DISSERTATION

FERROMAGNETIC RELAXATION IN (1) METALLIC THIN FILMS AND (2) BULK FERRITES AND COMPOSITE MATERIALS FOR INFORMATION STORAGE DEVICE AND MICROWAVE APPLICATIONS

Submitted by

Sangita S. Kalarickal

Department of Physics

In partial fulfillment of the requirements

For the Degree of Doctor of Philosophy

Colorado State University

Fort Collins, Colorado

Summer 2006

COLORADO STATE UNIVERSITY

July 11, 2006

WE HEREBY RECOMMEND THAT THE DISSERTATION PREPARED UNDER OUR SUPERVISION BY SANGITA S. KALARICKAL ENTITLED 'FERROMAGNETIC RELAXATION IN (1) METALLIC THIN FILMS AND (2) BULK FERRITES AND COMPOSITE MATERIALS FOR INFORMATION STORAGE DEVICE AND MICROWAVE APPLICATIONS' BE ACCEPTED AS FULFILLING IN PART REQUIREMENTS FOR THE DEGREE OF DOCTOR OF PHILOSOPHY.

Committee on Graduate Work

Professor R. M. Bradley

Professor R. G. Leisure

Professor C. S. Menoni

Professor R. E. Camley

Adviser Professor C. E. Patton

Department Head ~~Professor D. H. Hochheimer~~

ABSTRACT OF DISSERTATION

FERROMAGNETIC RELAXATION IN (1) METALLIC THIN FILMS AND (2) BULK FERRITES AND COMPOSITE MATERIALS FOR INFORMATION STORAGE DEVICE AND MICROWAVE APPLICATIONS

For a better understanding of fundamental magnetic loss processes in materials needed for microwave and information storage device applications, the ferromagnetic resonance (FMR) linewidth has been studied in (1) ferromagnetic metal films, (2) bulk ferrites, and (3) ferrite-ferroelectric composites. These materials have wide applications for high density magnetic storage as well as microwave isolators and circulators. The field of microwave magnetics, especially for magnetic metals, is ruled by a set of purely phenomenological models for the damping of the magnetodynamics. These operational models are supplemented by models for actual physical loss mechanisms. All of these models, phenomenological and physical, yield specific predictions of the linewidth vs. frequency response. Data on the frequency dependence of the ferromagnetic resonance linewidth can provide (1) insight into the relevant microwave loss processes and (2) a guide for the proper application of the different phenomenological models to materials design and device development. Comprehensive linewidth data also allow for (1) the identification of truly intrinsic losses and (2) the clarification of extrinsic losses due to inhomogeneities, imperfections, etc., that are candidates for elimination through the development of better materials.

The frequency dependence of the FMR linewidth in Permalloy films shows that the

dominant loss mechanism is akin to a Landau-Lifshitz or Gilbert type of phenomenological damping model. This trend matches the physical process of magnon-electron scattering. The frequency dependence of the Permalloy film FMR linewidth can be modeled by a combination of Landau-Lifshitz/Gilbert damping and broadening due to ripple fields and inhomogeneities. In Fe-Ti-N thin films, there are large extrinsic contributions that relate to two magnon scattering. This appears to be connected with changes in crystal structure due to the addition of nitrogen to the Fe-Ti matrix. The frequency dependence of the linewidth in hot isostatic pressed polycrystalline yttrium iron garnet explicitly demonstrates the anisotropy based two magnon scattering process for the randomly oriented grains. Microwave loss data for nickel zinc/barium strontium titanate composite materials show that composite or multifunctional materials can play a useful role in future systems that require electric field tuning and low power budgets.

Sangita Shreedharan Kalarickal
Department of Physics
Colorado State University
Fort Collins, CO 80523
Summer 2006

ACKNOWLEDGEMENTS

This work would not have been completed had it not been for the formidable support system I was fortunate enough to have.

I would like to acknowledge the Office of Naval Research, U.S. Army Office, and National Science Foundation for funding my research. Thanks are due, to Drs. Michael Schneider, Tom Silva and Pavel Kabos of National Institute of Standards and Technology, Boulder, for providing Permalloy thin films, and also help with the measurements on the pulsed inductive microwave magnetometer and the vector network analyzer FMR data analysis. Prof. C. Alexander is deeply acknowledged for providing the Fe-Ti-N samples, and many helpful discussions. Drs. Somnath and Louise Sengupta are acknowledged for providing ferrite-ferroelectric composite materials. The importance of the lessons I have learnt from these collaborations cannot be emphasized enough.

My advisor, Carl Patton taught me that anything is possible if one is willing to give it all that one has got and then some more. Thanks to you, Carl, I have acquired faith in the old school thought of physics, in basic integrity of research and in the fact that research is not much use, if it is not communicated well. Ah, I believe I have been 'Patton'ized.

Thanks are due to Dr. Michael Wittenauer for being a great mentor in the laboratory. Many happy hours were spent in the physics machine shop with Bob Adame who taught me a lot in terms of a positive outlook to life in general and machining in particular. My colleagues in the magnetics group are thanked for many helpful discussions, for help with

some of the data taking and proof reading this work, and in general, for being who they are! Thank you, Jaydip, Mingzhong, Kyoung Suk, Scott, Heidi, and especially Kevin! Mere thanks are not enough to Prof. Boris Kalinikos, Prof. Dieter Hochheimer, Prof. Siu Au Lee, and Prof. Sandy Kern for keeping my morale high throughout my time at the physics department. My friends, Bob and Nancy Sturtevant, Seema, Shekhar Cowsik, Vidya, Ana, Meghala, Zarine, Johan, Emma and Himali, many thanks for being there for me, through good times and bad! To my friends in India, I do not know how all of you learned this wonderful knack of providing long distance encouragement, but I am glad you did!

Pavol, my colleague, my friend, and one of my unfailing supports, words are a dilute form of expression. Thank you for walking with me.

My parents, thanks for your unconditional love, and confidence in me. My brother Darshan, you do not know that you have taught me to survive, and I hope for my own sanity that you never grow aware of the fact!

Nischal, without you I could *never* have gotten through this long road. With your love, I am never alone.

CONTENTS

ABSTRACT iii

ACKNOWLEDGEMENTS v

CHAPTER 1 INTRODUCTION

1.1 Microwave loss in ferromagnetic materials 1

1.2 Scope and outline of the dissertation 3

1.3 Units 6

CHAPTER 2 FERROMAGNETIC RESONANCE

2.1 Ferromagnetic Resonance: Introduction

2.1.1 Equation of motion of magnetization 9

2.1.2 Small signal limit and the linearized equation of motion 11

2.1.3 Uniform mode precession and the ferromagnetic resonance 13

2.1.4 Non-uniform modes: Spin waves 19

2.2 Phenomenological models for ferromagnetic relaxation

2.2.1 Landau-Lifshitz model 30

2.2.2 Gilbert model 32

2.2.3 Bloch Bloembergen model 32

2.2.4 Constrained Codrington Olds and Torey model 34

2.3 Frequency and field linewidth 36

2.4 Physical contributions to the FMR linewidth 40

2.4.1 Magnon electron scattering 42

2.4.2 Two magnon scattering 44

2.4.2A Two magnon scattering in a polycrystalline ferrite sample.... 47

2.4.2B Two magnon scattering in thin films 51

2.4.3 Inhomogeneous line broadening 55

2.4.4 Ripple field effect 56

2.5 Linewidth as a function of frequency:

A comparison of different models 57

2.6 Summary 61

2.7 References 63

CHAPTER 3 EXPERIMENTAL METHODS AND DATA ANALYSIS

3.1 Introduction 68

3.2 Field swept linewidth measurement techniques 70

3.2.1 Strip line ferromagnetic resonance spectrometer system 71

3.2.2 Shorted waveguide ferromagnetic resonance spectrometer system ... 75

3.3 Other ferromagnetic resonance linewidth measurement techniques

3.3.1 Vector network analyzer ferromagnetic resonance spectrometer system 78

3.3.2 Pulsed inductive microwave magnetometer system 83

3.4 Summary 87

3.5 References 88

CHAPTER 4 EXPERIMENTAL RESULTS I – FMR LINEWIDTH IN METAL FILMS

4.1: FMR in Permalloy films

4.1.1: Introduction and background 91

4.1.2: Material details 96

4.1.3: FMR linewidth for in plane magnetized films 96

4.1.4: Comparison of FMR linewidth obtained from different techniques 101

4.1.5: FMR linewidth for obliquely magnetized thin films 116

4.1.6: FMR linewidth for perpendicularly magnetized films 122

4.1.7: Summary and conclusions 126

4.2: FMR in nitrogenated Fe-Ti films

4.2.1: Introduction and background 128

4.2.2: Material details, resistivity and static magnetization results 131

4.2.4: Ferromagnetic resonance response 141

4.2.5: Summary and conclusions 151

4.3 References 153

CHAPTER 5 EXPERIMENTAL RESULTS II –

FMR LINEWIDTH IN BULK CERAMICS

5.1: Frequency dependence of linewidth in hot isostatic pressed yttrium iron garnet

5.1.1: Material details 160

5.1.2: Frequency dependence of FMR linewidth 161

5.1.3: Summary and conclusions 166

5.2: Microwave properties of ferrite ferroelectric composite materials 167

5.2.1: Materials details and crystallographic analysis 169

5.2.2: Static magnetization properties 172

5.2.3: Ferromagnetic resonance response 178

5.2.4: High field effective linewidth results 182

5.2.5: Summary and conclusions 188

5.3 References 189

CHAPTER 6 CONCLUSIONS

6.1 Summary of the work in the dissertation 193

6.2 Conclusions and future direction 196

Appendix 1: Table of materials used in this dissertation 199

Appendix2: Van der Pauw method for resistivity measurement 201

Appendix 3: High field effective linewidth measurement for composite materials with magnetic inclusions 204

REFERENCES 208

INTRODUCTION

Outline:

1.1: Microwave loss in ferromagnetic materials

1.2: Scope and outline of the dissertation

1.3: Units

1.1 MICROWAVE LOSS IN FERROMAGNETIC MATERIALS

The study of microwave excitation in magnetic materials is of primary importance in the design of various devices. Despite the nearly six decades of active research in this field of microwave magnetics, a complete understanding of the magnetic relaxation processes in these materials still evades magneticians. Meanwhile the role of these materials in everyday life has been increasing, with new materials posing new questions.

The most common method utilized to fingerprint the microwave loss in these materials is a study of the ferromagnetic resonance (FMR) spectrum of the sample. The ferromagnetic material in question is subject to a static external field and a

transverse microwave or millimeter wave field. This drives the precession of the magnetization about the equilibrium direction. The power absorbed by the sample is measured as a function of static external field or the frequency of the excitation field. The spectrum so obtained usually has a Lorentzian profile, with a maximum absorption of power at the FMR position. The full width at half maximum of the line, the FMR field swept linewidth ΔH or frequency swept linewidth $\Delta\omega$, is a measure of the microwave loss in the material and is also a rich source of information about the material itself.

The source of microwave loss in these materials is still a challenging question. There are two types of prevalent losses, namely intrinsic losses that are a signature of the material itself, and extrinsic losses that can mostly be eliminated by refining the manufacturing processes of the material. There have been several theories to model these losses. Intrinsic losses are modelled either by purely phenomenological models or by actual physical mechanisms, which describe the relaxation of the excited uniform mode magnon eventually to the lattice.

Evaluation of the FMR linewidth with reference to the types of damping mechanisms is a complex task. While the FMR linewidth at any particular field or frequency does give an indication of losses in the material, a complete spectrum is necessary before anything can be said about the intrinsic losses in the materials. Each model for magnetization relaxation, physical or phenomenological has a well-defined frequency dependence. Hence the frequency dependence of linewidth gives

an insight into the loss processes prevalent in the ferromagnetic and ferrimagnetic materials.

This thesis presents a study of FMR linewidth in different materials for device applications. These materials include metal films, which find use in high-density magnetic recording, and ferrites, which have wide applications in isolators, circulators etc. Frequency dependence of the FMR linewidth of the metal films and bulk ferrites helps unravel some of the sources of microwave damping in these materials. This thesis also presents results of an investigation of the static and dynamic magnetic properties of a series of ferrite-ferroelectric composite materials. These materials have become increasingly popular recently as they are being developed for their multifunctional properties which combine the frequency agility of ferrites with the low cost and size of ferroelectric materials.

1.2 SCOPE AND OUTLINE OF THE DISSERTATION

The work in this thesis consists of a study of the frequency dependence of the FMR linewidth in several materials for device applications and uses available theory to explain the several sources of losses. Chapter 2 is a review of the fundamental concepts of ferromagnetic resonance and relaxation. The Landau Lifshitz torque equation has been introduced and some phenomenological modifications of the torque equations are discussed to account for relaxation. Some physical processes like the magnon-electron scattering, the two magnon scattering mechanisms are

discussed. In addition to the relaxation mechanisms, some sources of FMR linebroadening have been discussed. The frequency dependence of FMR linewidth as given by these different models is examined.

Chapter 3 provides an extensive description of the experimental methodology used in this study. Three of the different microwave loss measurements methods that are in use today are discussed. The first method is the conventional field swept ferromagnetic resonance method, which uses either a strip transmission line or a shorted waveguide to provide the microwave excitation to the sample under consideration. The second is a frequency swept FMR measurement technique, which employs the use of modern vector network analyser to provide the excitation signal and analyse the transmission characteristics of the absorbed power from the sample. The third method is a pulsed inductive microwave magnetometer, which uses a pulsed DC signal for the excitation of the magnetization and extensive data analysis to provide the microwave loss parameters.

Chapter 4 presents the linewidth measurements results in two types of metallic films, which find use in the magnetic recording industry. One is Permalloy film, which is the material of choice for magnetic head pole. The FMR linewidth measurements on sputtered Permalloy films are compared for two different substrates. Results of the in plane, out of plane angle dependences and perpendicular to the plane measurements of FMR linewidth are presented. The second metallic film under study is the recently suggested for use in the next generation of magnetic recording heads, instead of Permalloy. These are nitrogenated iron-titanium films,

which are attractive for their soft magnetic properties and high saturation induction. Ferromagnetic resonance is studied in Fe-Ti-N for different nitrogen content, and in a wide frequency range. Frequency dependence of FMR linewidth in these Fe-Ti-N materials throws a new light on the dynamic properties, especially on the contribution of inhomogeneities and random anisotropy in the grains to the FMR linewidth.

Chapter 5 presents the results of linewidth measurements in two types of ceramic materials, which find use in several microwave devices. One such material, yttrium iron garnet (YIG) has been widely used and studied. Single crystal YIG is known to have the lowest microwave loss in any ferrite. Polycrystalline samples of bulk YIG have been studied extensively before, but the main source of microwave loss has been porosity. Typically, porosity contributes to an additional two-magnon linewidth of about 23 Oe/ percent porosity for YIG spheres. Recent processing advances in hot isostatic pressing (HIPPING) have however gone a long way in minimizing the porosity in these materials. With the porosity almost eliminated, it now becomes possible to measure frequency dependence of the two-magnon anisotropy scattering directly. Results of linewidth measurements in YIG and Ca-V substituted YIG are presented. The second material presented in this chapter, belongs to a newly emerging class of multifunctional materials. These are composite materials of ferrite and ferroelectric materials. Results on static and microwave magnetic measurements are presented.

Chapter 6 presents a summary and conclusions of the dissertation work and also ideas for future directions that can be taken.

1.3 UNITS

All physical parameters in this thesis are expressed in the Gaussian (cgs) system of units. The magnetic field **H** is expressed in Oersteds (Oe). The magnetization **M** is expressed in emu/cm^3. The corresponding magnetic induction **B** is expressed in Gauss (G). The saturation induction $4\pi M_s$ is expressed in Gauss, though the saturation magnetization M_s is in emu/cm^3.

FERROMAGNETIC RESONANCE AND RELAXATION

Outline:

2.1: Ferromagnetic Resonance: Introduction

2.1.1 Equation of motion of magnetization

2.1.2 Small signal limit and the linearized equation of motion

2.1.3 Uniform mode precession and ferromagnetic resonance

2.1.4 Non-uniform modes: Spin waves

2.2: Phenomenological models of ferromagnetic relaxation

2.2 .1 Landau-Lifshitz model

2.2 .2 Gilbert model

2.2 .3 Bloch Bloembergen model

2.2 .4 Constrained Codrington, Olds and Torrey model

2.3: Frequency and field linewidth

2.4: Physical contributions to the FMR linewidth

2.4.1 Magnon electron scattering

2.4.2 Two magnon scattering

2.4.2 A Two magnon scattering in a polycrystalline ferrite sample

2.4.2 B Two magnon scattering in thin films

2.4.3 Inhomogenous linebroadening

2.4.4 Ripple field effect

2.5: Linewidth as a function of frequency: a comparison of different models

2.6: Summary

2.7: References

2.1 FERROMAGNETIC RESONANCE: INTRODUCTION

Ferromagnetic resonance (FMR) has been under intense study since the first experiments made in 1946. (Griffiths 1946) This phenomenon provides a rich source of the information on magnetic material properties in the microwave regime. In particular, the magnetic relaxation parameters may be readily extracted from FMR linewidth data. The ubiquitous use of magnetic materials in high frequency applications has increased the importance of understanding spin dynamics and underlying magnetic relaxation. The sheer multiplicity of processes that come into play between the initial excitation of the magnetization in a microwave resonance experiment and the final state of thermal equilibrium with the lattice makes ferromagnetic relaxation a complicated process. Besides the physical processes that

may be responsible for this relaxation, several phenomenological models have also been advanced in its explanation.

This chapter lays down the basic working equations for ferromagnetic resonance and develops some concepts for FMR relaxation. This section provides an introduction to the ferromagnetic resonance condition. Section 2.2 outlines some of the popular phenomenological models for ferromagnetic relaxation. Section 2.3 gives a connection between the frequency and field swept linewidth. Section 2.4 outlines some of the well-known physical mechanisms for FMR relaxation and line broadening. Section 2.5 compares the frequency dependences of these different models and mechanisms.

2.1.1 EQUATION OF MOTION OF MAGNETIZATION

The properties of magnetically ordered materials, such as ferromagnets, are determined by the interactions of elementary magnetic moments. These moments are spin and orbital magnetic moments of the electrons and both are proportional to the corresponding angular momenta. In most cases it is the spin magnetic moment, which is dominant. This moment is equal to

$$\boldsymbol{\mu} = -|\gamma|\mathbf{S}, \tag{2.1}$$

where $\gamma = -g\mu_B / \hbar$ is the electron gyromagnetic ratio with a nominal value $\gamma = -1.76 \times 10^7$ s^{-1}/Oe in Gaussian units. Here, $g \approx 2$ is the electron Landé factor, μ_B is the Bohr magneton and $\mathbf{S}$ is the spin angular momentum of the electrons.

If a large enough magnetic field $\mathbf{H}$ is applied to the sample, the magnetic moments will be aligned in the direction of $\mathbf{H}$. Any perturbation from this equilibrium will result in a torque $\boldsymbol{\tau} = \boldsymbol{\mu} \times \mathbf{H}$ exerted by the field $\mathbf{H}$ on the magnetic moment $\boldsymbol{\mu}$. From classical mechanics, the torque is equal to rate of change of the angular momentum

$$\boldsymbol{\tau} = \frac{d\mathbf{S}}{dt} = \boldsymbol{\mu} \times \mathbf{H}. \tag{2.2}$$

From Eq. (2.1) and (2.2) we obtain an equation of motion for the magnetic moment

$$\frac{d\boldsymbol{\mu}}{dt} = -|\gamma| \boldsymbol{\mu} \times \mathbf{H}. \tag{2.3}$$

The strong magnetic ordering in ferromagnets is caused by exchange interaction, due to which, the neighboring spins tend to have magnetic moments oriented parallel to each other. In this case, the dynamic processes of large collection of spins, or magnetic moments, may be investigated in a continuum approximation. In this approximation the magnetization $\mathbf{M}(\mathbf{r},t)$, a macroscopic quantity, is used to describe the magnetic properties of the sample. This quantity is defined as

$$\mathbf{M}(\mathbf{r},t) = \frac{1}{\Delta V} \sum_{\Delta V} \boldsymbol{\mu} \quad = \frac{\boldsymbol{\mu}_{\Delta V}}{\Delta V}, \tag{2.4}$$

where $\boldsymbol{\mu}_{\Delta V}$ is the net magnetic moment of a small volume ΔV situated at a position $\mathbf{r}$.

The equation of motion of the magnetization $\mathbf{M}(\mathbf{r},t)$, as proposed by Landau and Lifshitz and known as the Landau-Lifshitz torque equation, then follows from Eq. (2.3) and is given by:

$$\frac{d\mathbf{M}(\mathbf{r},t)}{dt} = -|\gamma|\mathbf{M}(\mathbf{r},t)\times\mathbf{H}_{\text{eff}}(\mathbf{r},t). \tag{2.5}$$

In this dissertation, Eq. (2.5) will be referred to as the torque equation. Here $\mathbf{H}_{\text{eff}}(\mathbf{r},t)$ is the total effective magnetic field and in general includes externally applied fields and various internal fields due to dipolar, exchange, and anisotropy interactions. These internal fields are a function of the magnetization itself, which makes Eq. (2.5) nonlinear with respect to $\mathbf{M}(\mathbf{r},t)$. In this work, however, only small-signal limit is considered and Eq. (2.5) will be used in the linearized form.

Note that the Eq. (2.5) does not allow for losses. Phenomenological models of dissipation will be discussed in Section 2.2. Physical origins of dissipation mechanisms will be then considered in Section 2.3.

2.1.2 SMALL-SIGNAL LIMIT AND THE LINEARIZED EQUATION OF MOTION

The solution to the torque equation (2.5) becomes more tractable if both the magnetization $\mathbf{M}(\mathbf{r},t)$ and the total magnetic field $\mathbf{H}_{\text{eff}}(\mathbf{r},t)$ are first separated into

static and dynamic components. Typically, the dynamic components are much smaller than the static components. In addition, the static magnetization and the field components can be considered to be uniform throughout the sample volume. One can therefore write

$$\begin{aligned} &\mathbf{M}(\mathbf{r},t) = \mathbf{M}_0 + \mathbf{m}(\mathbf{r},t), && |\mathbf{m}(\mathbf{r},t)| \ll |\mathbf{M}_0|, \\ &\mathbf{H}_{\text{eff}}(\mathbf{r},t) = \mathbf{H}_0 + \mathbf{h}(\mathbf{r},t), && |\mathbf{h}(\mathbf{r},t)| \ll |\mathbf{H}_0|. \end{aligned} \tag{2.6}$$

Here $\mathbf{M}_0$ and $\mathbf{H}_0$ represent the static uniform components, and $\mathbf{m}(\mathbf{r},t)$ and $\mathbf{h}(\mathbf{r},t)$ are the small dynamic non-uniform components of magnetization and total magnetic field respectively. Right-hand side of Eq. (2.5) then can be written as a sum of four cross products. The cross product of small quantities $\mathbf{m}(\mathbf{r},t)\times\mathbf{h}(\mathbf{r},t)$ will be neglected in the small-signal limit approximation.

The cross product of the static components $\mathbf{M}_0\times\mathbf{H}_0$ must vanish at the static equilibrium. The solution to the static equilibrium problem will be discussed later for particular geometries. In fact, this solution defines the preferred coordinate system. For the present moment we assume that the coordinate system is chosen in such a way that the magnetization static equilibrium position is oriented along the $z-$axis. In the small signal limit the magnetization deviation from the $z-$axis can be considered as small quantity. To the first order one can therefore write $\mathbf{M}_0 = M_s\mathbf{z}$, where M_s is magnetization at saturation. The M_s value corresponds to the length of the magnetization vector and it will be considered as a conserved quantity. Both the transverse $x, y-$components of $\mathbf{H}_0$ must be zero because of the

static equilibrium condition $M_s \mathbf{z} \times \mathbf{H}_0 = 0$. One can therefore write $\mathbf{H}_0 = H_i \mathbf{z}$, where H_i is total static internal field.

Equation (2.5) in the small signal limit will then attain the form

$$\frac{d\mathbf{m}(\mathbf{r},t)}{dt} = -|\gamma| \mathbf{z} \times \left[M_s \, \mathbf{h}(\mathbf{r},t) - H_i \, \mathbf{m}(\mathbf{r},t) \right], \tag{2.7}$$

or in the transverse x, y – components

$$\begin{aligned} \frac{dm_x(\mathbf{r},t)}{dt} &= -|\gamma| \left[H_i \, m_y(\mathbf{r},t) - M_s \, h_y(\mathbf{r},t) \right], \\ \frac{dm_y(\mathbf{r},t)}{dt} &= \quad |\gamma| \left[H_i \, m_x(\mathbf{r},t) - M_s \, h_x(\mathbf{r},t) \right]. \end{aligned} \tag{2.8}$$

The set of equations (2.8), accompanied by the appropriate boundary conditions constitutes a mathematical model of magnetization dynamics in small-signal limit. In particular, the solutions to this equation provide the ferromagnetic resonance condition and the spin-wave dispersion.

2.1.3 UNIFORM MODE PRECESSION AND FERROMAGNETIC RESONANCE

Consider the case of an ellipsoidal sample. The sample geometries used in this work, spheres and thin films, can be treated as limiting cases of the ellipsoid. Figure 2.1 shows the sample and the field geometry. Here, capital X, Y, Z alphabets depict the coordinate system in which the axes coincide with the axes of the ellipsoid. This

coordinate system will be referred to as the sample frame. Lowercase x, y, z alphabets refer to the coordinate system in which the magnetization static equilibrium position coincides with the $z-$axis. This coordinate system will be also referred to as the precessional frame.

Suppose now that sample is uniformly magnetized and both magnetization $\mathbf{M}(t)$ and the magnetic field $\mathbf{H}_{\text{eff}}(t)$ are therefore a function of time alone. In the small-signal limit, the magnetization in the x, y, z system may be written as

$$\mathbf{M}(t) = \begin{pmatrix} m_{0x}(t) \\ m_{0y}(t) \\ M_s \end{pmatrix}. \tag{2.9}$$

Here, the '0' index emphasizes that the dynamic magnetization is uniform throughout the sample volume.

The total magnetic field $\mathbf{H}_{\text{eff}}(t)$ is comprised of the external static field $\mathbf{H}$, the external microwave pump field $\mathbf{h}_{\text{p}}(t)$, and the demagnetizing field $\mathbf{H}_{\text{D}}(t)$ due to the sample boundaries.

$$\begin{aligned} \mathbf{H}_{\text{eff}}(t) &= \mathbf{H} + \mathbf{h}_{\text{p}}(t) + \mathbf{H}_{\text{D}}(t) \\ &= \mathbf{H} + \mathbf{h}_{\text{p}}(t) - 4\pi\tilde{\text{N}} \cdot \mathbf{M}(t). \end{aligned} \tag{2.10}$$

Here, $\tilde{\text{N}}$ is the demagnetization tensor. This tensor is diagonal in the X, Y, Z coordinate system and the diagonal components N_X, N_Y, N_Z for general ellipsoid

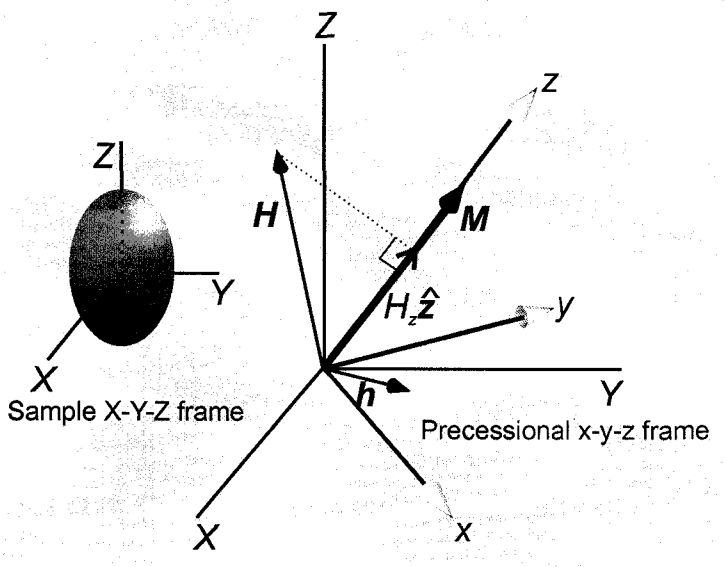

FIG. 2.1. Sample and fields geometry.

can be evaluated analytically (Osborn, 1945). In the x, y, z coordinate system, however, this demagnetizing tensor is generally non-diagonal, but still symmetric.

$$\ddot{N} = \begin{pmatrix} N_{xx} & N_{xy} & N_{xz} \\ N_{xy} & N_{yy} & N_{yz} \\ N_{xz} & N_{yz} & N_{zz} \end{pmatrix}, \tag{2.11}$$

From Eq. (2.10) the total magnetic field $\mathbf{H}_{\text{eff}}(t)$ written separately in the x, y, z components is therefore

$$\begin{pmatrix} H_{\text{eff}\,x}(t) \\ H_{\text{eff}\,y}(t) \\ H_{\text{eff}\,z}(t) \end{pmatrix} = \begin{pmatrix} H_x - 4\pi N_{xz} M_s \\ H_y - 4\pi N_{yz} M_s \\ H_z - 4\pi N_{zz} M_s \end{pmatrix} + \begin{pmatrix} h_{\text{p}x}(t) \\ h_{\text{p}y}(t) \\ h_{\text{p}z}(t) \end{pmatrix} - 4\pi \begin{pmatrix} N_{xx} m_{0x}(t) + N_{xy} m_{0y}(t) \\ N_{xy} m_{0x}(t) + N_{yy} m_{0y}(t) \\ N_{xz} m_{0x}(t) + N_{yz} m_{0y}(t) \end{pmatrix}. \tag{2.12}$$

Since both static transverse (x, y) components must be zero, the equations

$$\begin{aligned} &H_x - 4\pi N_{xz} M_s = 0 \\ &\text{and} \\ &H_y - 4\pi N_{yz} M_s = 0 \end{aligned} \tag{2.13}$$

constitute the static equilibrium condition. The total static internal field in the $z-$direction is $H_i = H_z - 4\pi N_{zz} M_s$. The uniform dynamic transverse $x, y-$fields are

$$\begin{pmatrix} h_{0x}(t) \\ h_{0y}(t) \end{pmatrix} = \begin{pmatrix} h_{px}(t) \\ h_{py}(t) \end{pmatrix} - 4\pi \begin{pmatrix} N_{xx} & N_{xy} \\ N_{xy} & N_{yy} \end{pmatrix} \cdot \begin{pmatrix} m_{0x}(t) \\ m_{0y}(t) \end{pmatrix}. \tag{2.14}$$

The linearized torque equation (2.8) can be then written conveniently in the matrix form

$$\frac{d}{dt}\begin{pmatrix} m_{0x}(t) \\ m_{0y}(t) \end{pmatrix} = |\gamma| \begin{pmatrix} -\mathrm{H}_{xy} & -\mathrm{H}_{yy} \\ \mathrm{H}_{xx} & \mathrm{H}_{xy} \end{pmatrix} \cdot \begin{pmatrix} m_{0x}(t) \\ m_{0y}(t) \end{pmatrix} + |\gamma| M_s \begin{pmatrix} h_{py}(t) \\ -h_{px}(t) \end{pmatrix}. \tag{2.15}$$

Here, so-called uniform stiffness fields have been introduced as

$$\begin{aligned} &\mathrm{H}_{xx} = H_i + 4\pi N_{xx} M_s = H_z + 4\pi \left(N_{xx} - N_{zz}\right) M_s, \\ &\mathrm{H}_{yy} = H_i + 4\pi N_{yy} M_s = H_z + 4\pi \left(N_{yy} - N_{zz}\right) M_s, \\ &\text{and} \\ &\mathrm{H}_{xy} = 4\pi N_{xy} M_s. \end{aligned} \tag{2.16}$$

Stiffness fields account for the fact that when the magnetization is tipped out of the equilibrium, both the instantaneous torque exerted on the magnetization and the corresponding instantaneous frequency is changed. Equivalently one may introduce the uniform stiffness frequencies as,

$$\omega_{xx}=|\gamma|\mathrm{H}_{xx},\quad \omega_{yy}=|\gamma|\mathrm{H}_{yy},\ \text{and}\ \omega_{xy}=|\gamma|\mathrm{H}_{xy}. \tag{2.17}$$

Equation (2.15) describes a simple undamped harmonic oscillator driven by the excitation field components $h_{px,y}(t)$. Consider first the free motion without the excitation, i.e. with $h_{px,y}(t)=0$. The eigenfrequencies of the oscillator can be found easily

$$\omega_0=\pm|\gamma|\sqrt{\mathrm{H}_{xx}\mathrm{H}_{yy}-\mathrm{H}_{xy}^2}=\pm\sqrt{\omega_{xx}\omega_{yy}-\omega_{xy}^2}\,. \tag{2.18}$$

The free motion of the transverse magnetization components in the linear regime is represented therefore as a simple harmonic oscillation with the frequency ω_0

$$m_{0x,y}(t)\propto \mathrm{Re}\left\{\mathrm{e}^{i\omega_0 t}\right\}. \tag{2.19}$$

The magnetization motion in the presence of the pump can be found easily too. For the particularly interesting case of the harmonic pump with an arbitrary polarization

$$\begin{aligned} h_{\mathrm{px}}(t)&=|h_{\mathrm{px}}|\cos(\omega t),\\ h_{\mathrm{py}}(t)&=|h_{\mathrm{py}}|\cos(\omega t-\varphi), \end{aligned} \tag{2.20}$$

the solution is given by

$$\begin{aligned} m_{0x,y}(t)&=\mathrm{Re}\left\{m_{0x,y}(\omega)\,\mathrm{e}^{i\omega t}\right\},\\ \begin{pmatrix} m_{0x}(\omega)\\ m_{0y}(\omega)\end{pmatrix}&=\ddot{\chi}_{\mathrm{e}}(\omega)\cdot\begin{pmatrix} |h_{\mathrm{px}}|\\ |h_{\mathrm{py}}|\,\mathrm{e}^{-i\varphi}\end{pmatrix}, \end{aligned} \tag{2.21}$$

where $\ddot{\chi}_{\mathrm{e}}(\omega)$ is the external susceptibility tensor

Geometry	N_X	N_Y	N_Z	Ferromagnetic resonance condition
 sphere	1/3	1/3	1/3	$\omega_0 = \lvert\gamma\rvert H$
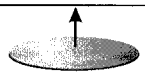 perpendicularly magnetized film	0	0	1	$\omega_0 = \lvert\gamma\rvert\left[H - 4\pi M_s\right]$
 in plane magnetized film	1	0	0	$\omega_0 = \lvert\gamma\rvert\sqrt{H\left(H + 4\pi M\right.}$

TABLE 2.1 Demagnetizing factors and ferromagnetic resonance conditions for selected geometries.

$$\ddot{\chi}_e(\omega) = \begin{pmatrix} \chi_{xx} & \chi_{xy} \\ \chi_{yx} & \chi_{yy} \end{pmatrix} = \frac{|\gamma| M_s}{\omega_0^2 - \omega^2} \begin{pmatrix} \omega_{yy} & i\omega - \omega_{xy} \\ -i\omega - \omega_{xy} & \omega_{xx} \end{pmatrix}. \tag{2.22}$$

The term "external" emphasizes the fact that the susceptibility tensor $\ddot{\chi}_e(\omega)$ relates the dynamic magnetization components and externally applied microwave field. One can see that the $\ddot{\chi}_e(\omega)$ tensor is non-symmetric and shows a resonant dependence on the frequency ω. The non-symmetric property is often termed gyrotropy. The corresponding FMR frequency is equal to ω_0, given by Eq. (2.18).

Consider now the particular case when the external static field with a magnitude H is oriented along one of the ellipsoid axes. In such a case the static equilibrium direction is oriented along this axis too, and both X, Y, Z and x, y, z frames coincide. In addition $H_z = H$, and the demagnetizing tensor becomes diagonal. The FMR frequency (2.18) may be therefore written as

$$\omega_0 = |\gamma| \sqrt{\left[H + 4\pi\left(N_X - N_Z\right)M_s\right]\left[H + 4\pi\left(N_Y - N_Z\right)M_s\right]}. \quad (2.23)$$

This result is known as the Kittel resonance condition. The demagnetization factors $N_{X,Y,Z}$ and the resonance conditions for selected geometries are given in Table 2.1.

Figure 2.2 shows sketches of the FMR frequency ω_0 vs. external static H field for the geometries listed in Table 2.1. The labels on the horizontal axis in graph (a) and (c) denote the values of the saturation field for the respective geometries. Below this field, the sample is not saturated. One can see that for a sample with rotational symmetry about the static equilibrium direction, as for the sphere and for the perpendicularly magnetized film, the resonance frequency ω_0 depends linearly on H. However for the sample with a broken symmetry, for example, in the case of an in plane magnetized film, this dependence is non-linear. This behavior is related to the ellipticity of the magnetization precession.

2.1.4 NON-UNIFORM MODES – SPIN WAVES

The spin wave concept was first introduced by Bloch in 1930. (Bloch 1930), (Lax and Button 1962) Subsequently, Herring and Kittel treated spin wave excitations in a semi classical manner with the inclusion of the exchange field in the torque equation. (Herring and Kittel 1951)

We start with the assumption that the spatial dependence of both $\mathbf{m}(\mathbf{r},t)$ and $\mathbf{h}(\mathbf{r},t)$ in Eq. (2.7) can be expanded in a Fourier series

$$\mathbf{m}(\mathbf{r},t)=\sum_{\mathbf{k}}\mathbf{m}_{\mathbf{k}}(t)e^{i\mathbf{k}\cdot\mathbf{r}},$$
$$\mathbf{h}(\mathbf{r},t)=\sum_{\mathbf{k}}\mathbf{h}_{\mathbf{k}}(t)e^{i\mathbf{k}\cdot\mathbf{r}}. \tag{2.24}$$

The particular case of the uniform mode precession ($\mathbf{k}=0$) has been already discussed in Section 2.1.3. In the following analysis only $\mathbf{k}\neq 0$ will be considered. The linearity of the Fourier transform guaranties that the Fourier components of both transverse magnetization and field again satisfy a set of equations analogous to Eq. (2.8)

$$\frac{dm_{\mathbf{k}x}(t)}{dt}=-|\gamma|\left[H_i\, m_{\mathbf{k}y}(t)-M_s\, h_{\mathbf{k}y}(t)\right],$$
$$\frac{dm_{\mathbf{k}y}(\mathbf{r},t)}{dt}=\quad|\gamma|\left[H_i\, m_{\mathbf{k}x}(t)-M_s\, h_{\mathbf{k}x}(t)\right]. \tag{2.25}$$

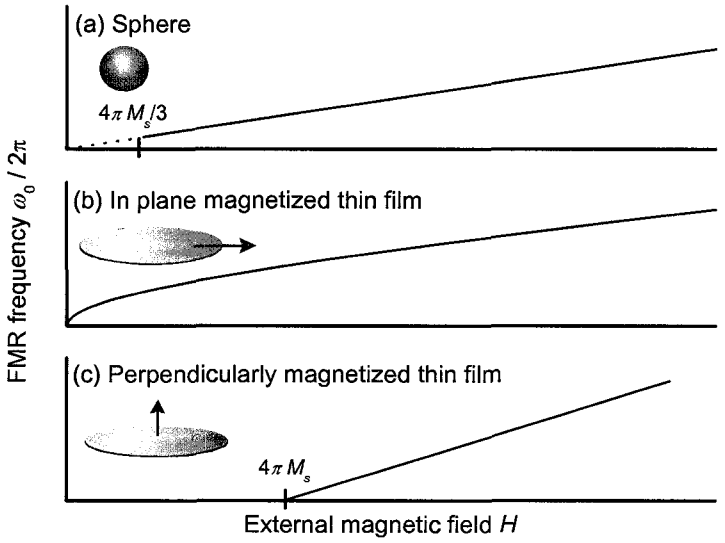

FIG. 2.2. Schematic representation of FMR frequency vs. external magnetic field for different sample geometries as indicated.

We now need to express the Fourier components of the dynamic field $h_{\mathbf{k}x,y}(t)$ in terms of the Fourier components of the dynamic magnetization $m_{\mathbf{k}x,y}(t)$. As long as the relation between these quantities can be written in the matrix form equivalent to Eq. (2.14), further analysis will follow the same path as given in Section 2.1.3 for the uniform mode.

Assume for simplicity that the microwave pump field is uniform throughout the sample and therefore it will not contribute to $\mathbf{k} \neq 0$ mode dynamics. The task is to find a $\mathbf{k}-$dependent tensor $\ddot{N}_{\mathbf{k}}$ that satisfies

$$\mathbf{h}_{\mathbf{k}}(t) = -4\pi \ddot{N}_{\mathbf{k}} \cdot \mathbf{m}_{\mathbf{k}}(t). \tag{2.26}$$

In the linear case, only the 2×2 submatrix of this tensor for the transverse $x, y-$components of $\mathbf{m}_{\mathbf{k}}(t)$ and $\mathbf{h}_{\mathbf{k}}(t)$ is important

$$\begin{pmatrix} h_{\mathbf{k}x}(t) \\ h_{\mathbf{k}y}(t) \end{pmatrix} = -4\pi \begin{pmatrix} N_{\mathbf{k}xx} & N_{\mathbf{k}xy} \\ N_{\mathbf{k}xy} & N_{\mathbf{k}yy} \end{pmatrix} \cdot \begin{pmatrix} m_{\mathbf{k}x}(t) \\ m_{\mathbf{k}y}(t) \end{pmatrix}. \tag{2.27}$$

In order to find $\ddot{N}_{\mathbf{k}}$ one has to first find the relation between $\mathbf{h}(\mathbf{r},t)$ and $\mathbf{m}(\mathbf{r},t)$ in $\mathbf{r}-$space and then to transform this relation into $\mathbf{k}-$space. For the present case of an isotropic sample, there are two dynamic, non-uniform fields that need to be taken into account: the exchange field $\mathbf{h}_{\mathrm{ex}}(\mathbf{r},t)$ and the dipolar field $\mathbf{h}_{\mathrm{dip}}(\mathbf{r},t)$.

The exchange field

The exchange field $\mathbf{h}_{ex}(\mathbf{r},t)$ is an effective field that tends to align adjacent magnetic moments due to exchange interaction. This field can be expressed as

$$\mathbf{h}_{ex}(\mathbf{r},t)=\frac{D}{M_s}\nabla^2\mathbf{m}(\mathbf{r},t), \tag{2.28}$$

where D is the exchange constant with the units of Oe·cm^2/rad^2. Fourier transform of Eq. (2.28) directly yields

$$\begin{aligned}\mathbf{h}_{\mathbf{k},ex} &= -\frac{D}{M_s}k^2\,\mathbf{m}_{\mathbf{k}}(t)=-4\pi\ddot{N}_{\mathbf{k},ex}\cdot\mathbf{m}_{\mathbf{k}}(t),\\ \ddot{N}_{\mathbf{k},ex} &= \frac{Dk^2}{4\pi M_s}\begin{pmatrix}1&0&0\\0&1&0\\0&0&1\end{pmatrix},\end{aligned} \tag{2.29}$$

where $k=|\mathbf{k}|$.

The dipolar field

The dipolar field $\mathbf{h}_{dip}(\mathbf{r},t)$ is the field due to volume and surface magnetic charges. This field can be calculated from the Maxwell's equations. These equations in so-called magnetostatic approximation have the form

$$\begin{aligned}&\nabla\times\mathbf{h}_{dip}(\mathbf{r},t)=0,\\ &\nabla\cdot\mathbf{h}_{dip}(\mathbf{r},t)=-4\pi\nabla\cdot\mathbf{m}(\mathbf{r},t)\end{aligned} \tag{2.30}$$

The magnetostatic approximation is applicable as long as the wave numbers k of spin waves of interest are much larger than the wave number of the electromagnetic wave $k_0 = \omega / c$. For the frequencies in the GHz range, the condition $k \gg k_0$ is satisfied for wave numbers k of the order of 10 rad/cm.

The solution to Eq. (2.30) is determined by the boundary conditions and therefore it depends on the sample geometry. Here, two particular cases will be discussed (i) a bulk, effectively infinite, sample, and (ii) a thin film with uniform magnetization across the film thickness. The first solution will be used for the spherical ferrite samples, while the second one for a metallic thin film samples.

The dipolar field solution for the bulk case can be obtained readily from Eqs. (2.24) and (2.30). The Fourier components of the dipolar field in this case obey

$$\mathbf{h}_{\mathbf{k},\mathrm{dip}}(t) = -4\pi \frac{\mathbf{k}\left[\mathbf{k}\cdot\mathbf{m}_{\mathbf{k}}(t)\right]}{k^2}. \tag{2.31}$$

Assume that the direction of the wave vector $\mathbf{k}$ in the precessional frame is determined by azimuthal and polar angles φ_k and θ_k respectively, as shown in Fig. 2.3(a). Then the Eq. (2.31) can be written in the tensor form

$$\mathbf{h}_{\mathbf{k},\mathrm{dip}} = -4\pi \vec{\vec{N}}^{\mathrm{bulk}}_{\mathbf{k},\mathrm{dip}} \cdot \mathbf{m}_{\mathbf{k}}(t),$$

$$\text{as } \vec{\vec{N}}^{\mathrm{bulk}}_{\mathbf{k},\mathrm{dip}} = \begin{pmatrix} n_{xx} & n_{xy} & n_{xz} \\ n_{xy} & n_{yy} & n_{yz} \\ n_{xz} & n_{yz} & n_{zz} \end{pmatrix}, \tag{2.32}$$

where

$$n_{xx} = \sin^2\theta_k \cos^2\varphi_k,$$
$$n_{yy} = \sin^2\theta_k \sin^2\varphi_k,$$
$$n_{zz} = \cos^2\theta_k,$$
$$n_{xy} = \sin^2\theta_k \sin\varphi_k \cos\varphi_k,$$
$$n_{xz} = \sin\theta_k \cos\theta_k \cos\varphi_k,$$
$$n_{yz} = \sin\theta_k \cos\theta_k \sin\varphi_k.$$

The dipolar field solution for a thin film was found by Kalinikos and Slavin with use of the Green's function approach. (Kalinikos and Slavin 1986) The general solution for the film with an arbitrary thickness cannot be written simply in the form of the plane wave expansion (2.24). For a very thin film, however, one can use an approximation proposed by Harte. (Harte 1965) In this approximation it is assumed that the magnitude of the magnetization is constant across the film thickness. The Fourier expansion (2.24) then comprises of two-dimensional wave vectors **k** confined in the film plane.

The coordinate system for the wave vector **k** must by now be altered to account

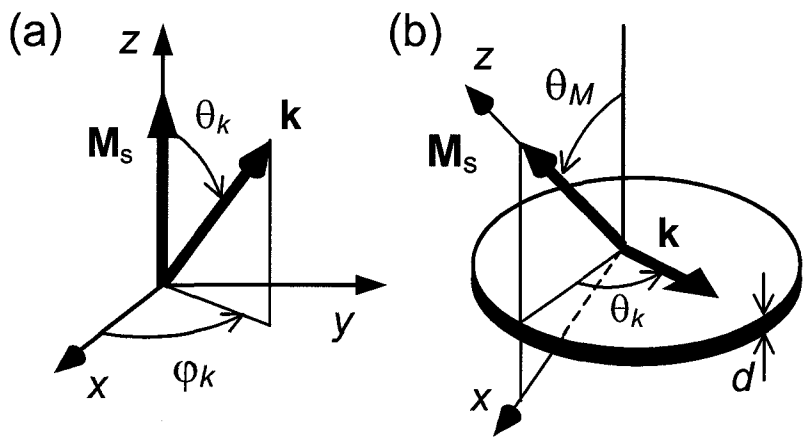

FIG. 2.3. The coordinate systems for the wavevector **k** in case of (a) bulk sample, (b) thin film sample.

for a general orientation of the static equilibrium with respect to the film plane. This coordinate system is shown in the Fig. 2.3(b). Here, the propagation direction of the wave vector $\mathbf{k}$ is determined by the angle θ_k with respect to the projection of the static equilibrium position on the film plane. This projection also lies in the $x-z$ plane. Angle θ_M defines the orientation of the magnetization static equilibrium with respect to the film normal. For this geometry, the Fourier components of the dipolar field are given by

$$\mathbf{h}_{\mathbf{k},\mathrm{dip}} = -4\pi \ddot{N}^{\mathrm{film}}_{\mathbf{k},\mathrm{dip}} \cdot \mathbf{m}_{\mathbf{k}}(t),$$
$$\ddot{N}^{\mathrm{film}}_{\mathbf{k},\mathrm{dip}} = \begin{pmatrix} n_{xx} & n_{xy} & n_{xz} \\ n_{xy} & n_{yy} & n_{yz} \\ n_{xz} & n_{yz} & n_{zz} \end{pmatrix}, \tag{2.33}$$

where

$$n_{xx} = (1-N_k)\cos^2\theta_k \cos^2\theta_M + N_k \sin^2\theta_M,$$
$$n_{yy} = (1-N_k)\sin^2\theta_k,$$
$$n_{zz} = (1-N_k)\cos^2\theta_k \sin^2\theta_M + N_k \cos^2\theta_M,$$
$$n_{xy} = (1-N_k)\sin\theta_k \cos\theta_k \cos\theta_M,$$
$$n_{xz} = \left[(1-N_k)\cos^2\theta_k - N_k\right]\sin\theta_M \cos\theta_M,$$
$$n_{yz} = (1-N_k)\sin\theta_k \cos\theta_k \sin\theta_M,$$

and

$$N_k = (1-\mathrm{e}^{-kd})/kd \tag{2.34}$$

is the Harte dipolar factor (Harte 1965), and d is the film thickness.

The total tensor $\ddot{N}_{\mathbf{k}}$ in Eq. (2.26) can be written as a sum of the exchange tensor given by Eq. (2.29) and either bulk or thin film dipolar tensor given by Eq. (2.32) or (2.33) respectively. Recall that only $N_{\mathbf{k}xx}$, $N_{\mathbf{k}yy}$ and $N_{\mathbf{k}xy}$ components of the resulting tensor are important for the linear case. The equation of motion (2.25) for transverse Fourier components of the magnetization can be written in the form analogous to the Eq. (2.15) for the uniform mode

$$\frac{d}{dt}\begin{pmatrix} m_{\mathbf{k}x}(t) \\ m_{\mathbf{k}y}(t) \end{pmatrix} = |\gamma| \begin{pmatrix} -\mathrm{H}_{\mathbf{k}xy} & -\mathrm{H}_{\mathbf{k}yy} \\ \mathrm{H}_{\mathbf{k}xx} & \mathrm{H}_{\mathbf{k}xy} \end{pmatrix} \cdot \begin{pmatrix} m_{\mathbf{k}x}(t) \\ m_{\mathbf{k}y}(t) \end{pmatrix}. \tag{2.35}$$

Here, the non-uniform stiffness fields have been introduced as

$$\begin{aligned} \mathrm{H}_{\mathbf{k}xx} &= H_i + 4\pi N_{\mathbf{k}xx} M_s, \\ \mathrm{H}_{\mathbf{k}yy} &= H_i + 4\pi N_{\mathbf{k}yy} M_s, \\ \mathrm{H}_{\mathbf{k}xy} &= 4\pi N_{\mathbf{k}xy} M_s. \end{aligned} \tag{2.36}$$

The eigenfrequency $\omega_{\mathbf{k}}$ for the $\mathbf{k}-$th mode is, similar to Eq. (2.18),

$$\omega_{\mathbf{k}} = |\gamma| \sqrt{\mathrm{H}_{\mathbf{k}xx}\mathrm{H}_{\mathbf{k}yy} - H_{\mathbf{k}xy}^2}. \tag{2.37}$$

Only the eigenfrequency with the positive sign has been considered here. The dependence of $\omega_{\mathbf{k}}$ on the wave vector $\mathbf{k}$ is called the spin-wave dispersion and it characterizes the linear properties of the spin wave propagation.

For bulk samples, the non-uniform stiffness fields are given by

$$\begin{aligned} \mathrm{H}_{\mathbf{k}xx} &= H_i + Dk^2 + 4\pi M_s \sin^2\theta_k \cos^2\varphi_k, \\ \mathrm{H}_{\mathbf{k}yy} &= H_i + Dk^2 + 4\pi M_s \sin^2\theta_k \sin^2\varphi_k, \\ \mathrm{H}_{\mathbf{k}xy} &= 4\pi M_s \sin^2\theta_k \sin\varphi_k \cos\varphi_k . \end{aligned} \tag{2.38}$$

In this case one gets the well-known result for bulk spin wave dispersion

$$\omega_{\mathbf{k}} = |\gamma| \sqrt{\left(H_i + Dk^2\right)\left(H_i + Dk^2 + 4\pi M_s \sin^2\theta_k\right)}. \tag{2.39}$$

Due to rotational symmetry of the isotropic sample considered here, the dispersion does not depend on the azimuthal angle φ_k. A sketch of the spin wave dispersion for a bulk sample is shown in Fig. 2.4(a). The overall frequency curvature is proportional to k^2 and is determined by the exchange term. The spread in the spin wave frequency for different propagation angles θ_k is related to dipolar interactions.

For thin film samples, the non-uniform stiffness fields are given by

$$\begin{aligned} \mathrm{H}_{\mathbf{k}xx} &= H_i + Dk^2 \\ &\quad + 4\pi M_s \left[(1-N_k)\cos^2\theta_k \cos^2\theta_M + N_k \sin^2\theta_M\right], \\ \mathrm{H}_{\mathbf{k}yy} &= H_i + Dk^2 + 4\pi M_s (1-N_k)\sin^2\theta_k, \\ \mathrm{H}_{\mathbf{k}xy} &= 4\pi M_s (1-N_k)\sin\theta_k \cos\theta_k \cos\theta_M . \end{aligned} \tag{2.40}$$

The spin wave dispersion for an obliquely magnetized thin film is a relatively complex function. The result, however, is appreciably simplified for the special cases of in-plane ($\theta_M = \pi/2$) magnetized thin film

$$\omega_{\mathbf{k}} = |\gamma| \sqrt{\begin{array}{l} \left(H_i + Dk^2 + 4\pi M_s N_k\right) \\ \times\left(H_i + Dk^2 + 4\pi M_s (1-N_k)\sin^2\theta_k\right) \end{array}}, \tag{2.41}$$

and perpendicularly ($\theta_M = 0$) magnetized thin film

$$\omega_{\mathbf{k}} = |\gamma| \sqrt{\left(H_i + Dk^2\right)\left(H_i + Dk^2 + 4\pi M_s (1 - N_k)\right)} \,. \tag{2.42}$$

Note that for the isotropic thin film, $H_i = H$ for the in-plane configuration, and $H_i = H - 4\pi M_s$ for the perpendicular configuration. Here, H is the external static field. In the limit of $k \to 0$ ($N_k \to 1$) the spin-wave frequency for a thin film therefore correctly reduces to the uniform mode frequency ω_0 shown in Table 2.1.

Figure 2.4b shows sketch of the spin wave dispersion (2.41) for an in-plane magnetized thin film. The dispersion is appreciably modified compared to the bulk sample case shown in Fig. 2.4(a). The dispersion exhibits a decrease of the spin wave frequency with an increase of the wave number for a certain range of the wave numbers k and propagation angles θ_k. This behavior is related to dipolar interactions and the corresponding spin waves are often referred to as magnetostatic backward waves since their phase and group velocities have opposite signs. In contrast, as follows from Eq. (2.42), there is no angular dependence of the dispersion for a perpendicularly magnetized thin film due to the rotational symmetry of the perpendicular configuration.

2.2 PHENOMENOLOGICAL MODELS OF FERROMAGNETIC RELAXATION

Phenomenology is a 20th-century philosophical movement founded by the German philosopher Edmund Husserl and is dedicated to *the description of experiences as they present themselves, without recourse to theory, deduction, or assumptions from other disciplines such as the natural sciences* (Husserl). Though this definition of phenomenology is too rigid for the spirit in which the phenomenological theories for the ferromagnetic relaxation of magnetization have been formulated, the basic idea remains the same. The importance of these theories lies in the fact that even though they are phenomenological, the field of microwave magnetics, especially for magnetic metals, is dominated by these models for the damping of the magnetodynamics. These theories have been widely used in the design of devices and the more popular ones have been summarized below. These theories take microwave losses into account with the addition of a loss term into the torque equation

$$\frac{d\mathbf{M}(\mathbf{r},t)}{dt} = -|\gamma|\mathbf{M}(\mathbf{r},t)\times\mathbf{H}_{\text{eff}}(\mathbf{r},t) + \text{loss}. \tag{2.43}$$

This additional loss term causes the magnetization to relax into equilibrium position if pump is turned off. In subsequent sections, the most popular phenomenological models will be discussed – Landau-Lifshitz, Gilbert, and Bloch-Bloembergen model. The analysis will be presented for the uniform mode alone since it is the uniform mode relaxation rate which is of interest in the ferromagnetic resonance experiments.

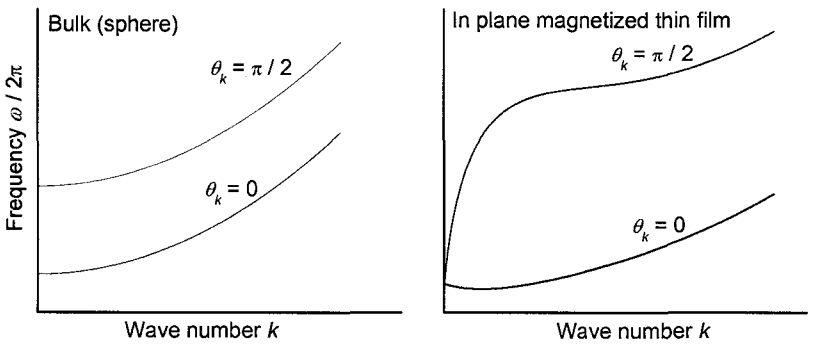

FIG. 2.4. Sketches of the spin wave dispersion in the magnetostatic approximation for (a) bulk sample, (b) for an in-plane magnetized thin film sample.

It will be shown that the uniform mode relaxation rate from the above mentioned phenomenological models can be expressed in terms of the uniform mode stiffness fields (2.16). It has been already shown in Sections 2.1.3 and 2.1.4 that with use of stiffness fields both the uniform and non-uniform mode (spin wave) eigenfrequencies, given by Eq. (2.18) and (2.37) respectively, can be analyzed in the same manner. The same conclusion applies for the relaxation rate. In order to obtain the spin wave relaxation rate from the phenomenological models discussed below, one would have to simply replace uniform stiffness fields by the non-uniform stiffness fields (2.36).

2.2.1 LANDAU-LIFSHITZ MODEL

Proposed in 1935, the Landau-Lifshitz (LL) relaxation model (Landau and Lifshitz 1935), was the first model of damped precession dynamics in a ferromagnetic sample. This model is particularly suitable for description of relaxation mechanism in thin metallic films. The LL equation is a modification of the torque equation Eq.

(2.5) with the addition of a damping term proportional to the component of the internal field perpendicular to the magnetization

$$\frac{d\mathbf{M}}{dt} = -|\gamma|\mathbf{M}\times\mathbf{H}_{\text{eff}} - |\gamma|\frac{\alpha_{\text{LL}}}{M_s}\mathbf{M}\times(\mathbf{M}\times\mathbf{H}_{\text{eff}}). \tag{2.44}$$

Here, α_{LL} is the unitless phenomenological Landau-Lifshitz damping constant. The LL damping term represents a relaxation of $\mathbf{M}$ towards the equilibrium direction of $\mathbf{H}_{\text{eff}}$, in such a way that the magnitude of $\mathbf{M}$ remains constant. Linearization of the Eq. (2.44) together with the small damping limit ($\alpha_{\text{LL}}^2 \ll 1$) yields modification of the uniform mode eigenfrequency as

$$\omega_0 \to i\eta_{\text{LL}} \pm \omega_0. \tag{2.45}$$

where the frequency ω_0 is again given by Eq. (2.18) and η_{LL} is the relaxation rate for LL damping

$$\eta_{\text{LL}} = \frac{|\gamma|\alpha_{\text{LL}}}{2}\left(\text{H}_{xx} + \text{H}_{yy}\right). \tag{2.46}$$

The term "relaxation rate" simply reflects the fact that the free motion of the magnetization is now described by exponentially decaying oscillations

$$m_{0x,y}(t) \propto \text{e}^{-\eta_{\text{LL}}t}\,\text{Re}\left\{\text{e}^{i\omega_0 t}\right\}. \tag{2.47}$$

The model ensures that the length of the magnetization vector $|\mathbf{M}|$ is preserved. This can be easily seen by the scalar multiplication of both sides of Eq. (2.44) by $\mathbf{M}$.

2.2.2 GILBERT MODEL

The Gilbert (G) damping model is akin to the damping of motion in a viscous medium (Gilbert 1955) (Gilbert 2004). The Gilbert equation is a modification of the torque equation with the addition of a relaxation term

$$\frac{d\mathbf{M}}{dt} = -|\gamma|\mathbf{M}\times\mathbf{H}_{\text{eff}} + \frac{\alpha_{\text{G}}}{M_s}\mathbf{M}\times\frac{d\mathbf{M}}{dt}, \tag{2.48}$$

where α_{G} is the dimensionless parameter known as the Gilbert damping parameter. In the small damping approximation ($\alpha_{\text{G}}^2 \ll 1$) the linearized Eq. (2.48) yields the same result for the eigenfrequency and the relaxation rate as for the LL damping, with α_{LL} replaced by α_{G}. It will be shown later that this relaxation rate also matches the one predicted by the theory of magnon-electron scattering. These models are therefore widely used for characterization of the intrinsic damping in metallic thin films. In further analysis the LL and G models will be treated as a single model with a damping constant $\alpha = \alpha_{\text{LL}} = \alpha_{\text{G}}$.

2.2.3 BLOCH–BLOEMBERGEN MODEL

The Bloch–Bloembergen (BB) model was initially introduced as a phenomenological description of paramagnetic relaxation, but it has also been used to describe ferromagnetic relaxation (Bloembergen and Wang 1953). This model considers the magnetization relaxation as a two-part process. When the

magnetization is perturbed from the static equilibrium, first the transverse x, y magnetization components relax to zero, while the longitudinal z component remains constant. Such a process does not conserve the length of the magnetization vector. It may be viewed therefore as a process that describes the relaxation of the average magnetization $\langle \mathbf{M} \rangle$, where the non-conservation of the length $|\langle \mathbf{M} \rangle|$ accounts for the excitation of non-uniform modes. In the linear regime such an excitation can be due to the so-called two-magnon process, which is related to scattering of the uniform magnetization mode on the sample inhomogeneities. After the relaxation to z direction the average magnetization relaxes back to the saturated value due to spin-lattice processes. This two-part relaxation process can be characterized by a transverse T_2 and a longitudinal T_1 relaxation time and the magnetization motion can be described by a pair of equations

$$\frac{d\mathbf{M}_{x,y}}{dt} = -|\gamma|\left(\mathbf{M} \times \mathbf{H}_{\text{eff}}\right)_{x,y} - \frac{\mathbf{M}_{x,y}}{T_2}, \tag{2.49}$$

and

$$\frac{d\mathbf{M}_z}{dt} = -|\gamma|\left(\mathbf{M} \times \mathbf{H}_{\text{eff}}\right)_z - \frac{\mathbf{M}_z - M_s}{T_1}, \tag{2.50}$$

The linear relaxation rate of the transverse magnetization components for the BB model is therefore

$$\eta_{\text{BB}} = \frac{1}{T_2}, \tag{2.51}$$

The BB equation written in the form (2.49) and (2.50) differs from the original BB formulation in a subtle, but important point. In the original formulation, transverse and longitudinal components of magnetization have been defined with respect to the direction of external static field, or in the X,Y,Z frame. In Eq. (2.49) and (2.50) these components are actually defined with respect to the direction of internal static field, or in the precessional x,y,z frame. This form is therefore also termed as Modified Bloch-Bloembergen (MBB) equation, (Kambersky and Patton 1975).

Equations (2.49) and (2.51) may be written as a single equation in vectorized form as

$$\frac{d\mathbf{M}}{dt} = -|\gamma|(\mathbf{M}\times\mathbf{H}) + \frac{1}{T_1}\frac{\mathbf{H}_{\text{eff}}}{H_{\text{eff}}^2}\left[M_s H_{\text{eff}} - \mathbf{M}\cdot\mathbf{H}_{\text{eff}}\right] + \frac{1}{T_2}\frac{1}{H_{\text{eff}}^2}\left[(\mathbf{M}\times\mathbf{H}_{\text{eff}})\times\mathbf{H}_{\text{eff}}\right]. \tag{2.52}$$

This vectorized form of BB equation was first reported in an American Physical Society meeting abstract by Codrington, Olds and Torrey (Codrington *et al.* 1954) and in a regular paper by Wangsness (Wangsness 1955). Therefore it will be termed the Codrington, Olds and Torrey (COT) equation.

2.2.4 CONSTRAINED CODRINGTON, OLDS AND TORREY MODEL

As discussed above, both BB (MBB) and COT models written in the form (2.49-2.50), or (2.52) respectively do not conserve the magnitude of magnetization $\mathbf{M}$.

Recently, Silva proposed a form of COT equation that conserves the magnitude of $\mathbf{M}$ (Silva, unpublished). It can be shown that the condition $|\mathbf{M}| = M_s$ requires

$$\frac{T_2}{T_1} = \frac{M_s H_{\text{eff}} + \mathbf{M}\cdot\mathbf{H}_{\text{eff}}}{\mathbf{M}\cdot\mathbf{H}_{\text{eff}}} \tag{2.53}$$

In the small signal limit when $M_s H_{\text{eff}} \approx \mathbf{M}\cdot\mathbf{H}_{\text{eff}}$ Eq. (2.53) reduces to known result for constrained BB equation $T_2 = 2T_1$. Under the condition (2.53) the COT equation (2.52) may be written in terms of transverse relaxation time T_2 alone

$$\frac{d\mathbf{M}}{dt} = -|\gamma|(\mathbf{M}\times\mathbf{H}) - \frac{1}{T_2}\frac{\mathbf{M}\times(\mathbf{M}\times\mathbf{H}_{\text{eff}})}{\mathbf{M}\cdot\mathbf{H}_{\text{eff}}}. \tag{2.54}$$

This form is referred to as constrained COT (CCOT) equation. Comparison with LL equation (2.44) yields the CCOT relaxation rate in the small signal limit

$$\eta_{\text{CCOT}} = \frac{1}{2T_2}\frac{\mathrm{H}_{xx} + \mathrm{H}_{yy}}{H_i},, \tag{2.55}$$

where $\mathrm{H}_{xx}, \mathrm{H}_{yy}$ are uniform stiffness fields and H_i is internal static field.

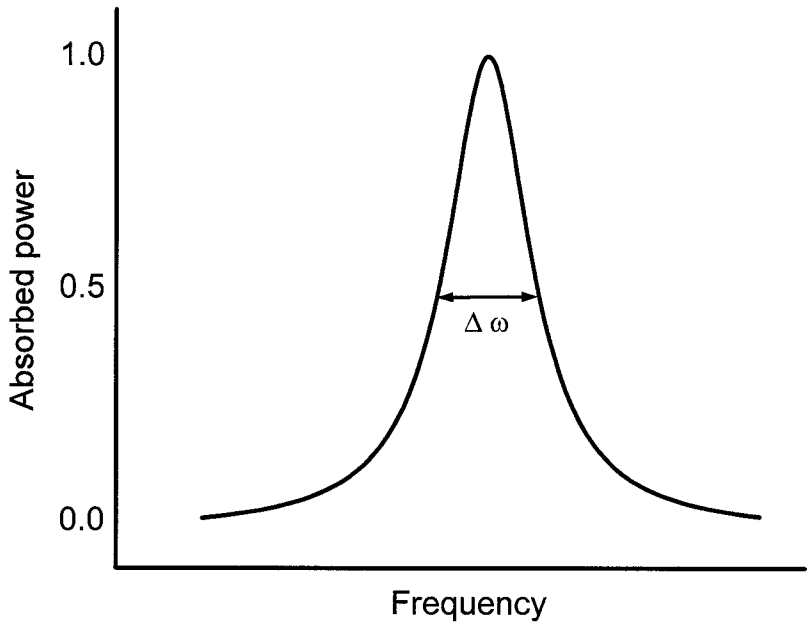

FIG. 2.5. Sketch of the frequency-swept absorbed power.

2.3 FREQUENCY AND FIELD LINEWIDTH

As discussed in the Section 2.2. for the linear case, the phenomenological damping terms in the torque equation yields an exponential decay of the free magnetization motion. This decay can be characterized by the relaxation rate η with field and/or frequency dependence specific for each phenomenological model. An experimental method of measuring η would be therefore to subject the sample initially with magnetization in the static equilibrium and a short field disturbance and to measure the transient response of the magnetization. This measurement technique was employed in the early works on magnetization relaxation (Wolf 1961) and also

recently with the use of the pulsed inductive microwave magnetometry (PIMM) developed at NIST, Boulder, CO (Kos *et al.* 2002), (Silva *et al.* 1999).

Another technique, invented in 1946 and since then widely used in the characterization of the relaxation parameters of magnetic materials, is ferromagnetic resonance (FMR) spectroscopy. This technique is based on the detection of the microwave power absorbed by the sample. The sample is subjected to continuous microwave excitation, with the transverse pump field of the form given by Eq. (2.20). In the usual FMR experiment, however, the pump field is linearly polarized so that only either $h_{px}(t)$ or $h_{py}(t)$ is non-zero. Then the average microwave power P_{abs} absorbed by the sample is proportional to the imaginary part of the corresponding diagonal component of the external susceptibility tensor $\ddot{\chi}_e$ (2.22)

$$P_{abs} = -\frac{1}{2}\omega\left|h_{px(y)}\right|^2 \operatorname{Im}\chi_{xx(yy)} . \tag{2.56}$$

Note that in the lossless case both χ_{xx} and χ_{yy} are real and P_{abs} is zero.

One can evaluate χ_{xx} and χ_{yy} for each specific phenomenological damping model discussed in the Section 2.2. However, since the relaxation rate η is much smaller than the resonance frequency ω_0, to a good approximation one can replace ω_0 with $i\eta + \omega_0$ in Eq. (2.22)

$$\chi_{xx(yy)} \approx \frac{|\gamma| M_s}{(i\eta + \omega_0)^2 - \omega^2}\omega_{yy(xx)} . \tag{2.57}$$

Close to the resonance point $\omega \approx \omega_0$ and for small damping, this equation may be further simplified as

$$\begin{aligned}\chi_{xx(yy)} &\approx \frac{|\gamma| M_s}{(i\eta + \omega_0)^2 - \omega^2} \omega_{yy(xx)} \\ &\approx \frac{|\gamma| M_s}{\omega_0^2 - \omega^2 + 2i\eta\omega_0} \omega_{yy(xx)} \\ &\approx \frac{1}{2\omega} \frac{|\gamma| M_s}{\omega_0 - \omega + i\eta} \omega_{yy(xx)} .\end{aligned} \tag{2.58}$$

The absorbed power P_{abs} is then given by

$$P_{\text{abs}} \approx \frac{1}{4} \left| h_{px(y)} \right|^2 |\gamma| M_s \, \omega_{yy(xx)} \frac{\eta}{(\omega_0 - \omega)^2 + \eta^2} . \tag{2.59}$$

Figure 2.5 shows a sketch of the frequency dependence of the absorbed power P_{abs}. This dependence has a nearly Lorentzian shape with the half-power frequency linewidth given by

$$\Delta\omega = 2\eta . \tag{2.60}$$

Hence, the frequency-swept detection of the absorbed power P_{abs} yields directly the magnetization relaxation rate η.

In the usual FMR experiment, the microwave pump frequency ω is fixed and the external static field H is varied. The field-swept dependence of absorbed power again resembles a Lorentzian shape with the half-power field linewidth ΔH. The connection between $\Delta\omega$ and ΔH can be found from the relation

$$\Delta\omega = |\gamma|\Delta H \cdot \left.\frac{\partial\omega_0}{\partial|\gamma|H}\right|_{\text{FMR}} = |\gamma|\Delta H \cdot P_A(\omega_0). \tag{2.61}$$

Here, the derivative is evaluated at the FMR point. This type of conversion has been discussed in (Patton 1968), (Patton 1975), (Kuanr *et al.* 2005) and most recently in (Kalarickal *et al.* 2006). The *ellipticity factor* $P_A(\omega_0)$ factor defined above provides a convenient way to account for the ellipticity of the FMR response in relaxation rate and linewidth analyses (Kuanr *et al.* 2005). This factor can be evaluated from Eqs. (2.16)-(2.18). If the experimental configuration is chosen in such a way that $H_z = H$ then this factor is

$$P_A(\omega_0) = \left.\frac{\partial\omega_0}{\partial|\gamma|H}\right|_{\text{FMR}} = \frac{1}{2\omega_0}\left(\omega_{xx} + \omega_{yy}\right). \tag{2.62}$$

In the field swept experiment, the derivative $\partial P_{\text{abs}}/\partial H$ is often measured with use of the lock-in technique. The so-called *derivative linewidth* ΔH_d is then defined as a field difference between the extrema of $\partial P_{\text{abs}}/\partial H$ vs. H curve. For a Lorentzian shape the connection between half-power ΔH and the derivative ΔH_d linewidth is

$$\Delta H = \sqrt{3}\,\Delta H_d \tag{2.63}$$

Details on the FMR experimental setup used in this dissertation will be discussed in the Chapter 3.

2.4 PHYSICAL CONTRIBUTIONS TO THE FMR LINEWIDTH

In section 2.2 the magnetization relaxation was treated purely phenomenologically. The common feature of the discussed phenomenological models that is, the tendency of the magnetization vector to relax to the static equilibrium position, was included in torque equation more-or-less on the grounds of geometrical arguments. In the subsequent section, the relation between the magnetization relaxation rate and the measurable quantities in the FMR experiment: frequency, or field linewidth respectively, was discussed. It was also pointed out that the uniform microwave pump field excites the uniform magnetization mode alone. The linewidth therefore reflects the relaxation of the uniform mode relaxation. However, two questions arise: what physical processes would determine the relaxation and the measured linewidths, and how do these processes relate to the discussed phenomenological models?

Broadly speaking, there are three important physical contributions to FMR linewidths: (i) the direct dissipation of the uniform mode energy, (ii) the flow of the uniform mode energy into non-uniform magnetic modes, and (iii) inhomogeneous linewidth broadening due to spread of the localized resonance frequencies.

The first relaxation mechanism, also termed as the intrinsic damping, has its origin in the coupling between magnetic system and the other systems: lattice, conduction electrons, etc. In the corpuscular language, this coupling corresponds to the scattering of the magnetization quanta, magnons, to the lattice vibration modes

(phonons) or to other non-magnetic systems (conduction electrons, for example). In metallic samples, the intrinsic damping due to magnon-electron scattering is a well-pronounced contribution to the relaxation rate. This damping mechanism will be discussed in Section 2.4.1. On the other hand, the intrinsic damping in the ferrite samples used in this dissertation is much smaller than the contributions from other mechanisms and will be neglected.

The second contribution to relaxation is the coupling between magnetization modes themselves. This coupling is due either to the non-linearity of the magnetization motion, or to the scattering of the uniform mode on the sample imperfections and inhomogeneities. In low-power FMR experiments, the non-linear coupling may be neglected. On the other hand, the coupling via the inhomogeneity-produced fields can be considerably strong even in the linear magnetization regime and it is one of the most pronounced contributions to the linewidth. Such a mechanism is called two-magnon scattering and it will be discussed in detail in the Section 2.4.2. This contribution was known to be a dominant one for polycrystalline ferrite samples and is also fairly important for metallic thin films used in this dissertation.

The last contribution to the linewidth differs significantly from the previous two ones. Similar to the two-magnon scattering, it is related to the presence of the inhomogeneities in the sample, but it is not a relaxation process. Regions with slightly different magnetic properties, grains in a polycrystalline sample for example, may have slightly different resonance frequencies. This spread of resonance

frequencies is related to the distribution in local effective fields. As a result, instead of a single resonance peak one observes a superposition of several resonances and consequently an increase in the measured linewidth. This line broadening will be discussed in Section 2.4.3.

2.4.1 MAGNON-ELECTRON SCATTERING

FMR experiments on high quality Ni samples showed that the intrinsic damping in metals is caused by the itinerant nature of the electrons and the spin orbit interaction. (Heinrich 2003) Heinrich and other workers in the field introduced a model based on the s-d exchange interaction, which considers the interaction between the itinerant (s-electrons) and the localized (d-electrons). Magnons and electrons are scattered coherently, a process that is then disrupted by incoherent scattering with other excitations like thermally excited phonons and magnons. This results in a fast fluctuating torque, resulting in magnetic relaxation. A calculation of the microwave susceptibility then shows that the energy of a resonant magnon is the energy which participates in the scattering process (Heinrich 2003) (Heinrich *et al.* 2002).

In other words, the s-d exchange interaction can be viewed as interaction of two precessing magnetic moments corresponding to the d-localized and itinerant electrons coupled by s-d exchange field. In the absence of damping, the excitation corresponds to a parallel alignment of the magnetic moments precessing together in phase. However, due to the finite spin mean free path of the itinerant electrons, the

equation of motion for these electrons has to include spin relaxation towards the instantaneous effective field, which includes the s-d exchange coupling field. This results in a phase lag between the two precessing magnetic moments and hence in magnetic damping (Vonsovskii 1961). This process gives a linewidth proportional to the frequency, similar to the LL or G formulation of relaxation.

Another physical description of intrinsic damping is Kambersky's model, which is based on the observation that the Fermi surface changes with the direction of the magnetization (Kambersky 1976). This model corresponds to intraband transitions. As the precession of the magnetization evolves in space and time, the Fermi surface also distorts periodically. The repopulation of the changing Fermi surface by the electrons is delayed by a finite relaxation time of the electrons. In both cases, one gets a viscous type of damping, which is described by the phenomenological LL or G model.

Based on a three particle confluence process, the relaxation rate for the uniform mode precession is given by (Kamberský and Patton 1975),

$$\eta_{\mathrm{me}} = \alpha_{\mathrm{me}} \omega P_A, \tag{2.64}$$

where α_{me} is a scattering summation, which is an intrinsic parameter depending the interaction of the uniform mode with other excitations, ω is uniform mode frequency and P_A is the ellipticity factor given by Eq. (2.62). The corresponding frequency swept linewidth is given by

$$\Delta\omega_{\text{me}} = 2\eta_{\text{me}} = \alpha_{\text{me}}\left(\omega_{xx} + \omega_{yy}\right). \tag{2.65}$$

The field swept linewidth for magnon-electron scattering is then given by

$$\Delta H_{\text{me}} = \frac{2\alpha_{\text{me}}\omega}{|\gamma|}. \tag{2.66}$$

The field swept linewidth is linear in frequency. This linear frequency dependence of linewidth has been widely observed for ferromagnetic metals. The predicted temperature dependence of the damping parameter was observed in high quality Ni samples, showing that the intrinsic damping in Ni was caused by the itinerant nature of the electrons and spin orbit interactions (Heinrich 2003) . The damping parameter α_{me} for Ni was found to be 0.005, which is the same as the Gilbert or LL damping parameter for this metal.

2.4.2 TWO-MAGNON SCATTERING

In early FMR works on ferrite samples, it was observed that the linewidths were substantially larger than expected from intrinsic damping processes. This discrepancy was later attributed to the presence of sample imperfections that induce an additional coupling between the uniform ($k = 0$) magnetization mode and degenerate non-uniform ($k \neq 0$) modes (spin waves). The origin of this coupling may vary: dipolar field due to voids, pores, surface pits; the variation in the direction of magnetocrystalline anisotropy in polycrystalline samples; magnetostrictive

coupling due to non-uniform stresses etc (Sparks 1964). This relaxation mechanism is referred to as two-magnon scattering (TMS).

In 1956, Clogston *et al.* for the first time recognized the role of degenerate spin waves in the uniform mode relaxation (Clogston *et al.* 1956). In 1958, LeCraw *et al.* (LeCraw *et al.* 1958) observed that the FMR linewidth in a series of single crystal YIG spheres was related to the grit size of the polishing paper. In their seminal theoretical paper, Sparks *et al.* explained this increase in linewidth by the scattering of the uniform mode from the dipolar field produced by surface pits (Sparks *et al.* 1961). In polycrystalline samples scattering may occur from the dipolar fields produced by pores between grains and/or from the random orientation of the local anisotropy axes in the grains. Theoretical treatment of the porosity scattering is similar to the surface pits scattering. A basic theory for the anisotropy scattering was outlined by Schloemann in 1958 (Schloemann 1958). Two-magnon scattering for samples other than spherical in shape was discussed by Sparks (Sparks 1970) and Hurben and Patton (Hurben and Patton 1998) for the particular case of a thin ferrite film.

For the case of thin metallic films, a model of two-magnon scattering was presented recently by Arias and Mills (Arias and Mills 1999). This model dealt with scattering from regularly shaped surface defects due to dipolar fields and a variation in the surface anisotropy direction. In 2004, McMichael and Krivosik established the classical model of TMS relaxation for thin films with random anisotropy scattering (McMichael and Krivosik 2004). The TMS contribution to relaxation rate

due to surface roughness during large angle switching was treated theoretically by Dobin and Vittoria (Dobin and Vittoria 2004). Experimental evidence of TMS contribution to the linewidth in thin metallic films was presented in (Bertaud and Pascard 1965), (McMichael *et al.* 1998) and (Lenz *et al.* 2006).

The methods used in the theoretical study of TMS relaxation vary. The most widely used are the transition probability method and the method of coupled equations of motion. In the transition probability method, relaxation is taken as a transition of the magnetic system from one state to the other. The uniform mode relaxation rate is the number of such transitions per unit time that yields the annihilation of the uniform mode magnon and creation of non-uniform mode magnon. Quantum mechanical perturbation theory is used to calculate transition probability and the relaxation rate. This method was used, for example in (Sparks *et al.* 1961) and (Seiden and Sparks 1965).

In the method of coupled equations of motion, the inhomogeneity coupling is introduced either as an additional field in the magnetization torque equation, or as an additional energy term in the Hamiltonian. The equation of motion for the uniform mode similar to Eq. (2.15), has a solution which yields the uniform mode susceptibility with an additional term in the relaxation parameter. This additional term is associated with two-magnon scattering. This method was used, for example, in (Schloemann 1958) (McMichael and Krivosik 2004).

Both the methods yield an equivalent result for the TMS relaxation rate η_{TMS}. This result may be written in a form similar to the quantum-mechanical Fermi's Golden Rule

$$\eta_{\mathrm{TMS}} = \pi \sum_{\mathbf{k}} \left| \mathcal{W}_{0\mathbf{k}} \right|^2 \delta(\omega_0 - \omega_{\mathbf{k}}). \tag{2.67}$$

Here, $\left|\mathcal{W}_{0\mathbf{k}}\right|^2$ is the coupling strength between the uniform mode and a non-uniform mode characterized by the wave vector $\mathbf{k}$. This coupling strength generally depends on the type of the scattering process and distribution and size of imperfections. The delta function in Eq. (2.67) conserves the energy $\hbar\omega$ in TMS process. This conservation of energy therefore requires frequency degeneracy in the spin-wave dispersion.

As shown in Fig. 2.4, the spin-wave dispersion for bulk sample and thin film are qualitatively different. Therefore, although Eq. (2.67) is applicable in both cases, the result for η_{TMS} and its frequency/field dependence is qualitatively different for a bulk sample (a sphere) and a thin film.

2.4.2 A Two-magnon scattering in a polycrystalline ferrite sample

Two-magnon scattering theory for a polycrystalline ferrite sample with randomly oriented magnetocrystalline anisotropy in the individual grains was developed by Schloemann (Schloemann 1958). The theory yields a result for TMS relaxation rate in the form of Eq. (2.67) with

$$|\mathcal{W}_{0\mathbf{k}}|^2 = \frac{4}{105}(|\gamma|H_A)^2 \times\left(1+19|\gamma|\frac{H_i + Dk^2 + 2\pi M_s \sin^2\theta_k}{\omega}\right)g(k). \tag{2.68}$$

Here, $H_A = K_1 / M_s$ is the anisotropy field, with magnetocrystalline cubic anisotropy constant K_1. Other parameters have been already introduced in Section 2.1.1 and 2.1.2: γ is the gyromagnetic ratio, H_i is the internal static field, and D is the exchange constant. Note that for a sphere $H_i = H - 4\pi M_s / 3$. As already shown in Fig. 2.3a, k and θ_k are the wavevector magnitude and the polar angle of spin-wave propagation, respectively. The function $g(k)$ accounts for the distribution and size of the grains. For randomly distributed directions of magnetocrystalline axes, this function takes the form (Schloemann 1958),

$$g(k) = \frac{1}{V}\frac{8\pi\xi^3}{\left[1+(k\xi)^2\right]^2}, \tag{2.69}$$

where ξ is the mean grain size and V is the sample volume. The function $g(k)$ falls rapidly for $k \gg 1/\xi$ and accounts for the fact that the uniform mode is mostly scattered to the spin waves with wavelengths of the order of the grain size. Therefore, in a coarse grained sample, the scattering is limited to relatively low-k spin waves.

The mutual relation between the degenerate spin waves, wave numbers and the grain size is in fact one of the most important factors in the TMS analysis. In order to elucidate this point, Fig. 2.6 shows the spin wave dispersion for different pump frequencies calculated for case of a YIG sphere. The spin wave dispersion was calculated for the nominal parameters $|\gamma|/2\pi$=2.8 MHz/Oe, $4\pi M_s$=1750 G, and $D = 5.19\times10^{-9}$ Oe-cm^2/rad^2. The dashed lines refer to the pump frequency. For each frequency, the external field corresponds to the FMR value $H = \omega/|\gamma|$. As shown in graphs (a) and (b), the pump frequency less than $(2/3)(|\gamma|4\pi M_s) \approx 3.27$ GHz lies outside of the $k = 0$ limits of spin wave manifold.

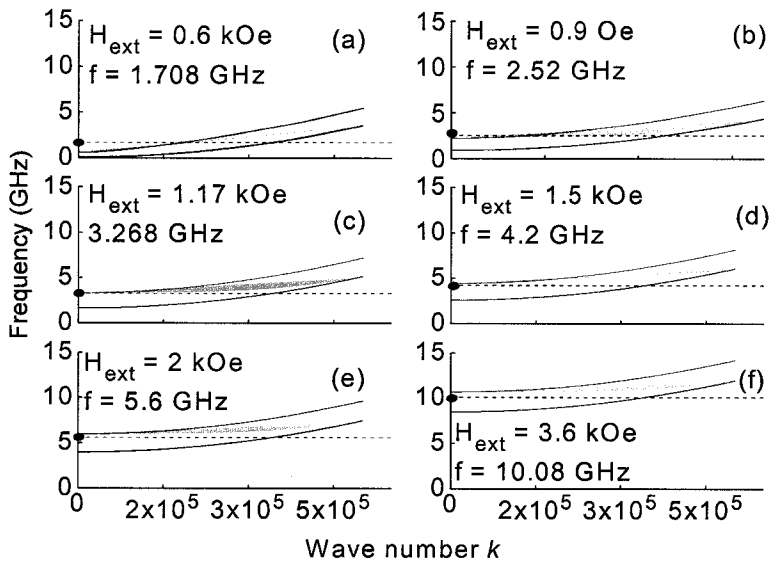

FIG 2.6 Spin wave manifold for a sphere, for different frequencies as shown. In all graphs the red curve shows the dispersion for $\theta_k = 90$ degrees while the black curve shows the dispersion for $\theta_k = 0$ degree. The dashed line refers to the FMR frequency.

The excited uniform mode is therefore degenerate with the high-k spin waves. At $\omega/2\pi = (2/3)(|\gamma|4\pi M_S)$ the uniform mode is excited at the upper limit of the spin wave manifold, as shown in graph (c). Hence the number of spin waves degenerate with the uniform mode is the maximum. Above the frequency $(2/3)(|\gamma|4\pi M_S)$ the uniform mode is excited within the spin wave manifold and the TMS scattering to low-k spin waves is allowed. One can therefore expects a strong frequency dependence of TMS relaxation rate with a peak at the frequency $(2/3)(|\gamma|4\pi M_S) \approx 3.27$ GHz and abrupt fall below this frequency. Such a behavior was actually observed and will be shown and discussed in Chapter 5.

In the limiting case of scattering to $k \to 0$ spin waves, the two-magnon anisotropy relaxation rate η_{TMAS} can be evaluated analytically with the use of Eqs. (2.67) - (2.69). It was shown by Schloemann (Schloemann 1958) that the result is

$$\eta_{\text{TMAS}} \simeq |\gamma| \frac{16\pi\sqrt{3}}{21} \frac{H_A^2}{4\pi M_S} G\left(\frac{\omega}{\omega_M}\right), \tag{2.70}$$

where $\omega_M = |\gamma|4\pi M_S$ and

$$G(x) = \begin{cases} \dfrac{x^2 - x/3 + 19/360}{\sqrt{(x-1/3)^3 (x-2/3)}}, & x > 2/3, \\ 0, & x \le 2/3. \end{cases} \tag{2.71}$$

The field swept linewidth from Eqs. (2.69), (2.59) and (2.60) is

$$\Delta H_{\mathrm{TMAS}} = \frac{2\eta_{\mathrm{TMAS}}}{|\gamma|} \approx 8.3 \frac{H_A^2}{4\pi M_s} G\left(\frac{\omega}{\omega_M}\right). \tag{2.72}$$

Recall that for a sphere the ellipticity factor $P_A(\omega_0) = 1$.

2.4.2 B Two-magnon scattering in thin films

As was discussed in the introduction to this section, the general result for TMS relaxation rate (2.67) is applicable both to bulk and thin film samples. However, the difference in the linewidth frequency/field dependence between bulk samples and thin films is due to several factors. Firstly, the spin-wave dispersion is very different. For a very thin film, the spin wave propagation is confined to the film plane. This leads to a strong dependence of TMS relaxation rate on the magnetization angle with respect to the film normal. Secondly, the defect size is usually smaller than those in bulk polycrystalline ferrites and the scattering to relatively large k values is therefore allowed. It was shown in (McMichael and Krivosik 2004), (Krivosik and Patton 2006) (Krivosik *et al.* 2004) that for a thin film, the coupling strength in Eq. (2.67) may be written as

$$|\mathcal{V}_{0\mathbf{k}}|^2 \simeq \langle \delta\omega_0^2(\mathbf{r}) \rangle c(k), \tag{2.73}$$

where $\delta\omega_0(\mathbf{r})$ is a spatial variation of the uniform mode resonance frequency ω_0, $\langle \cdots \rangle$ represents a averaging over the sample, and $c(k)$ has the same meaning as the function $g(k)$ in Eq. (2.68). The difference is in the dimensionality of the

$\mathbf{k}-$space. The $g(k)$ function was evaluated for 3D (bulk) sample, while the $c(k)$ function is evaluated for 2D (planar) configuration. The $c(k)$ function takes the form (McMichael and Krivosik 2004)

$$c(k)=\frac{1}{A}\frac{2\pi\xi^2}{\left[1+(k\xi)^2\right]^{3/2}}, \tag{2.74}$$

where A is the film area and ξ again represents the mean size of planar defects.

The spatial variation $\delta\omega_0(\mathbf{r})$ can be formally evaluated from Eq. (2.18). Assume that the inhomogeneities induce a small local variation of the uniform mode stiffness fields (2.16) or, equivalently, a variation of the uniform mode stiffness frequencies (2.17). In Eq. (2.18) for the uniform mode frequency one can replace ω_{xx} by approximately $\omega_{xx}+\delta\omega_{xx}(\mathbf{r})$ etc. and evaluate the variation of ω_0 as

$$\begin{aligned}\delta\omega_0(\mathbf{r}) &\approx \frac{\partial\omega_0}{\partial\omega_{xx}}\delta\omega_{xx}(\mathbf{r})+\frac{\partial\omega_0}{\partial\omega_{yy}}\delta\omega_{yy}(\mathbf{r})+\frac{\partial\omega_0}{\partial\omega_{xy}}\delta\omega_{xy}(\mathbf{r}) \\ &= \frac{1}{2\omega_0}\left[\omega_{xx}\delta\omega_{yy}(\mathbf{r})+\omega_{yy}\delta\omega_{xx}(\mathbf{r})-2\omega_{xy}\delta\omega_{xy}(\mathbf{r})\right].\end{aligned} \tag{2.75}$$

As discussed already, for an in-plane or perpendicularly magnetized thin film the demagnetizing tensor is diagonal and therefore $\omega_{xy}=0$. In addition, under the assumption that the variation of the stiffness frequencies does not differ significantly,

one can write $\delta\omega_{xx}(\mathbf{r}) \approx \delta\omega_{yy}(\mathbf{r}) \equiv |\gamma|\delta h(\mathbf{r})$, where $\delta h(\mathbf{r})$ is the spatial fluctuation of the field induced by the inhomogeneity. Therefore, from Eq. (2.75)

$$\begin{aligned}\delta\omega_0(\mathbf{r}) &\approx \frac{|\gamma|}{2\omega_0}(\omega_{xx}+\omega_{yy})\delta h(\mathbf{r}) \\ &= |\gamma| P_A(\omega)\delta h(\mathbf{r}),\end{aligned} \tag{2.76}$$

where $P_A(\omega)$ is the ellipticity factor already introduced in Eq.(2.61).

In the last step, one can replace summation in Eq. (2.67) by an integral

$$\sum_k \rightarrow \frac{A}{(2\pi)^2}\int d\mathbf{k}. \tag{2.77}$$

The result for TMS scattering rate then comprises Eqs. (2.67) and (2.73) - (2.77).

$$\eta_{\mathrm{TMS}} \approx \frac{|\gamma|^2}{2} P_A^2(\omega_0)\left\langle \delta h^2(\mathbf{r})\right\rangle \xi^2 \int \frac{\delta(\omega_0-\omega_{\mathbf{k}})}{\left[1+(k\xi)^2\right]^{3/2}} d\mathbf{k}. \tag{2.78}$$

The corresponding field linewidth ΔH_{TMS} is therefore

$$\begin{aligned}\Delta H_{\mathrm{TMS}} &= \frac{2\eta_{\mathrm{TMS}}}{|\gamma|}\frac{1}{P_A(\omega_0)} \\ &\approx |\gamma| P_A(\omega_0)\left\langle \delta h^2(\mathbf{r})\right\rangle \xi^2 \int \frac{\delta(\omega_0-\omega_{\mathbf{k}})}{\left[1+(k\xi)^2\right]^{3/2}} d\mathbf{k}.\end{aligned} \tag{2.79}$$

The coupling strength due to inhomogeneities is represented by the $\left\langle \delta h^2(\mathbf{r})\right\rangle \xi^2$ factor in Eq. (2.78). In the small defects size limit ($k\xi \ll 1$) and for a very thin film ($kd \ll 1$, where d is the film thickness) the integral in Eq. (2.79) can be evaluated

analytically (McMichael and Krivosik 2004) (Arias and Mills 1999). For an in-plane magnetized thin film the result is given by

$$\int \frac{\delta(\omega_0 - \omega_{\mathbf{k}})}{\left[1+(k\xi)^2\right]^{3/2}} d\mathbf{k} \approx \frac{4}{|\gamma| D} \frac{1}{P_A(\omega_0)} \operatorname{asin}\left(\frac{H}{H+4\pi M_s}\right)^{1/2}, \tag{2.80}$$

where D is the exchange constant. The approximate result for the contribution to the linewidth may be therefore written in a simple form:

$$\Delta H_{\mathrm{TMS}} \approx \frac{4}{D}\left\langle \delta h^2(\mathbf{r})\right\rangle \xi^2 \operatorname{asin}\left(\frac{H}{H+4\pi M_s}\right)^{1/2}. \tag{2.81}$$

One can see from Eq. (2.81) that the inhomogeneity field variation is narrowed both by exchange and dipolar interactions. For a film with a large saturation magnetization and for a small field $H \ll 4\pi M_s$, the asin factor in Eq. (2.80) may be approximated to

$$\operatorname{asin}\left(\frac{H}{H+4\pi M_s}\right)^{1/2} \approx \left(\frac{H}{H+4\pi M_s}\right)^{1/2} \approx \frac{\omega_0}{|\gamma| 4\pi M_s} \tag{2.82}$$

The frequency dependence of ΔH_{TMS} for ultra thin film, with small defects and at low fields (frequencies) is therefore linear, similar to the LL or G damping. For Permalloy, for example, the approximation (2.82) is valid up to 10 GHz. Two-magnon scattering may therefore produce an artificial overestimation of the intrinsic damping parameter α.

2.4.3 INHOMOGENEOUS LINE BROADENING

Besides the intrinsic damping which may be described phemenologically, some degree of linewidth increase can be expected due to inhomogeneities. There are several sources of inhomogeneous linebroadening, such as inhomogeneous applied fields, surface demagnetization across the sample, variation in the demagnetization fields of surface pits, or porosity in polycrystalline samples, etc. An interpretation of linewidth solely as due to intrinsic damping would therefore give an artificially high estimate of the damping parameter. The degree of linebroadening caused by these inhomogeneities depends on the relative strengths of the effective inhomogeneous field and the exchange and dipolar interactions. If the effective inhomogeneity fields are much stronger than the interactions, then the film can be treated as a collection of non-interacting regions where the magnetization will resonate at different fields. Thus an inhomogenously broadened line consists of a superposition of narrower lines. This is the local resonance model, and it has been widely used to describe the frequency dependence of linewidth in metal films. (Heinrich 2003) Generally for inhomogeneous line broadening, the representation is achieved by adding a constant value of linewidth to the intrinsic part of the linewidth.

$$\Delta H_{\text{total}}(\omega) = \Delta H_{\text{inhom}} + \Delta H_{\text{int}}(\omega), \tag{2.83}$$

where $\Delta H_{\text{int}}(\omega)$ is the frequency dependent intrinsic linewidth. This zero-frequency linewidth found in many ferromagnetic metallic thin films including single crystal Fe (Celinski and Heinrich 1991) and Pemalloy (Patton *et al.* 1975) films evidently has

origin in the surface or interface quality. It has also been suggested that two-magnon scattering may be responsible for this intercept.(Heinrich *et al.* 1985)

2.4.4 RIPPLE FIELD EFFECT

Spatial variations of the anisotropy amplitude or its angular variation from grain to grain can also result in the broadening of FMR lines. Broadening can also be studied using the magnetization ripple concept, which has its origin in the anisotropy dispersion. (Hoffman 1968) (Harte 1968) Ripple is a wavelike structure in the local magnetization that balances the randomness of the anisotropy angular dispersion. Therefore, there is a significant smoothing effect of the exchange forces. The broadening of a line shape comes from local changes in the resonance frequency due to the so-called ripple field produced by the magnetization ripple. The Kittel equation is then modified (Rantschler and Alexander 2003) to include this ripple field as

$$\omega = |\gamma| \sqrt{\begin{matrix}[H + H_k \cos 2\theta + H_d(H)] \times \\ [H + H_k \cos^2 \theta + H_d(H) + 4\pi M_s]\end{matrix}}, \tag{2.84}$$

Here, H_k is the field of the uniaxial anisotropy and θ is the angle which the magnetization makes with the easy axis. The term $H_d(H)$ is the average demagnetizing field due to the ripple, parallel to external static field **H**. The magnitude of $H_d(H)$ varies with the magnitude of the static field as

$$H_d(H) = \frac{H_r H_k^{1/4}}{(H + H_k \cos 2\theta)^{1/4}}. \quad (2.85)$$

Here, H_r is the ripple field parameter which depends on the anisotropy, film thickness, mean grain size, and angular dispersion of the magnetization ripple. (Hofmann) It was proposed in (Rantschler and Alexander 2003) that the linebroadening is simply proportional to the demagnetizing field (2.85). The total linewidth comprises ripple linebroadening and intrinsic part

$$\Delta H = \Delta H_{\text{int}} + \frac{H_r H_k^{1/4}}{(H + H_k \cos 2\theta)^{1/4}}. \quad (2.86)$$

In addition to the above line broadening contributions, the magnetic damping in metallic films in particular, can also be affected by eddy currents. (Heinrich 2003) This has been elaborated in Chapter 3, where the role of eddy current contribution to the broadening of the FMR line in Permalloy films has been considered.

2.5 LINEWIDTH AS A FUNCTION OF FREQUENCY: A COMPARISON OF DIFFERENT MODELS

The previous sections outlined various models describing ferromagnetic resonance relaxation. This section will briefly lay out the frequency dependences of FMR linewidth as predicted by these models and make comparisons. Figure 2.7 compares the calculated frequency dependences of the frequency swept linewidth for Landau-Lifshitz (LL), Gilbert (G), Bloch–Bloembergen (BB), constrained Codrington, Olds

and Torrey (CCOT), and the magnon electron scattering (me) models as a function of frequency for an in-plane magnetized thin film geometry. The parameters used for the calculation are, the saturation magnetization $4\pi M_s = 10$ kG, the transverse relaxation time $T_2 = 120$ ns and the LL/G/me damping parameter $\alpha = 0.005$. The value of $\alpha = 0.005$ is a typical value for metal films. The values for different models parameters have been chosen to show the responses clearly. The LL/G/magnon electron models all give the same response in the small signal limit. The $\Delta\omega$ values for these models show a small upturn as the frequency is increased. The BB model is based on a constant relaxation rate, hence the $\Delta\omega$ values for this model remains constant. The CCOT model shows a sharp upturn in the $\Delta\omega$ values for low frequencies due to the $1/H_i$ factor in Eq. (2.55). For higher frequencies however, these values drop drastically.

Figure 2.8 compares the calculated field swept linewidth for for Landau-Lifshitz (LL), Gilbert (G), Bloch–Bloembergen (BB), constrained Codrington, Olds and Torrey (CCOT), and the magnon electron scattering (me) models, as a function of frequency. The parameters used in the calculations are same as those for the curves in Fig 2.7. The conversion from the frequency swept to the field swept linewidth has been done as per Eq. (2.61). Here too, the LL/G/magnon electron models all give the same response in the small signal limit. The ΔH values for these models give a linear dependence in frequency with a zero intercept. For the BB model, the ΔH values looks linear in the frequency range shown. The CCOT model shows an

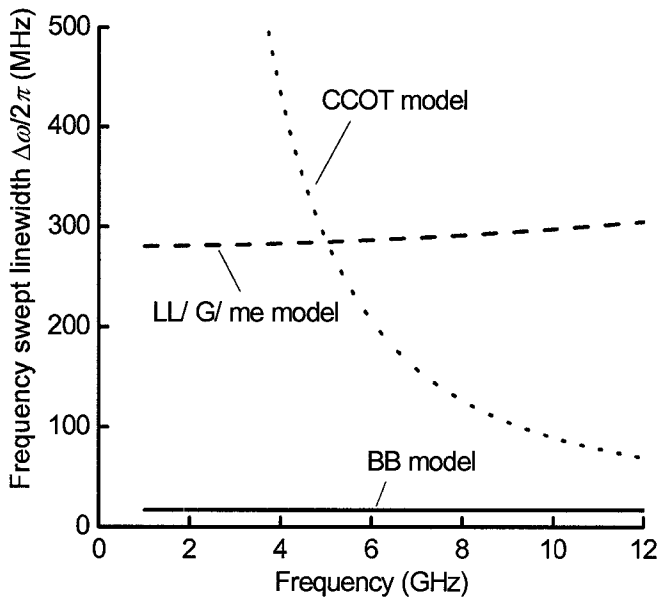

FIG. 2.7. Comparisons of the in plane frequency swept linewidth for different models as indicated. The solid line is due to the BB model, the dashed line is due to the LL/G/me model, and the dotted line is due to the CCOT model.

upturn in the ΔH values for low frequencies. For higher frequencies however these values drop drastically.

Figure 2.9 compares the calculated frequency dependences of the frequency swept linewidth for line broadening due to local field inhomogeneities and due to the ripple field effect. Both the mechanisms give $\Delta\omega$ values that increase at lower frequencies. However, the effect of the ripple field gives a sharper increase as compared to the local inhomogeneities.

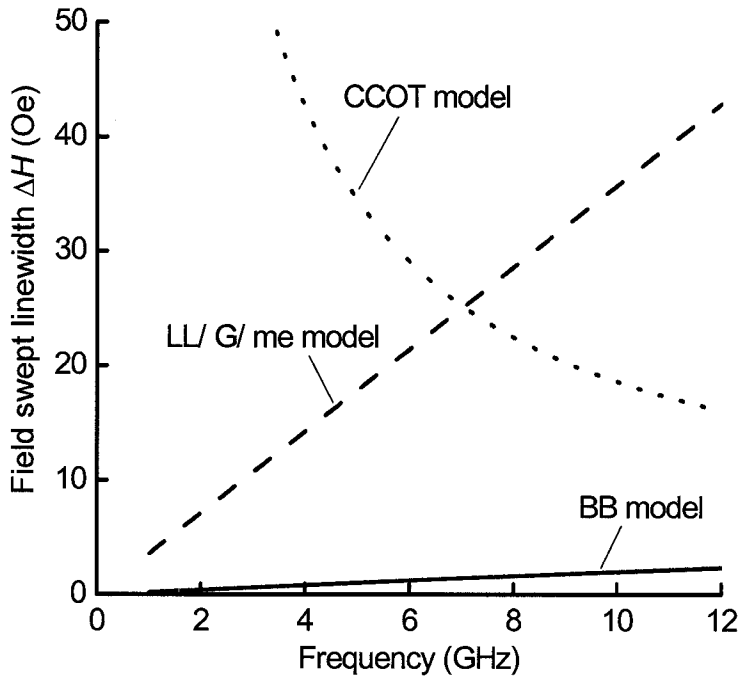

FIG. 2.8. Comparisons of the in plane field swept linewidth for different models as indicated. The solid line is due to the BB model, the dashed line is due to the LL/G/me model, and the dotted line is due to the CCOT model.

Figure 2.10 compares the calculated frequency dependences of the field swept linewidth for line broadening due to local field inhomogeneities and due to the ripple field effect. The ΔH values due to inhomogneities is a constant whereas for the ripple field, the ΔH is frequency dependent with a decrease as the frequency is increased. Note that the ripple field effect becomes prominent at lower frequencies, especially for the frequencies below 2 GHz.

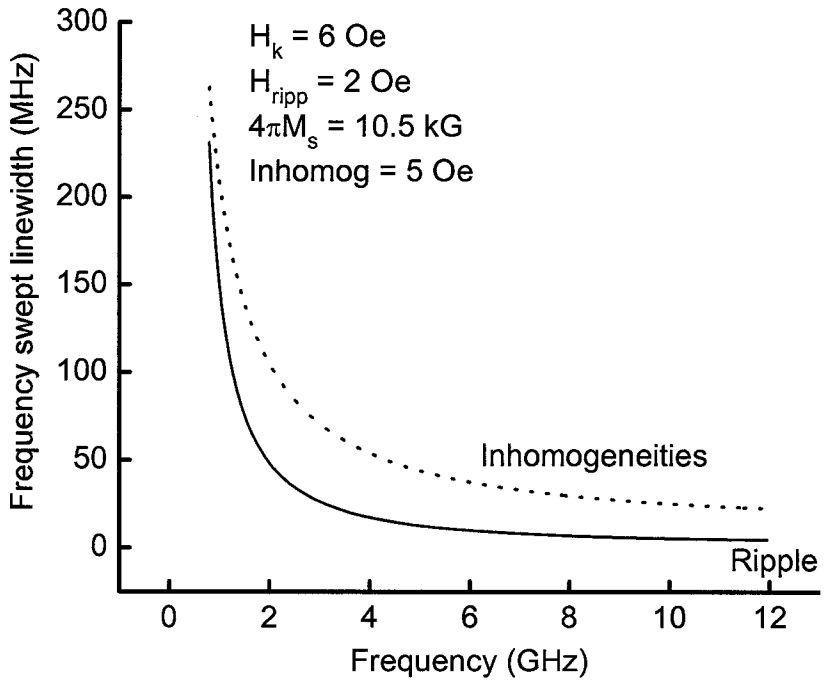

FIG. 2.9. Comparisons of the in plane frequency swept linewidth contribution for different linebroadening models as indicated. The dashed line is due to the inhomogeneity model, the solid line is due to the ripple field effect.

These frequency dependences of linewidth are evidently different. In real samples, the trend can be a combination of two or more of these mechanisms, as will be seen in the experimental results in the Chapters to follow.

2.6 SUMMARY

This chapter has introduced ferromagnetic resonance and has given the working equations for the resonance positions. It has also outlined several models, which attempt to describe relaxation in ferromagnetic materials in bulk and thin films. The phenomenological models as proposed by Landau and Lifshitz, Gilbert and Bloch

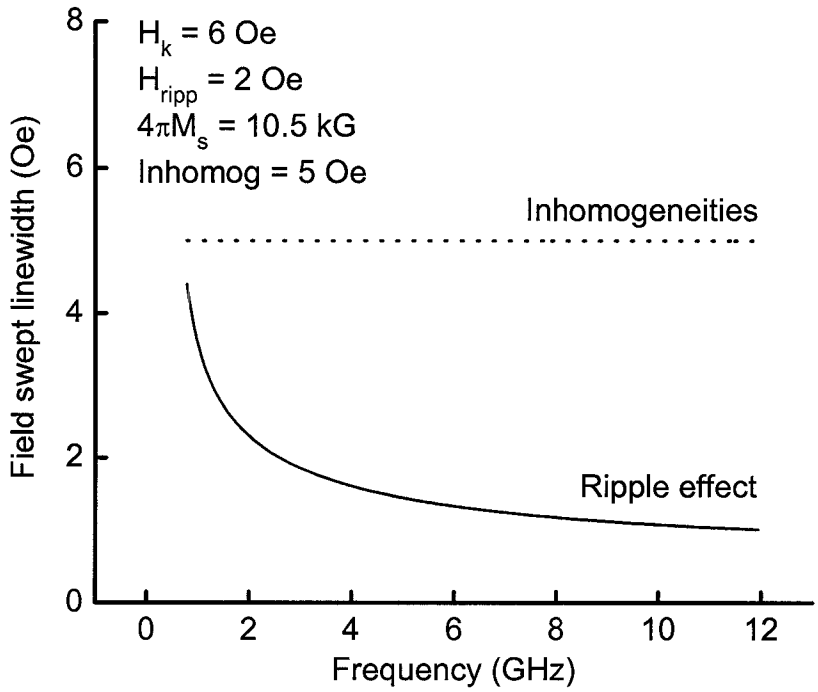

FIG. 2.10. Comparisons of the in plane field swept linewidth contribution for different linebroadening models as indicated. The dashed line is due to the inhomogeneity model, the solid line is due to the ripple field effect.

and Bloembergen, which bear their names, have been summarized with a view to focus on the frequency dependence of the calculated FMR linewidth. A modified form of Bloch-Bloembergen model, proposed by Codrington, Olds and Torey and with a constraint of magnetization conservation, has also been briefly described. Several physical mechanisms of FMR relaxation have also been described. Magnon – electron scattering, two magnon scattering in bulk materials and thin films, line broadening due to inhomogeneities and ripple effect have been briefly described and the frequency dependences of the field and frequency linewidths due to these mechanisms have been compared.

2.7 REFERENCES

(Dobin and Vittoria 2004) A. Dobin and C. Vittoria Phys. Rev. Lett. **92**, 257204 (2004).

(Arias and Mills 1999) R. Arias and D. Mills Phys. Rev. B **60**(10), 7395-7409 (1999).

(Bertaud and Pascard 1965) A. J. Bertaud and H. Pascard J. Appl Phys **36**, 970 (1965).

(Bloch 1930) F. Bloch Z. Physik **61**, 206 (1930).

(Bloembergen and Wang 1953) N. Bloembergen and S. Wang Phys. Rev. **93**, 72 (1953).

(Celinski and Heinrich 1991) Z. Celinski and B. Heinrich J. Appl. Phys. **70**, 5935 (1991).

(Clogston *et al.*1956) A. M. Clogston, H. Suhl, L. R. Walker and P. W. Anderson J. Phys. Chem. Solids **1**, 129 (1956).

(Codrington *et al.*1954) R. S. Codrington, J. D. Olds and H. C. Torrey Phys. Rev. **95**, 607 (1954).

(Dobin and Vittoria 2004) A. Dobin and C. Vittoria Phys. Rev. Lett. 92: 257204 (2004).

(Gilbert 1955) Army Research Foundation Report (1955).

(Gilbert 2004) T. Gilbert IEEE Trans. Magn. **40**, 3443 (2004).

(Griffiths 1946) J. H. E. Griffiths Nature **158,** 670 (1946)

(Harte 1965) K. J. Harte J. Appl Phys **36,** 960 (1965).

(Harte 1968) K. J. Harte J. Appl Phys **39,** 1503 (1968).

(Heinrich 2003) B. Heinrich, *Spin Relaxation in Magnetic Metallic Layers and Multilayers,* Springer Verlag (2003).

(Heinrich *et al.* 2002) B. Heinrich, R. Urban and G. Waltersdorf IEEE Trans. Magn. **30,** 2496 (2002).

(Heinrich *et al.*1985) B. Heinrich, J. F. Cochran and Hasegawa J. Appl Phys **57**, 3690 (1985).

(Herring Kittel 1951) C. Herring and C. Kittel Phys. Rev. **81**, 869 (1951).

(Hoffman 1968) H. Hoffman IEEE Trans. Magn. Mag-**4**, 32 (1968).

(Hurben and Patton 1998) M. Hurben and C. Patton J. Appl. Phys **83**(8), 4344-4365 (1998).

(Husserl) E. Husserl. http://www.husserlpage.com/

(Kalarickal *et al.* 2006) S. S. Kalarickal, P. Krivosik, M. Wu, C. E. Patton, M. L. Schneider, P. Kabos, T. J. Silva and J. P. Nibarger J. Appl Phys **99** 093909 (2006).

(Kalinikos and Slavin 1986) B. A. Kalinikos, and A. N. Slavin. J. Phys. C: Solid State Phys. **19** 7013 (1986).

(Kambersky 1976) V. Kambersky Czech. J. Phys. B **26**, 1366 (1976).

(Kambersky and Patton 1975) V. Kambersky and C. E. Patton Phys. Rev. B **11**, 2668 (1975).

(Kos *et al.* 2002) A. B. Kos, T. J. Silva and P. Kabos Rev. Sci. Instr **73**, 3563 (2002).

(Krivosik and Patton 2006) P. Krivosik and C. E. Patton J. Appl Phys: (to be submitted) (2006).

(Krivosik *et al.* 2004) P. Krivosik, S. Kalarickal, N. Mo and C. E. Patton. "*Two-magnon scattering processes in magnetic thin films - a simple and mathematically tractable model.*" The 49th MMM Conference, Nov. 7-11, Book of Abstracts, Jacksonville, Florida (2004).

(Kuanr *et al.* 2005) B. Kuanr, R. Camley and Z. Celinski Appl. Phys. Lett. **87**, 012502 (2005).

(Landau and Lifshitz 1935) L. D. Landau and E. M. Lifshitz Physik. Z. Sowjetunion **8**, 153 (1935).

(Lax and Button 1962) Lax and Button, *Microwave ferrites and ferrimagnetics.* New York, (McGraw Hill Book Company, 1962)

(LeCraw, *et al.* 1958) R. C. LeCraw, E. G. Spencer and C. S. Porter Phys. Rev. **110**, 1131 (1958).

(McMichael and Krivosik 2004) R. McMichael and P. Krivosik IEEE Trans. Magn. **40,** 2 (2004).

(McMichael *et al.*1998) R. McMichael, M. Stiles, P. Chen and W. Egelhoff J. Appl. Phys **83**(11), 7037-7039 (1998).

(Osborn 1945) J. A. Osborn, Phys. Rev. **67**, 351, (1945).

(Patton 1968) C. E. Patton, J. Appl. Phys **39**, 3060 (1968).

(Patton 1975) C. E. Patton, *Magnetic Oxides*. D. J. Craik, Wiley, London: 575-645 (1975).

(Patton *et al.*, 1975) Patton, C. E., Frait, Z. and Wilts, C. H., J. Appl. Phys **46**(11), 5002-5003.(1975)

(Rantschler and Alexander 2003) J. Rantschler and C. Alexander J. Appl. Phys **93**(10), 6665-6667 (2003).

(Schloemann 1958) E. Schloemann, J. Phys. Chem. Solids **6**, 242 (1958).

(Seiden and Sparks 1965) P. E. Seiden and M. Sparks Phys. Rev. **137**, A1278 (1965).

(Silva *et al.*1999) T. J. Silva, C. S. Lee, T. M. Crawford and C. T. Rogers J. Appl Phys **85,** 7849 (1999).

(Sparks 1964) M. Sparks, *Ferromagnetic Relaxation Theory*, (McGraw-Hill, New York, 1964)

(Sparks 1970) M. Sparks Phys. Rev. B **60**, 7395 (1970).

(Sparks *et al.*1961) M. Sparks, R. Loudon and C. Kittel Phys. Rev. **122,** 791 (1961).

(Vonsovskii 1961) Vonsovskii, Chap V. *Ferromagnetic resonanc*e. E. A. Turov. Moscow, GIMFL (1961).

(Wangsness 1955) R. K. Wangsness Phys. Rev. **98**, 927 (1955).

(Wolf 1961) P. Wolf, J. Appl Phys **32,** 95S (1961).

EXPERIMENTAL METHODS AND DATA ANALYSIS

Outline:

3.1: Introduction

3.2: Ferromagnetic resonance linewidth measurement techniques

3.2.1 Strip line ferromagnetic resonance spectrometer

3.2.2 Shorted waveguide ferromagnetic resonance spectrometer

3.3: Other ferromagnetic resonance linewidth measurement techniques

3.3.1 Vector network analyzer ferromagnetic resonance spectrometer

3.3.2 Pulsed inductive microwave magnetometer

3.4: Summary

3.5: References

3.1 INTRODUCTION

Three categories of techniques have been developed for the measurement of the ferromagnetic resonance (FMR) and the magnetodynamic damping parameters in ferromagnetic materials in the 1-40 GHz range of frequencies. The first category FMR linewidth determination involves the measurement of microwave power

absorbed by a ferromagnetic sample as a function of the static external magnetic field at a fixed microwave frequency. The resulting magnetic loss parameter obtained is the field swept linewidth, which is the most experimentally accessible parameter, which characterizes a given sample. This broad category of FMR measurement methods include the stripline (SL) based FMR technique developed in the 1960s, (Patton, 1968) the standard shorted waveguide (Green and Kohane, 1964) (Bady, 1967) and the microwave cavity (Cadieu *et al.*, 1997) FMR measurement techniques. The second category of FMR linewidth determination techniques involves the measurement of the microwave power absorbed by the sample as a function of the frequency of the applied external microwave field at a fixed static magnetic field. The resulting loss parameter is the frequency swept linewidth. This category includes the utilization of the vector network analyzer (VNA) instrumentation, with swept microwave frequency at fixed field, and conversion of the basic $S-$parameters so obtained, into FMR absorption curves and extracted linewidths (Barry, 1986) (Kalarickal *et al.*, 2006). The third category involves the use of pulsed inductive microwave magnetometry (PIMM) (Kos *et al.*, 2002) (Silva *et al.*, 1999). This last technique significantly extends early work on the inductive detection of magnetization switching (Wolf, 1961) through the use of modern, fast rise time drive electronics, coplanar waveguides for simultaneous drive and detection, and digital signal processing. The Fourier transform of the PIMM time domain response yields the FMR absorption profile in frequency and the corresponding linewidths.

Section 3.2 describes the field swept FMR measurement techniques, which include the stripline ferromagnetic resonance spectrometer method and the shorted waveguide technique. Section 3.3 describes a couple of other FMR measurement methods like the VNA ferromagnetic resonance spectrometer method and the pulsed inductive magnetometer method. Section 3.4 summarizes this chapter.

3.2 FIELD SWEPT LINEWIDTH MEASUREMENT TECHNIQUES

In the field swept FMR spectrometer technique, the FMR signal is detected either of two ways. One is the detection of power *transmitted* through the system and the other is the detection of the power *reflected* from the sample. This section describes the field swept linewidth measurement techniques utilized in the studies for this dissertation. Of the methods described here, the strip line (SL) based technique operates in the transmission mode and the shorted waveguide technique operates in the reflection mode. In either case, one varies the static magnetic field at a fixed microwave frequency, obtains an FMR absorption profile, and determines the half power field swept linewidth ΔH as the full width at half maximum (FWHM) of the response.

3.2.1 THE STRIP LINE FERROMAGNETIC RESONANCE SPECTROMETER SYSTEM

One of the techniques used for the measurement of the magnetodynamic damping parameters in metallic ferromagnetic thin films in the 1-10 GHz range of frequencies is a strip line FMR technique developed in the 1960s (Patton, 1968). The strip line ferromagnetic resonance technique allows the user the flexibility to operate in a wide band of frequencies through the use of a non-resonant strip transmission line. This avoids the usual restricted bandwidths that result from conventional shorted waveguide or cavity methods. The broad band strip line FMR spectrometer used for all the measurements in this dissertation follows the basic format given by Patton (Patton, 1968). Figure 3.1 shows a schematic of the strip transmission line used to excite the magnetic sample. The structure consists of a 1 cm wide center strip transmission line with a double ground plane. A stripline can be thought of as a flattened coaxial cable with a center conductor enclosed by an outside conductor and uniformly filled with a dielectric (Pozar, 1990). The dielectric filler used was Rexolite® with a thickness and dielectric constant chosen to ensure a 50 Ω

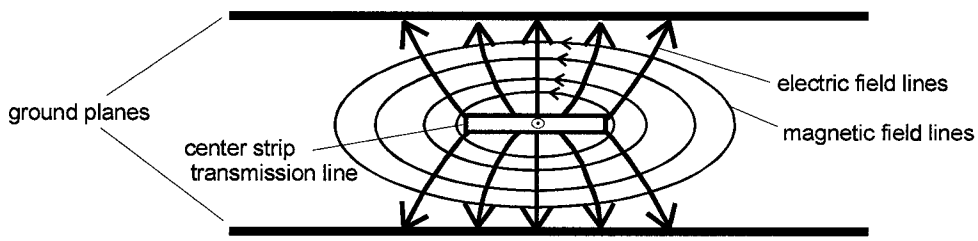

FIG. 3.1. Details of strip transmission line (side view).

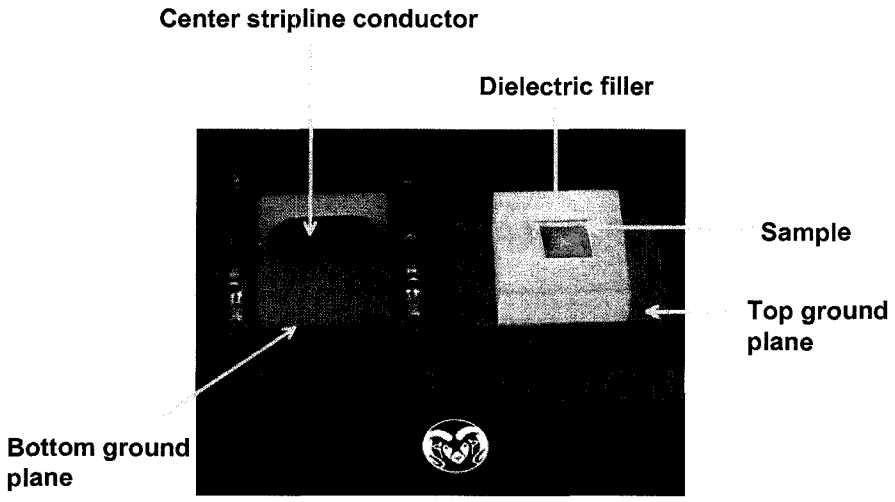

FIG. 3.2. Details of strip transmission line.

impedance matching with the cable lines. The electric and magnetic field lines in the structure are shown. The sample was mounted flush with one ground plane of the strip line in the sample recess, to ensure a reasonable homogeneity in the microwave magnetic field over the sample area. Figure 3.2 shows a photograph of the strip line device with a sphere sample mounted in the sample recess as shown. Figure 3.3 shows the transmission power vs. frequency for the strip line device measured using a vector network analyzer. The device shows very little loss for frequencies below 6.5 GHz, and hence has wide operating bandwidth of 0.6 – 6.5 GHz.

Figure 3.4 shows a schematic of the FMR spectrometer system. The spectrometer consists of a Hewlett Packard 8340B synthesized sweeper used as a continuous wave (cw) microwave input signal source, the double ground plane strip transmission line for sample excitation, coaxial isolators for voltage standing wave ratio (VSWR) reduction, and a Schottky diode for detection. A Stanford Research Systems SR830

DSP Lock-In Amplifier is used to provide field modulation and lock in detection to extract the derivative of the absorbed power vs. field profile. An ESI electromagnet is used to provide the applied static field. LABVIEW® software is used to control the microwave electronics and the static field sweep, and also to record the microwave and static field parameters used in the experiment. The inset in Fig. 3.1 shows the sample and the field geometry for an in plane magnetized thin film. The microwave input power was always kept below 1 mW to ensure a linear response.

The static magnetic field was applied in the plane of the center strip transmission line, perpendicular to the microwave field.

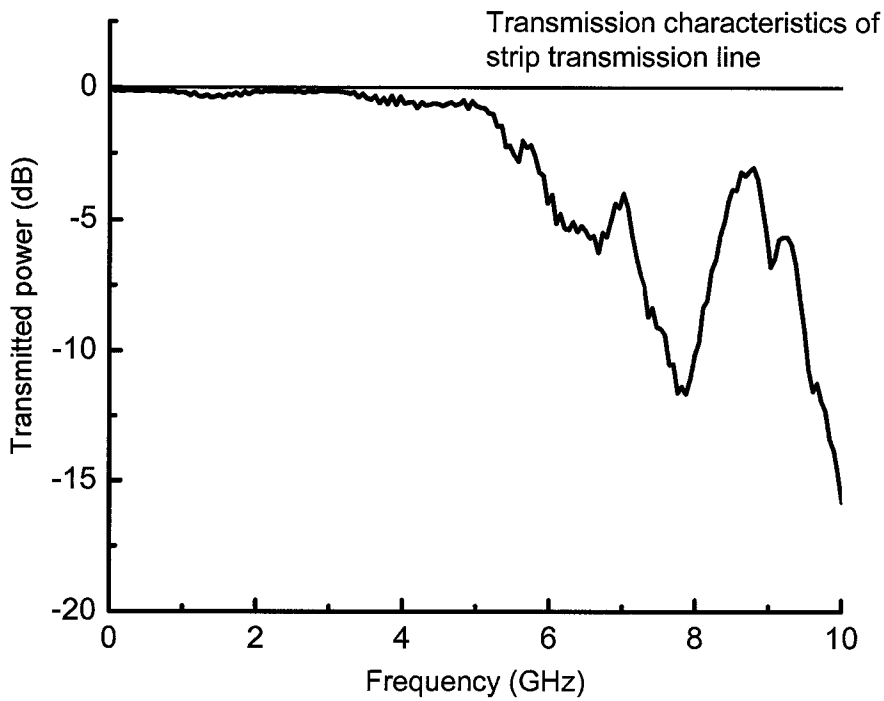

FIG. 3.3 Transmission characteristics of the strip transmission line.

An extremely useful feature of the present SL-FMR spectrometer is the capacity for FMR measurements as a function of in plane and out of plane angles for a film. A separate Rexolite® rotating disk with a sample recess is used to measure the FMR response for in plane angles, for a thin film. This disk is a part of one of the dielectric fillers and is calibrated for angles up to 5°. For out of plane FMR measurements the magnet may be rotated with a precision of 0.1°. In addition, the

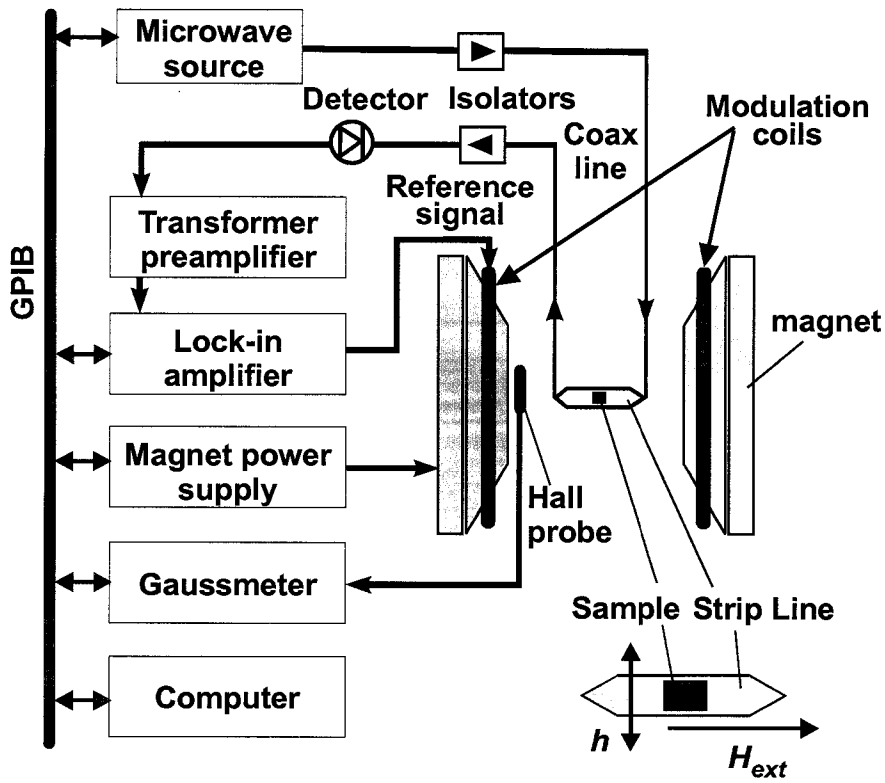

FIG. 3.4. Schematic diagram of the strip line ferromagnetic resonance spectrometer. The inset shows the field geometry and a film sample with respect to the strip transmission line. The sample is placed near one ground plane of the strip line structure and directly above the stripline. The mutually perpendicular static applied field H_{ext} and the microwave field h are both in the film plane and as indicated.

azimuthal angle can be varied with a precision of 0.025°. This is an important feature because for high magnetization films, at low GHz frequencies, the out of plane angle dependence of FMR parameters becomes extremely sensitive to the angle, especially close to the perpendicular orientation. A deviation of about 1° from the perpendicular configuration for Permalloy, for example, can give an FMR linewidth reading higher by a factor of two.

3.3.2 THE SHORTED WAVEGUIDE FERROMAGNETIC RESONANCE SPECTROMETER SYSTEM

The second spectrometer system uses a rectangular waveguide system to guide the input signal from the synthesized sweeper (Hurben, 1996) (Green, 1964). This system enables the user to operate in the 8-40 GHz frequency range. Figure 3.5 shows a schematic of the shorted waveguide system. A Hewlett Packard 8340B synthesized sweeper is used to provide a cw microwave input signal. The signal is sent directly to the X-band (8-12 GHz) waveguide system or to an HP 8349B microwave amplifier and then to a Ka-band (26-40 GHz) waveguide system. The waveguide system uses isolators to protect the microwave source and a directional coupler to separate the incident and the reflected signals. A Stanford Research Systems SR830 DSP lock-in amplifier is used to provide field modulation and lock in detection to extract the derivative of the absorbed power vs. field profile. A Varian electromagnet is used to provide the applied static field for the X-band

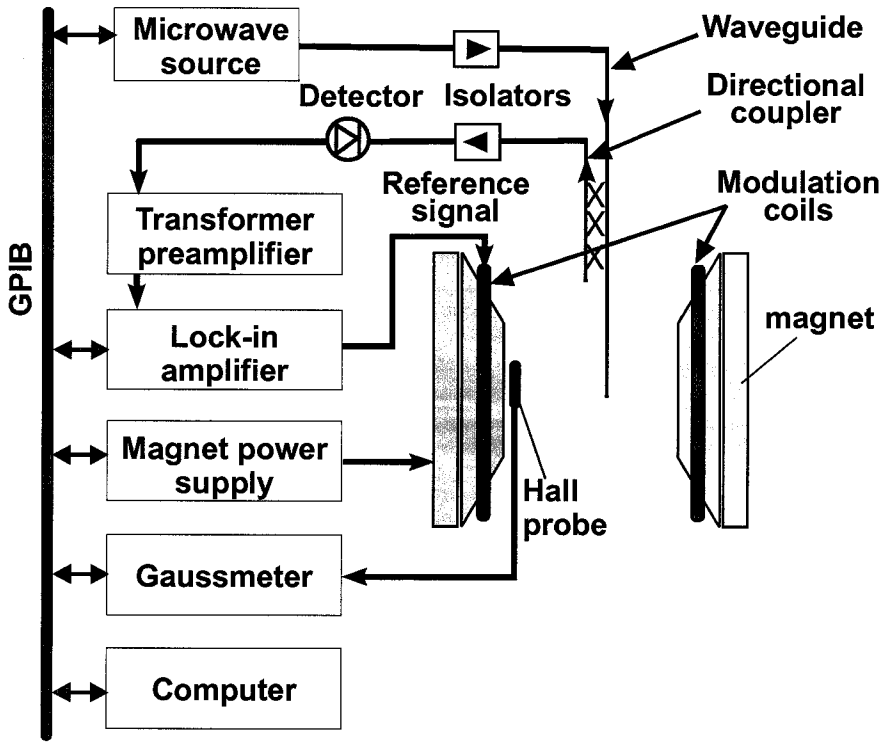

FIG. 3.5. Schematic diagram of the shorted waveguide ferromagnetic resonance spectrometer.

spectrometer. An ESI electromagnet is used to provide the applied static field for the Ka band spectrometer. LABVIEW® software is used to control the microwave electronics and the static field sweep, and also to record the microwave and static field parameters used in the experiment. The sample is mounted at the end of the shorted waveguide, which ensured a microwave field perpendicular to the static field for all the frequencies.

The experimental FMR absorption derivative vs. field profiles obtained for various samples were generally undistorted and symmetric. Direct numerical integration of the data gave near Lorentzian profiles. The full width at half maximum of a Lorentzian fit to the integrated data was then used as a measure of the half power

FMR linewidth of the samples. The FMR linewidth was also measured as the difference between the inflexion points of the derivative curve and is known as the peak to peak value. This value is related to the linewidth of the corresponding Lorentzian absorption curve by a factor of $\sqrt{3}$.

Figure 3.6 shows representative data for a sample of 50 nm Permalloy thin film on a glass substrate. Graph (a) shows a typical measured absorption derivative vs. field profile for 3 GHz microwave excitation. The profile is symmetric and clean. The solid circles in graph (b) show the normalized integrated data and the solid curve

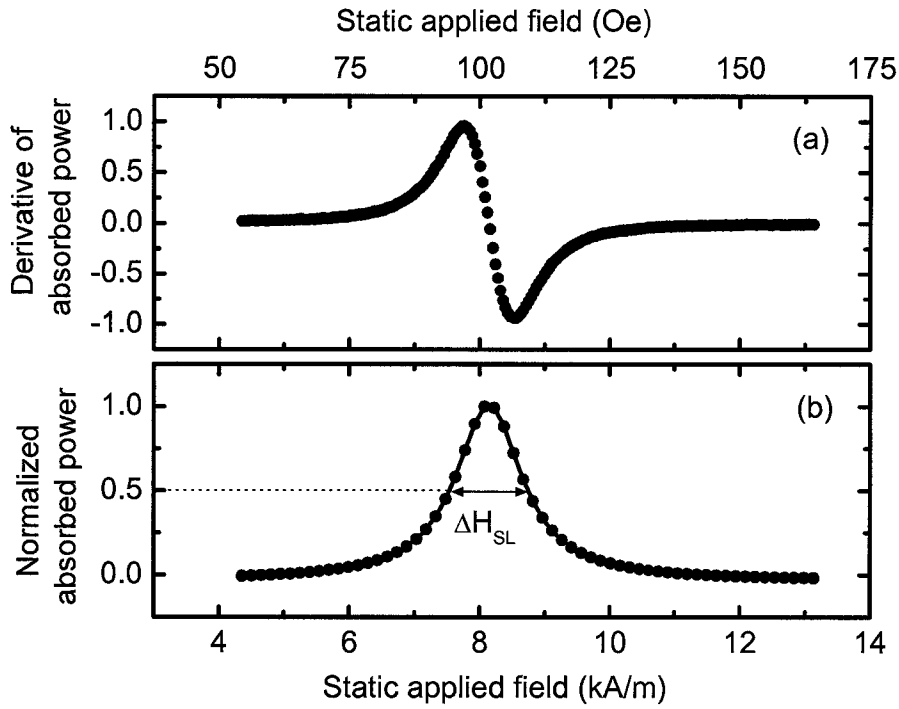

FIG. 3.6. Representative ferromagnetic resonance data. Graph (a) shows ferromagnetic resonance absorption derivative versus static applied field data for a 50 nm inplane magnetized Permalloy film at 3 GHz. Graph (b) shows the normalized integrated response from (a) as a function of field. The solid curve in (b) is a Lorentzian fit to the data.

shows the Lorentzian fit. A resonance field H_{res} of 101 ± 0.5 Oe and a half power linewidth ΔH_{SL} value of 8.3 ± 1 Oe were obtained from these data.

3.3 OTHER FERROMAGNETIC RESONANCE LINEWIDTH MEASUREMENT TECHNIQUES

Besides the field swept linewidth measurement methods, FMR linewidth for Permalloy was also measured using two other techniques, at the National Institute of Standards and Technology (NIST), Boulder. These methods fall in the second and third category as mentioned in Section 3.1. This section briefly outlines these two techniques.

3.3.1 THE VECTOR NETWORK ANALYZER FERROMAGNETIC RESONANCE SPECTROMETER SYSTEM

The vector network analyzer (VNA) FMR technique also allows for operation over a wide frequency band and yields FMR parameters from standard microwave S – parameter measurements vs. frequency and field. Figure 3.4 shows a diagram of the system. The microwave drive in this case is provided by a coplanar waveguide (CPW) excitation structure, with the thin film sample positioned across the center conductor as indicated. The static magnetic field is provided by a set of Helmholtz coils. The signal analysis is done with a standard vector network analyzer.

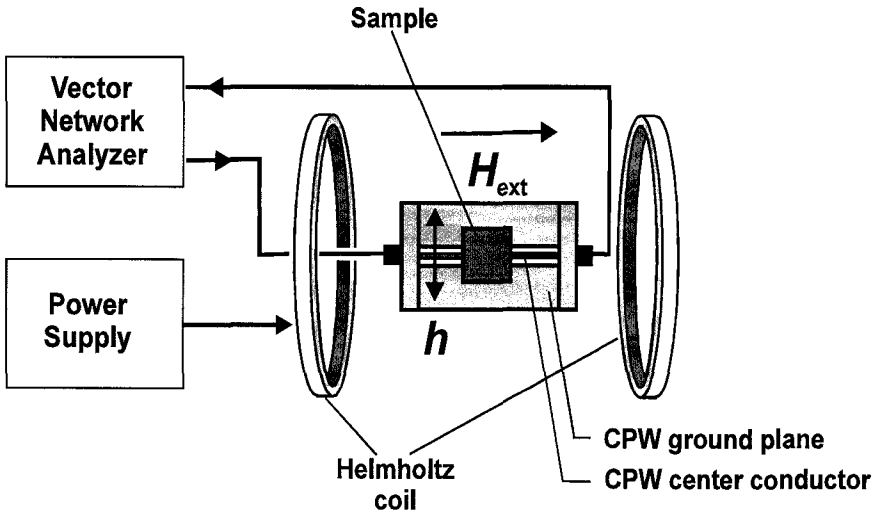

FIG. 3.7. Schematic diagram of the vector network analyzer ferromagnetic resonance spectrometer. The sample is placed on the coplanar waveguide (CPW) structure as indicated. The mutually perpendicular static applied field $\boldsymbol{H}_{ext}$ and the microwave field $\boldsymbol{h}$ are in the plane of the film and as indicated.

The coplanar waveguide had a 100 μm wide center strip. The static field was applied in the plane of the film and perpendicular to the microwave field. The set-up was then used to obtain the standard microwave $S-$parameters as a function of frequency at fixed field for the CPW line with the sample in place. Data were collected for a range of fixed static fields from 20-106 Oe. A typical frequency sweep extended from 400 MHz to 4.4 GHz. For sweeps at fields below 46.7 Oe, the reference field was set at 106 Oe, and for fields above this mid-value, a reference field of 9.4 Oe was used.

The data were analyzed on the basis of a transmission line model developed by (Barry, 1986) under the assumption that the dominant CPW mode was the TEM mode. If the effect of reflections is neglected, the Barry analysis gives an uncalibrated effective microwave permeability of the form

$$U(f) = \pm \frac{i \ln\left[S_{21\text{-H}}(f)/S_{21\text{-ref}}(f)\right]}{\ln\left[S_{21\text{-ref}}(f)\right]}, \tag{3.1}$$

where the sign is chosen to make $\mathrm{Im}[U(f)]$ negative in the vicinity of the FMR peak. The f denotes the common set of frequency points for the two data runs, $S_{21\text{-H}}(f)$ denotes the corresponding set of S_{21} parameters at the FMR field of interest, and $S_{21\text{-ref}}(f)$ is the set of reference S_{21} parameters at the reference field. Under ideal circumstances, $-\mathrm{Im}[U(f)]$ vs. f would correspond to the FMR loss profile and $\mathrm{Re}[U(f)]$ would show the $U(f)$ dispersion.

Figure 3.8 shows representative 1 - 3 GHz results for a 50 nm Permalloy film at an external field $H_{\mathrm{ext}} = 40.5$ Oe, with the reference data at $H_{\mathrm{ext}} = 106$ Oe. The film was oriented with the uniaxial anisotropy easy axis parallel to the CPW line. The open and solid circles show the data for $-\mathrm{Im}[U(f)]$ and $\mathrm{Re}[U(f)]$, respectively, with all data normalized to give a maximum $-\mathrm{Im}[U(f)]$ value of unity at the FMR peak. The solid curves show fits that will be discussed shortly. As far as the data are concerned, the main point of note is that the responses shown for $-\mathrm{Im}[U(f)]$ and $\mathrm{Re}[U(f)]$ do not correspond strictly to the loss and dispersion profiles expected from FMR theory (Patton, 1975). The $-\mathrm{Im}[U(f)]$ response is asymmetric and actually drops below zero at low frequency. The $\mathrm{Re}[U(f)]$ response shows a significant departure from a dispersive response above about 2.3 GHz.

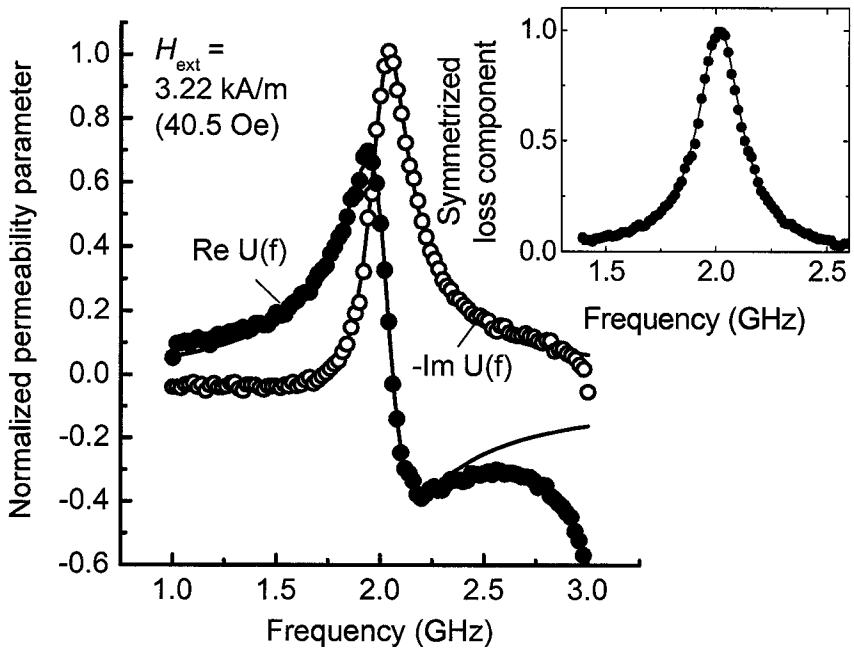

FIG. 3.8. Representative vector network analyzer ferromagnetic resonance (VNA-FMR) data that shows the normalized permeability parameter U vs. frequency f for a 50 nm Permalloy film at an applied static field $H_{ext} = 40.5$ Oe. The solid circles show the $\mathrm{Re}[U(f)]$ and the open circles show $-\mathrm{Im}[U(f)]$ values extracted from the experimental $S-$ parameters. The solid curves show fits to the data based on the analysis given in the text. The inset shows the data in a normalized loss component format from equation (3.7), with conversion based on the same fit parameters used to obtain the solid curves in the main figure plot. The solid curve in the inset shows the theoretical loss profile.

These distortions are attributed to two effects, (1) the neglect of reflections in the simplified analysis that gives Eq. (3.1) and (3.2) the proximity of the reference field value to the FMR field points. The result is a combination of offsets and distortions due to the FMR response embedded in the reference data the as well as a mixing of the real and imaginary components of the actual $\chi(f)$ susceptibility in the measurements. Linewidths were obtained through an empirical scheme in which the data were fitted to a modified susceptibility response function of the form

$\chi_0 + \chi(f)e^{i\phi}$, where χ_0 is a complex offset parameter and ϕ is a phase shift. This procedure was applied for each of the measurement fields to obtain frequency linewidth Δf_{VNA} values vs. the FMR frequency. Details are given below.

The complex susceptibility response at a frequency f for a uniaxial thin film magnetized to saturation along the easy axis by a static external field H_{ext} may be written as

$$\chi(f) = \frac{1}{\mu_0} \frac{M_S\left(H_{\mathrm{ext}} + H_k + M_S\right)}{\left[f_{\mathrm{res}}^2 - f\left(f + i\Delta f_{\mathrm{VNA}}\right)\right]\left(\frac{2\pi}{|\gamma|\mu_0}\right)^2}. \tag{3.2}$$

In the above, M_S is the saturation magnetization, H_k is the uniaxial anisotropy field parameter, f_{res} is the resonance frequency, γ denotes the electron gyromagnetic ratio, and Δf_{VNA} is the frequency swept linewidth. The full fitting function to the data was written as

$$U_{\mathrm{fit}}(f) = C\left[1 + \chi_0 + \chi(f)e^{i\phi}\right], \tag{3.3}$$

where C is a real scaling parameter, χ_0 is a complex offset parameter, and ϕ is a phase shift adjustment. The extracted data were fit simultaneously to both real and imaginary parts of the function $U_{\mathrm{fit}}(f)$ to obtain the f_{res} and Δf_{VNA} values. The form in Eq. (3.3) is based on the fact that $U(f)$ is related to the actual complex microwave permeability μ and that μ, in turn is equal to $\mu_0[1+\chi(f)]$.

For the data shown in Fig. 3.8, the fitting procedure gives f_{res} and Δf values of 2.0 GHz and 236 ± 12 MHz, respectively. The fitted values for $\mathrm{Re}\,\chi_0$, $\mathrm{Im}\,\chi_0$, and ϕ for these particular data were –157, –34, and 24 degrees, respectively. As a demonstration that this procedure actually corresponds to a Lorentzian loss profile, the Fig. 3.8 inset shows the same data in a normalized loss format corresponding to $-\mathrm{Im}[\chi(f)]$, along with the theoretical response shown by the solid curve. The above procedure gave satisfactory fits for the entire ensemble of VNA data. All FMR frequency fits were accurate to better than 1 MHz and the linewidth fits were accurate to five percent or so. For a given fit, the values for χ_0 were in the range expected from the tail of the reference field FMR $\chi(f)$ response. The fitted ϕ values were in the 21° - 25° range.

3.3.2 THE PULSED INDUCTIVE MICROWAVE MAGNETOMETER SYSTEM

The pulsed inductive microwave magnetometer technique allows the user to obtain the loss parameters in the ferromagnetic material from the free induction decay of the dynamic magnetization in response to a pulsed magnetic field rather than a microwave field.(Schneider *et al.*, 2005) (Silva, 1999) Figure 3.9 shows a simplified diagram of the PIMM system. The pulsed field h is provided by a coplanar waveguide (CPW) structure, with the thin film sample positioned across the center conductor as indicated. Two sets of Helmholtz coils provide the necessary static

fields. Set A is used to produce the static field parallel to the CPW axis and perpendicular to the pulsed field for measurement. This field controls the ringing response. Set B is used to saturate the film in the transverse direction in order to obtain a reference signal without ringing. These responses are measured in the time domain with a 20 GHz sampling oscilloscope.

The data reported were obtained for a range of static measurement fields from 20 to 100 Oe. The CPW structure had a center strip width of 220 μm. The input CPW field pulses have a rise time and duration of 50 ps and 10 ns, respectively. The maximum pulse field amplitude was approximately 0.8 Oe. This combination of static and pulsed field amplitudes ensured a linear response (Nibarger *et al.*, 2003). The Permalloy film samples were placed on the top of the CPW structure with the substrate side down in order to minimize any possible impedance mismatch due to the presence of the sample. The films were oriented with the uniaxial anisotropy easy axis parallel to the CPW line. The dynamic magnetization ringing response to the initial step in the CPW field pulse was measured and used for the decay and linewidth analysis.

A given dynamic magnetization response to the initial step in the CPW pulsed field was measured and analyzed in four steps. (1) A transverse field H_B (coil set B) of 70 Oe was applied to saturate the film in the hard direction. (2) With H_B reset to zero, the desired easy direction static field H_A (coil set A) was applied and the

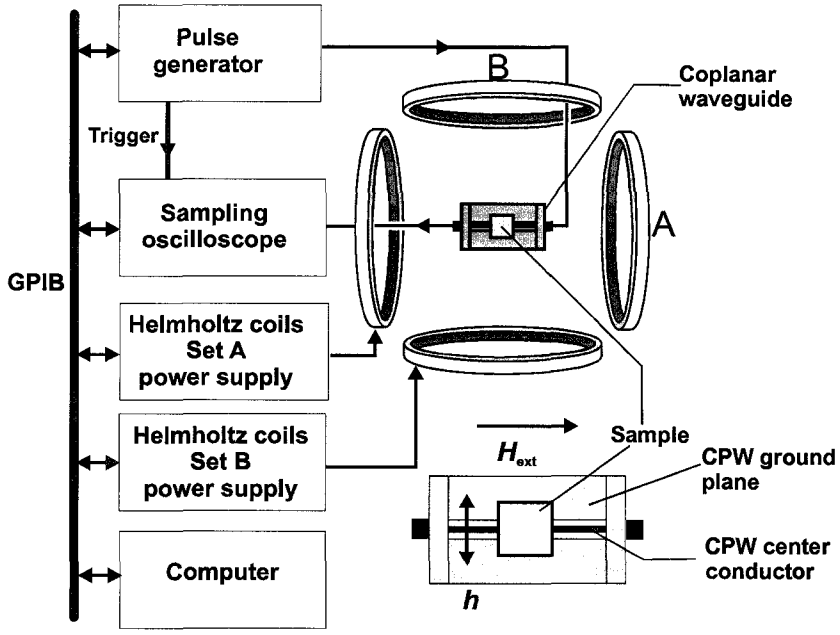

FIG. 3.9. Schematic diagram of the pulsed inductive microwave magnetometer. The sample is placed on the coplanar waveguide (CPW) structure as indicated. The inset shows the field geometry and sample with respect to the center conductor and the ground plane of the coplanar waveguide, with the mutually perpendicular static applied field $\boldsymbol{H}_{ext}$ and the microwave field $\boldsymbol{h}$ are in the plane of the film, as indicated.

output voltage vs. time profile from the CPW line, taken as $V_A(t)$, was measured for a range of times from about 0.5 ns prior to the onset of the pulse to a time 10 ns after the step. (3) With H_A reset to zero and H_B held at 70 Oe, a second output voltage vs. time profile, $V_B(t)$, was measured again to provide a reference data set. The step response was then obtained as $V_R(t) = V_A(t) - V_B(t)$. (4) A fast Fourier transform of this time domain ringing response signal was then used to extract absorption and dispersion vs. frequency profiles. Fits of these FFT data to a standard damped oscillator frequency response then yielded the FMR frequency and FWHM frequency linewidth at each measurement field.

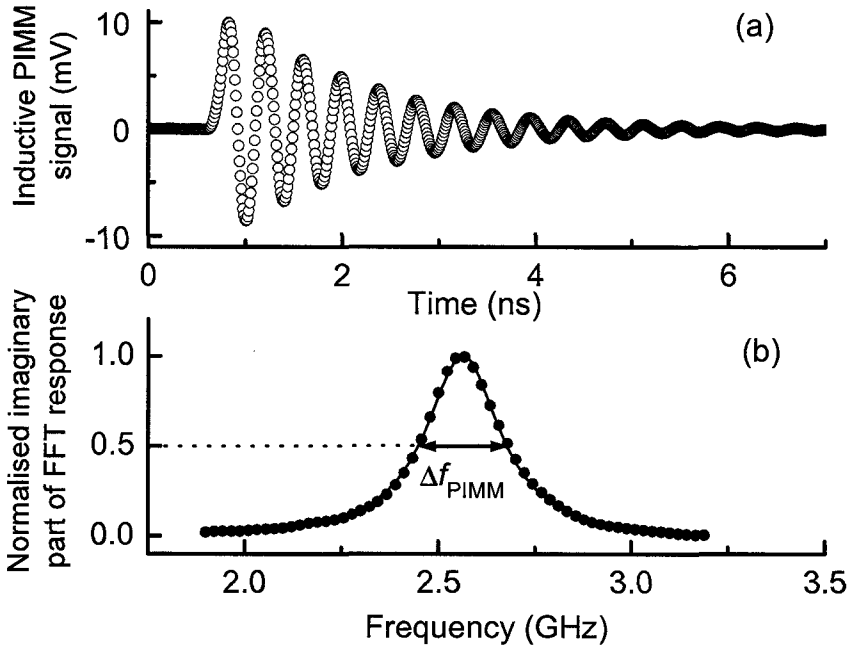

FIG. 3.10. Representative data from the pulsed inductive microwave magnetometer (PIMM) system. Graph (a) shows the inductive signal for a 50 nm Permalloy film with a static applied field of 66 Oe. Graph (b) shows the imaginary part of the fast Fourier transform (FFT) of the signal in (a). The solid curve in (b) is a Lorentzian fit to the data.

Figure 3.10 shows representative data for a 50 nm Permalloy film. These data are for a measurement field of 66 Oe. Figure 3.10(a) shows the free induction decay $V_R(t)$ response discussed above. In Figure 3.10(b), the loss component of the FFT response and a Lorentzian fit to those data are shown by the solid circles and the solid curve, respectively. The corresponding resonance frequency f_{res} is 2.53 ± 0.05 GHz and the fitted FWHM frequency linewidth Δf_{PIMM} for the profile in (b) is 236 ± 11 MHz.

3.4 SUMMARY

This chapter gives detailed description of the different techniques used in this dissertation work to measure FMR losses in ferromagnetic materials. The strip line spectrometer has been described, which eliminates the need for the use of several cumbersome and large waveguides in the L band (0.8 - 2GHz), the S band (2 - 3 GHz) and the C band (3 - 6 GHz). This spectrometer operates in the transmission mode. The shorted waveguide technique has been described which is has been set up in the magnetic laboratory at Colorado State University (CSU) for use in the X-band (8-12 GHz) and higher frequency ranges. This spectrometer operates in the reflection mode. These give microwave losses in terms of field swept linewidth.

Besides these methods, the vector network analyser and the pulsed inductive microwave magnetometer techniques have also been described. In use at the National Institute of Standards Technology at Boulder, CO, these techniques give microwave losses in terms of the frequency swept linewidth.

All results on the different materials and sample geometries presented in this dissertation have been measured using the field swept linewidth measurement techniques. Since the VNA-FMR and the PIMM techniques are fairly new and are gaining popularity, it was important to compare the microwave losses obtained using these frequency swept linewidth measurement techniques and the traditional field swept linewidth measurement techniques used at CSU. This was done using Permalloy thin films and the results are discussed in Chapter 4.

3.5 REFERENCES

(Bady 1967) I. Bady IEEE Trans. Magn. **3,** 521 (1967).

(Barry 1986) W. Barry IEEE trans. Microwave theory and techniques **MTT-34,** 80 (1986).

(Cadieu et al. 1997) F. J. Cadieu, R. Rani, W. Mendoza, B. Peng, S. A. Shaheen, M. J. Hurben and C. E. Patton J. Appl. Phys **81,** 4801 (1997).

(Green and Kohane 1964) J. J. Green and T. Kohane SCP Solid State Technol. **7,** 46 (1964).

(Hurben 1996) M. J. Hurben, *Two magnon scattering and relaxation in ferrite thin films*, Colorado State University. Ph. D. (1996).

(Kalarickal et al. 2006) S. S. Kalarickal, P. Krivošik, M. Wu, C. E. Patton, M. L. Schneider, P. Kabos, T. J. Silva and J. P. Nibarger J. Appl Phys **99**(9), In Press (2006).

(Kos et al. 2002) A. B. Kos, T. J. Silva and P. Kabos Rev. Sci. Instr **73**, 3563 (2002).

(Nibarger et al.2003) J. Nibarger, R. Lopusnik and T. Silva Appl. Phys. Lett. **82**(13), 2112-2114 (2003).

(Patton 1968) C. E. Patton, J. Appl. Phys **39**, 3060 (1968).

(Patton 1975) C. E. Patton, *Magnetic Oxides*. D. J. Craik, Wiley, London: 575-645 (1975).

(Pozar 1990) D. M. Pozar, *Microwave engineering*, (Addison-Wesley, 1990)

(Schneider et al. 2005) M. L. Schneider, T. Gerrits, A. B. Kos and T. J. Silva Appl. Phys. Lett. **87**, 072509 (2005).

(Silva et al.1999) T. J. Silva, C. S. Lee, T. M. Crawford and C. T. Rogers J. Appl Phys **85**, 7849 (1999).

(Wolf 1961) P. Wolf J. Appl Phys **32**, 95S (1961).

EXPERIMENTAL RESULTS I – FMR LINEWIDTH IN METAL FILMS

Outline:

4.1: Ferromagnetic resonance in Permalloy films

4.1.1: Introduction and background

4.1.2: Material details

4.1.3: FMR linewidth for in-plane magnetized films

4.1.4: Comparison of FMR linewidth obtained from different techniques

4.1.5: FMR linewidth for obliquely magnetized thin films

4.1.6: FMR linewidth for perpendicularly magnetized films

4.1.7: Summary and conclusions

4.2: Ferromagnetic resonance in nitrogenated iron-titanium films

4.2.1: Introduction and background

4.2.2: Material details, resistivity and static magnetization results

4.2.3: Ferromagnetic resonance response

4.2.4: Summary and conclusions

4.3: References

4.1 FERROMAGNETIC RESONANCE IN PERMALLOY FILMS

4.1.1 INTRODUCTION AND BACKGROUND

The study of ferromagnetic metals has recently found renewed motivation following the application of these materials in the magnetic recording industry. Applications which employ fast magnetization reversal processes have spurred an increase in the interest to acquire a thorough understanding of the spin dynamics and magnetic relaxation processes in the nanosecond regime (Plummer and Weller 2001), (Hillebrands and Ounadjela 2001) .

As was already discussed in Chapter 2, magnetic relaxation is not an intrinsic property of material alone; it depends upon several factors such as the sample shape, its quality, etc. It is often described in terms of extrinsic and intrinsic factors. Magnetic damping in metals is believed to be due to spin-orbit interaction between localized and conduction electrons accompanied by scattering of electrons to phonons. At finite temperatures the scattering of spin wave excitations (magnons) with conduction electrons and phonons is an integral part of the system. These are intrinsic processes. The presence of structural and compositional defects also lead to losses, and these are called extrinsic contributions.

The origin of intrinsic damping in metallic ferromagnets is often not understood. The applicability of different phenomenological relaxation models in the description of intrinsic damping has been a long-standing question. In this work, this issue has

been tackled with the study of FMR linewidth as a function of frequency and of the magnetization angle to the thin film sample normal. In what follows, the external magnetic field configuration when the external static field and the microwave field are both in the plane of the sample is referred to as the parallel configuration. The perpendicular configuration is one in which the external static field is perpendicular to the plane of the sample while the microwave field is in the plane of the sample. The Landau-Lifshitz (LL) or Gilbert (G) damping models predict a linear behaviour of the field swept linewidth ΔH as a function of frequency, both in parallel and perpendicular configurations. The magnitude of the ΔH is also expected to be identical in both the configurations. On the other hand, the Bloch Bloembergen (BB) model predicts a linear behaviour of ΔH as a function of frequency in the parallel configuration while it predicts a constant ΔH in the perpendicular configuration.

Field linewidth measurements by Quach *et al.* (Quach *et al.* 1976) on 10 μm thick (100) Ni-Co platelets as a function of angle at frequencies of 9.5, 24.8 ad 35.5 GHz, could be fit by an LL model. Measurements reported by Anderson (Anderson *et al.* 1971) on single crystals of Ni(001) and Ni(110) at a frequency of 22 GHz as a function of angle could also be fit by a LL model with a constant parameter α. Studies by Frait and Fraitova (Frait and Fraitova 1980) on Fe whiskers over a range of frequencies of 20-100 GHz also show that the intrinsic damping could be represented by an LL model. Patton et *al.* have done work on 15 to 320 nm thick evaporated NiFe films, which showed different results (Patton 1968). The field linewidth ΔH in the perpendicular configuration for a 15 nm thick NiFe film was

considerably larger than ΔH in the parallel configuration. Another observation was that the perpendicular linewidth was independent of frequency while the linewidth in the parallel configuration was linear in frequency. This result is in contradiction to the LL damping model and supports the BB model. Conversely, results on another set of NiFe evaporated thin films showed linear dependence of linewidth in both parallel and perpendicular configurations for frequencies above 10 GHz (Patton *et al.* 1975). For frequencies below 10 GHz however, it was seen that ΔH in the parallel configuration was linear while ΔH in the perpendicular configuration showed a levelling off. The work by Patton on the out of plane angle dependence of FMR linewidth also shows that the linewidth in certain films could be modelled by a constant LL damping parameter (Patton 1973).

While the characteristics of magnetic damping in ferromagnetic materials have been under intense investigation over the past few decades, several issues still remain. The work in this dissertation with regard to Permalloy film has been threefold. First, in spite of intensive metal film FMR work over many years, there has been no systematic comparison of the actual decay rates and linewidths that are obtained from the three different methods of FMR measurement described in Chapter 3. One of the purposes of this work was to measure decay rates and FMR linewidths for representative Permalloy thin films by all three techniques, analyze the data in a systematic way, and compare the results. These comparisons were made in terms of the conventional half power field swept linewidth from SL-FMR measurements, and the frequency swept linewidth that comes directly from VNA-

FMR measurements and the PIMM fast Fourier transform (FFT) analyses. The results show that all techniques and both formats provide consistent values of the damping and relaxation parameters for these films. Permalloy films with in-plane uniaxial anisotropy were chosen for the comparison measurements because of their good soft magnetic properties and nominally low linewidths.

Second, there has been little experimental work to resolve the issue of phenomenological damping models applicable to metal films. The models for describing magnetic damping have been well established for magnetic oxides. As far as ferromagnetic metals are concerned, there are models describing the scattering to electrons and due to impurities but experimentalists mostly have to select between a few phenomenological models and even this is under intense debate. A study of relaxation in metal films would include a study of FMR linewidth for in-plane, obliquely and perpendicularly magnetized films at various frequencies. Measurement of linewidth in the perpendicular orientation at the lower GHz range can get problematic. At these frequencies the alignment of the external static field with the film normal becomes quite crucial. A minor deviation of the external static field direction from the film normal would imply a much larger value of the measured perpendicular linewidth. This problem was solved with the alignment method used in the SL-FMR system, where it is possible to align to angles better than 0.1 degree. The second goal of this work was therefore to carefully measure the angle dependence of FMR linewidth, and compare the linewidth in the parallel and perpendicular configuration to establish the connection between the

phenomenological models that may be used in the analysis of the damping in Permalloy films.

Third, several types of substrates have been used for the deposition of polycrystalline Permalloy films. Glass has been the traditional material of use as substrates. Silicon substrates have been in use lately because of the ease with which magnetostriction could be measured for films deposited on Si. The choice of substrate has hence shifted changed from glass to silicon. Related influence on the FMR linewidth has not been compared. This question has also been addressed as the third goal of this work, which was to measure and compare the linewidths obtained for Permalloy films deposited on different substrates

Section 4.1.2 gives the material details of the Permalloy films used in this investigation. Section 4.1.3 compares the FMR linewidth obtained using the different techniques mentioned in Chapter 3. Section 4.1.4 gives the frequency dependence of the FMR linewidth in the parallel configuration and also comments on the linewidth obtained for Permalloy films deposited by different techniques and on different substrates. Section 4.1.5 gives the out of plane angle dependence of the FMR linewidth. Section 4.1.6 gives the frequency dependence of the FMR linewidth in the perpendicular configuration. Section 4.1.7 gives a summary of the FMR results on Permalloy films.

4.1.2 MATERIAL DETAILS

Permalloy is a ferromagnetic alloy, with a nominal composition of 80% Ni and 20% Fe. This composition of Ni and Fe gives zero magnetostriction. This alloy has been known to have the lowest microwave loss among metal films. These films are usually deposited in a static magnetic field applied in the plane of the film, which is known to enhance the uniaxial in plane anisotropy.

The Permalloy films studied in this work were prepared by DC magnetron sputtering with a nominal composition of $Ni_{80}Fe_{20}$. These films were prepared on 1 cm × 1 cm glass substrates, with a 5 nm Ta seed layer. The Ta seed layer was deposited to enhance the adhesion of the Permalloy film. The films were deposited at room temperature with the substrates mounted on a rotating fixture with permanent magnets that provided a nominal in-plane field of 25 Oe. The resulting films had square easy direction hysteresis loops, and showed coercive forces and anisotropy fields in the 2 and 5 Oe range, respectively.

The two substrates used for comparison in this study were glass and silicon substrates. The films deposited on these two substrates have been designated as SX_g and SX_{Si}. Here X stands for the thickness of the film in nm. The thicknesses of films varied from 10 nm to 150 nm.

4.1.3 FMR LINEWIDTH FOR IN-PLANE MAGNETIZED FILMS

This section provides results on the ferromagnetic resonance (FMR) linewidth as a function of frequency from 2-6 GHz for in plane magnetized Permalloy films. The

measurement technique used was the stripline ferromagnetic resonance (SL-FMR) technique, which has been described in Chapter 3. The FMR field linewidth ΔH was also measured as a function of film thickness. The linewidth increased drastically for thicknesses larger than about 100 nm, and this trend was noticed for films deposited on glass as well as Si substrates.

Figures 4.1.1 and 4.1.2 show the linewidth ΔH for different frequencies as a function of film thickness. Figure 4.1.1 shows the ΔH values for SX_g samples, as a function of thickness for the indicated frequencies between 2 and 5.5 GHz. Figure 4.1.2 shows the ΔH values for SX_{Si} samples, as a function of thickness for the indicated frequencies between 2 and 6 GHz. For the SX_g samples, the ΔH values were in the 12-35 Oe range. At any given frequency, the linewidth decreased for thicknesses less than 100 nm, above which the linewidth shows an increase. For the SX_{Si} samples, the ΔH values were in the 25- 85 Oe range. At any given frequency, the linewidth remained constant for thicknesses less than 100 nm, above which the linewidth shows an increase. This increase in ΔH for thickness larger than 100 nm is expected because eddy current effects become prominent for these thicknesses as will be elaborated later.

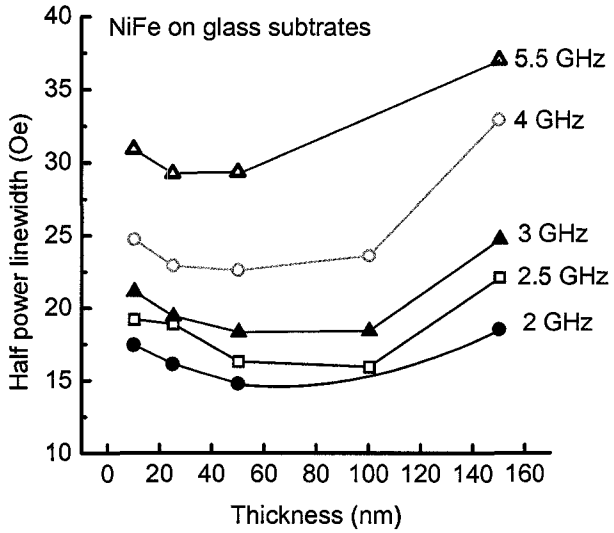

FIG. 4.1.1 In plane half power linewidth vs. thickness in Permalloy films on glass substrates

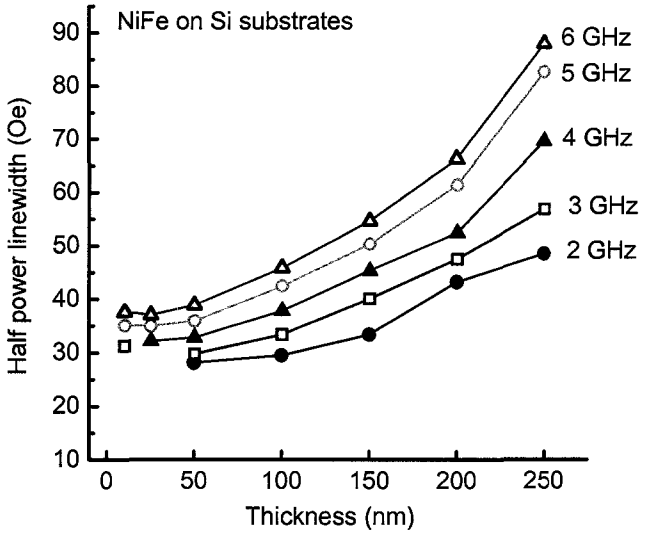

FIG. 4.1.2. In plane half power linewidth vs. thickness in Permalloy films on Si substrates at frequencies as indicated.

The FMR data obtained for the SX_g and SX_{Si} samples, shown in Fig. 4.1.1 and 4.1.2, were plotted as a function of frequency. In both cases, as is expected of metal films, the linewidth vs. frequency response was linear. The linewidth of SX_{Si} was generally larger than the linewidth of SX_g. Moreover, the slopes of the linear trends of the SX_g and SX_{Si} samples were markedly different, with the SX_g samples having a larger slope. The SX_{Si} samples also showed a larger intercept on the linewidth axis, for zero frequency, than the SX_g samples.

Figure 4.1.3 shows half power FMR linewidth vs. frequency, for a representative sample $S50_g$ in the wide frequency range of 2.25 - 12.5 GHz. The solid circles show half power linewidth data obtained with the stripline FMR technique. The open circles show the half power linewidth data obtained with a shorted waveguide technique. The dotted line is a linear fit to the data. The solid curve is a calculation using the ripple field theory in combination with the LL theory. The ripple field used for the calculation is 5 Oe, which is of the same as the uniaxial anisotropy parameter for this film. The LL damping parameter α_{LL} used was 0.006. The data obtained with the SL FMR technique are compatible with the data obtained with the shorted waveguide technique. Also the linewidth vs. frequency data is seen to be linear in the wide band of frequencies. Linear linewidth responses are often interpreted in terms of a combined inhomogeneous broadening and Landau - Lifshitz damping model.(Heinrich *et al.* 1985) (Liu *et al.* 2003) Within this framework, one would expect a field swept half power linewidth of the form

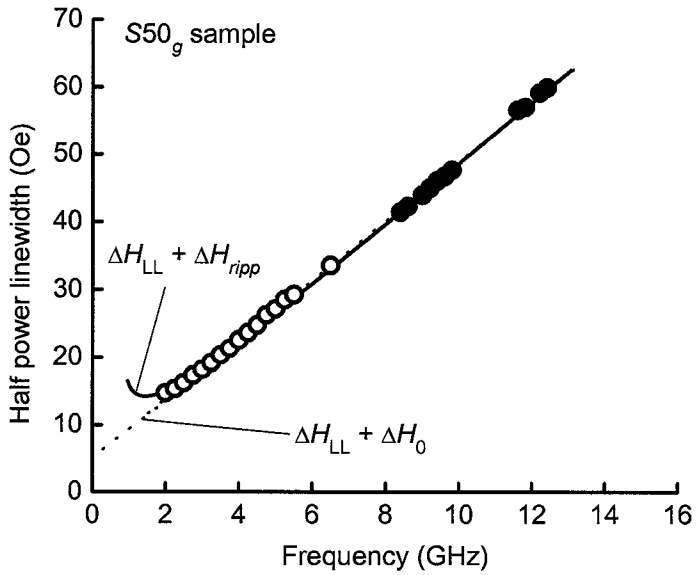

FIG.4.1.3. Half power FMR linewidth vs. frequency for $S50_g$. The dotted straight line is a linear fit to the data and the solid curve is a fit to the calculation with LL damping and ripple field effect taken into consideration

$$\Delta H = \Delta H_0 + \frac{2\alpha_{sl}\omega}{|\gamma|}, \tag{4.1.1}$$

where ΔH_0 is a measure of the inhomogeneous broadening in field that affects the FMR response. The slope $2\alpha_{sl}/|\gamma|$ may have several interpretations. First, the linear trend of the data can be related to a phenomenological Landau Lifshitz or Gilbert type of relaxation. The slope of the line may be therefore interpreted as due to the damping parameter α_{LL} or α_G. Second, it may be related to magnon-electron scattering relaxation, which has been known to give linear frequency dependence with corresponding α_{me} damping parameter. For low linewidths found here, the Landau Lifshitz and Gilbert models are equivalent for all practical purposes. Since the actual damping parameter is open to several interpretations, the parameter

obtained from the linear fit to the experimental data will be denoted as α_{sl}. The slope given above corresponds to an α_{sl} value of about 0.006, which is a typical literature damping parameter value for Permalloy. The intercept ΔH_0 is a measure of the inhomogeneous broadening in field that affects the FMR response as mentioned in Chapter 2.

The ripple effect trend in conjunction with the Landau-Lifshitz model also fits the data. The slight upturn at lower frequencies, due to pronounced effect of the ripple, gives an impression of an intercept when a linear trend is extrapolated to the linewidth axis. The data for sample $S50_g$ shows that the line broadening at lower frequencies could be taken to be either an effect of inhomogeneities or due to the ripple field.

4.1.4 COMPARISON OF FMR LINEWIDTH OBTAINED FROM DIFFERENT TECHNIQUES

As described in Chapter 3, three techniques have been developed for the measurement of the ferromagnetic resonance (FMR) and the magnetodynamic damping parameters in metallic ferromagnetic thin films in the 1-10 GHz range of frequencies. The first is a strip line (SL) based FMR technique developed in the 1960s. This is closely related to the standard shorted waveguide and microwave cavity field swept FMR measurement techniques, where one measures the FMR linewidth at a fixed frequency. The second utilizes vector network analyzer (VNA)

instrumentation, swept frequency at fixed field, and conversion of the S – parameters so obtained, into FMR absorption curves and extracted linewidths. The third involves the use of pulsed inductive microwave magnetometry (PIMM). This technique significantly extends work on the inductive detection of switching from the 1960s through the use of modern, fast rise time drive electronics, coplanar waveguides for simultaneous drive and detection, and digital signal processing. The Fourier transform of the PIMM response yields the FMR absorption profile vs. frequency and the corresponding linewidths.

The SL, VNA, and PIMM techniques all have advantages and disadvantages. While the strip line approach is broad band and simple to run and analyze, the sensitivity is low. The VNA approach is also broad band and takes advantage of the full amplitude and phase analysis capabilities of advanced commercial vector network analyzer instruments. This approach, however, requires careful calibration and the proper subtraction of reference signals in order to obtain accurate results. The advantages of the PIMM method lie in the use of step or impulse rather than microwave fields, data in the form of the full magnetodynamic response to the step drive, and the absence of a complicated calibration procedure. As with the VNA approach, the main PIMM disadvantage is that the data must be analyzed through a careful reference subtraction process. Many of the details of these issues will become apparent from the discussion below. For a comprehensive comparison of the techniques, in plane FMR linewidth were measured for Permalloy films on all the three systems. The samples $S50_g$ and $S100_g$ were measured on both, the PIMM

and SL-FMR system. The VNA-FMR data were taken on sample $S50_gA$, which was also sputtered at NIST, Boulder.

Figures 4.1.4 and 4.1.5 show linewidth comparison results in field linewidth ΔH vs. frequency and frequency linewidth $\Delta\omega$ vs. frequency formats, respectively. Graphs (a) in each case correspond to SL-FMR and PIMM data on sample $S50_g$ and VNA-FMR data on sample $S50_gA$. Graphs (b) correspond to SL-FMR and PIMM data on sample $S100_g$. The SL-FMR, VNA-FMR, and PIMM results are shown by solid circles, solid triangles, and open circles, respectively. The linewidth conversions were based on nominal free electron $|\gamma|/2\pi$ and H_k values of 2.8 GHz/kOe and 6 Oe, respectively, and $4\pi M_S$ value of 10.55 kG. These values are consistent with the FMR frequency vs. field data for the three samples. Error bars for each data set are on the order of the size of the data points. The straight lines show fits for the full (a) and (b) data sets in Fig. 4.1.4. The corresponding slopes and intercepts are useful parameters for comparison with typical Permalloy data in the literature. These lines carry over to the curves shown in Fig. 4.1.5.

ΔH The field format linewidth vs. frequency results in Fig. 4.1.4 show consistent results from method to method. The fitted slopes for the straight lines in (a) and (b) are 4.85 ± 0.1 Oe/GHz and 4.9 ± 0.3 Oe/GHz respectively. The corresponding intercepts for the straight line fits are 2.3 ± 0.3 and 4.1 ± 0.2 Oe, respectively. The regression coefficients for the fits shown in (a) and (b) are 0.989 and 0.995 respectively.

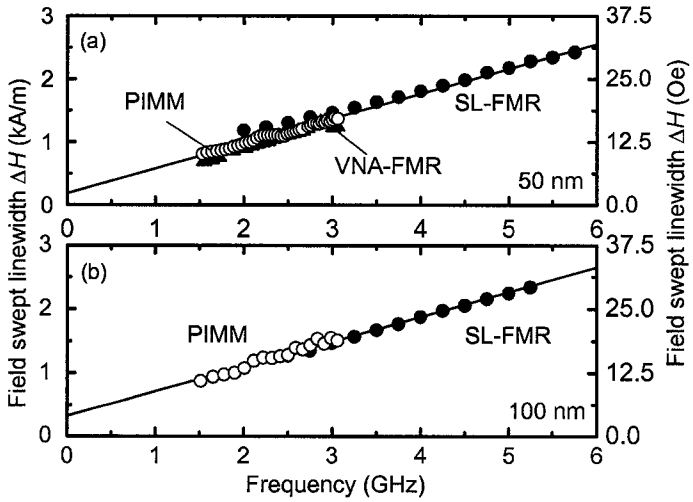

FIG 4.1.4. Comparison of the field format linewidth ΔH results obtained from the strip line, the vector network analyzer, and PIMM techniques on the 50 nm and 100 nm films. The solid circles are the SL-FMR results, the solid triangles are the VNA-FMR results, and the open circles are the PIMM results. The solid lines are linear fits to all the points. Graph (a) shows the ΔH values vs. frequency for the films $S50_g$ and $S50_g A$ and graph (b) shows the ΔH values vs. frequency for sample $S100_g$.

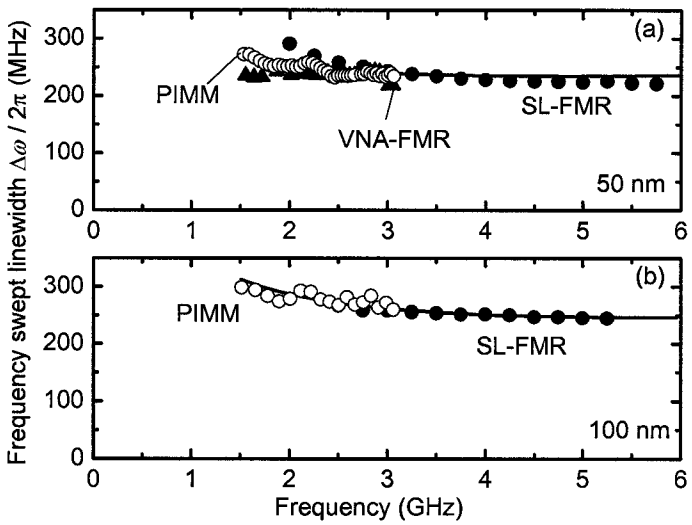

FIG 4.1.5. Comparison of the frequency format linewidth $\Delta\omega$ results obtained from the strip line, the vector network analyzer, and PIMM techniques on the 50 nm and 100 nm films. The solid circles are the SL-FMR results, the solid triangles are the VNA-FMR results, and the open circles are the PIMM results. The solid curves are the corresponding fits to the lines in Fig. 4.1.4. Graph (a) shows the $\Delta\omega$ values vs. frequency for the films $S50_g$ and $S50_g A$ and graph (b) shows the $\Delta\omega$ values vs. frequency for sample $S100_g$.

This type of linewidth vs. frequency response is similar to that found in many previous FMR experiments on Permalloy and other metal ferromagnetic films (Heinrich *et al.* 1985), (Patton 1968).

Such linewidth responses are often interpreted in terms of a combined inhomogeneous broadening and Landau - Lifshitz damping model. Within this framework, one would expect a field swept half power linewidth of the form given by Eq. (4.1.1). The slopes given above correspond to α_{sl} values of about 0.007 for both $S50_g$ and $S100_g$ films. This is a typical value for low loss metal films. Intercept ΔH_0 values in the few Oe range are also consistent with the expected field inhomogeneities due to anisotropy dispersion and other effects. The interpretation of these responses continues to be a subject of intense study.

Similar comments apply to the frequency linewidth vs. frequency presentations in Fig. 4.1.5. The data for the three techniques are consistent from method to method. The change of format expands the scatter in the data from the fit line at low frequencies. This can be made clear from the linewidth conversion formulae established above. Based on Eqs. (2.60), (2.61), and (4.1.1), one can write

$$\Delta\omega = \left(|\gamma|\Delta H_0 + 2\alpha_{sl}\omega\right)\sqrt{1+\left(\frac{|\gamma|4\pi M_s}{2\omega}\right)^2}\,. \qquad (4.1.2)$$

For Permalloy, with $|\gamma|4\pi M_s/2\pi \approx 28$ GHz, the conversion amounts effectively to a $|\gamma|4\pi M_s/2\omega$ multiplier. This results in an increase in the frequency linewidth, relative to $|\gamma|\Delta H$, as well as any corresponding scatter, especially at the low

frequency limit for the current measurements. The ΔH_0 intercept in the field linewidth vs. frequency presentation format for the data corresponds to a curvature of the $\Delta\omega$ vs. ω response as seen in Fig. 4.1.4. The levelling off in $\Delta\omega$ for $\omega > 3$ GHz or so corresponds to dominance of the $2\alpha_{sl}\omega$ term relative to the zero frequency $|\gamma|\Delta H_0$ term in Eq. (4.1.2). In this limit, the theoretical $\Delta\omega$ is just $\alpha_{sl}|\gamma|4\pi M_s$. However, work in progress indicates that there may be additional contributions to this curvature for frequencies below the 1.5 GHz limit of the data reported here.

The linewidths obtained for the Permalloy films of various thicknesses using different techniques were analysed in different ways. First, the thickness dependence of the damping parameters is examined. The damping α_{sl} and the inhomogeneity contributions were first separated by a simple linear fit and then the thickness dependence of these parameters were examined. All the films showed similar trend in linewidth with frequency. Hence frequency dependence of the linewidth is being shown for an example film $S100_g$ where the data obtained by two different measurement methods (SL-FMR and the PIMM) were used simultaneously and the frequency dependence trends were studied using different phenomenological models.

Thickness dependence of linewidth parameters for in-plane magnetized thin films

Figure 4.1.6 and 4.1.7 shows the variation of extrapolated damping parameters from the linear trend of the frequency dependence of linewidth for thickness of 5 nm

– 150 nm for SX_g samples and 10 nm – 250 nm for SX_{Si} samples. Figure 4.1.6 shows the damping parameter obtained from the slope of the linewidth vs. frequency data, α_{sl} and the Fig. 4.1.7 shows the zero-frequency intercept ΔH_0. The SX_g data are shown by solid circles in graph (a) and the SX_{Si} data shown by open circles in graph (b). The solid curves in Fig 4.1.6 correspond to the expected trend from intrinsic and eddy current contribution to linewidth. This dependence is given by (Heinrich 2003)

$$\alpha_{sl} = \alpha_{\text{int}} + \frac{|\gamma|}{6}\left(\frac{4\pi}{c}\right)^2 \frac{M_s}{\rho} d^2, \qquad (4.1.3)$$

where α_{int} is an intrinsic contribution to the damping parameter, ρ is the resistivity in CGS units and d is the film thickness. The solid lines in in Fig 4.1.6 correspond to the different values of ρ as indicated.

For both the types of samples, the values of the damping parameter increase with thickness. The α_{sl} values for the SX_g samples are generally larger than for the SX_{Si} samples with the same thickness. For the SX_g samples, the α_{sl} values show typical values in the 0.005-0.0075 range. For the SX_{Si} samples the α_{sl} values show low values in the 0.0025-0.005 range for sample thicknesses below 100 nm. However this value increases drastically for thicknesses above 100 nm, as is expected from eddy current losses.

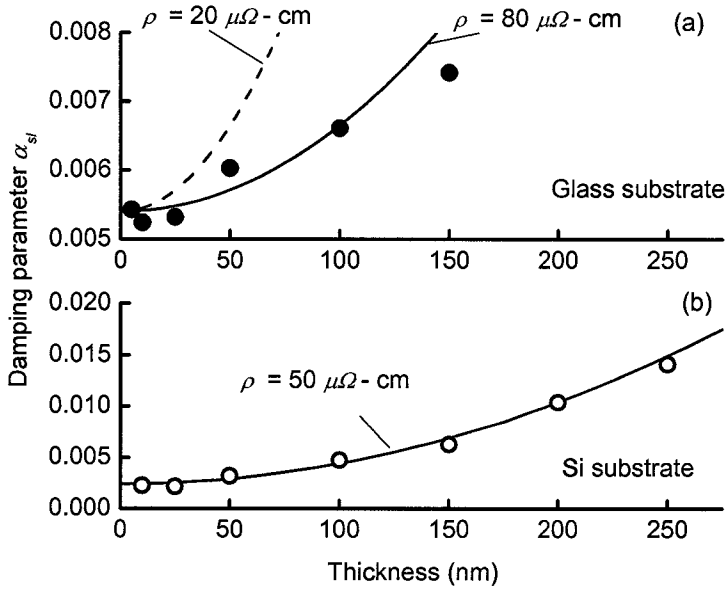

FIG.4.1.6. Damping parameter α_{sl} as a function of film thickness for different substrates as indicated. The solid curves correspond to expected values from intrinsic and eddy current contribution, taking into account the resistivity of Permalloy as 20, 80 and 50 $\mu\Omega - cm$, as indicated.

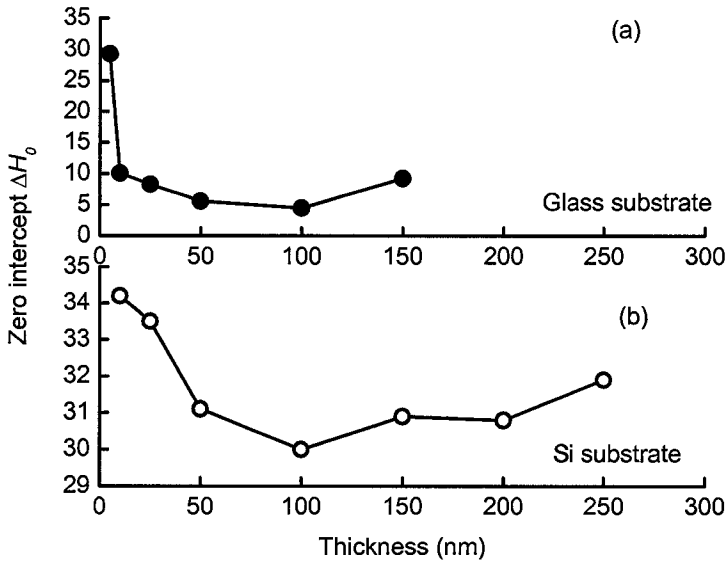

FIG. 4.1.7. Inhomogeneous linebroadening ΔH_0 as a function of film thickness for different substrates as indicated.

A comparison between the expected frequency dependence of linewidth with only intrinsic damping and the eddy current contribution taken into consideration shows that the films on the glass substrates do not show the expected increase. The values of resistivity of 50 and 80 $\mu\Omega-\text{cm}$ gave the best fit for data in graph (a) and (b) respectively. These values are slightly high for Permalloy which has the reported nominal value of ~ 20 $\mu\Omega-\text{cm}$ (Patton *et al.* 1966). The calculation for this expected value of resistivity is shown as a dashed line in graph (a). Nevertheless, results on these films, especially on the Si substrates, indicate that the increase can be attributed to eddy current losses, albeit with a large value of resistivity. Unfortunately, restrictions in the availability of experimental equipment did not make it feasible to measure the resistivity of these films.

Another point to notice is that the eddy current contribution is negligible for thicknesses below ~100 nm. The intrinsic value $\alpha_{\text{int}} = 0.005$ used for the SX_g samples is a reasonable value for metallic films. The value $\alpha_{\text{int}} = 0.0025$ used for the SX_{Si} samples is on the other hand quite low.

The inhomogeneity contribution ΔH_0 for films on glass is quite different from that for films on silicon substrates. For both types of samples, the values of the ΔH_0 for the SX_{Si} samples are higher than those for the SX_g samples. In the case of the SX_g samples, the inhomogeneous broadening of the linewidth shows an increase for thicknesses less than 25 nm. In the case of the SX_{Si} samples, the increase is gradual.

However the trend remains the same contribution increasing as one goes towards lower thicknesses.

Frequency dependence of linewidth for in-plane magnetized thin films

In this subsection we examine the frequency dependence of the field linewidth for an in-plane magnetized thin film as they look in the different scenarios offered by different damping models. The data shown in this section are for $S100_g$ sample obtained from PIMM and SL-FMR setup. The field linewidth vs. frequency dependence $\Delta H(\omega)$ is essentially linear in the frequency range studied and it extrapolates to a non-zero value at zero frequency. This kind of dependence is clearly seen in Fig. 4.1.4. The frequency swept linewidth dependence $\Delta\omega(\omega)$ typically shows an upturn for lower excitation frequencies, below 2 GHz or so, as shown in Fig. 4.1.5. This behaviour was observed also in (Schneider *et al.* 2005), (Bonin *et al.* 2005), (Kalarickal *et al.* 2006).

The linearity of $\Delta H(\omega)$ dependence suggests a Landau-Lifshtiz or Gilbert type of damping, which could be interpreted also as a magnon-electron scattering physical mechanism. On the other hand, an apparent intercept in the field swept linewidth $\Delta H(\omega)$ or the upturn in the frequency swept linewidth $\Delta\omega(\omega)$ can be interpreted in three ways.

The first interpretation is that of a straightforward addition of a constant inhomogeneous line broadening term to the LL linewidth. This kind of analysis has been utilized by several authors in the past 40 years (Rossing 1963), (Spano and

Bhagat 1981), (Kraus *et al.* 1981), (Cochran *et al.* 1982), (Heinrich *et al.* 1985), (Celinski and Heinrich 1991). This has been discussed in the preceding section, in Figs. 4.1.4 and 4.1.5. The frequency dependence of the linewidth follows the Eq. 4.1.1 with α_{sl} replaced by α_{LL} . The point to note is that the physical linebroadening mechanism, when considered in the $\Delta\omega$ vs. ω format does show an upturn at lower frequencies as was discussed in connection to Eq. (4.1.2).

The second interpretation is that of a combination of the LL model with the CCOT model discussed in Section 2.2.4. As shown in Fig. 2.7. the CCOT model predicts a low-frequency upturn in the frequency linewidth. Figures 4.1.8 and 4.1.9 show the linewidth vs. frequency in a frequency and field linewidth format respectively for the 100 nm film. The figure also shows a fit to a combined LL and CCOT model to the data. The open circles show the data and the solid lines are the fit. The dashed line in Fig. 4.1.8 shows the LL dependence alone The equation for frequency linewidth

can be evaluated from Eq. (2.46) and (2.55). In the limit of low frequencies this equation has a form

$$\Delta\omega = \left(\frac{|\gamma| 4\pi M_s}{T_2 \omega} + 2\alpha_{LL}\omega \right) \sqrt{1 + \left(\frac{|\gamma| 4\pi M_s}{2\omega} \right)^2} \,. \qquad (4.1.4)$$

The best fit to data yields the values $\alpha_{LL} = 0.0076$ and $T_2 = 1.42 \times 10^{-6}$ s .

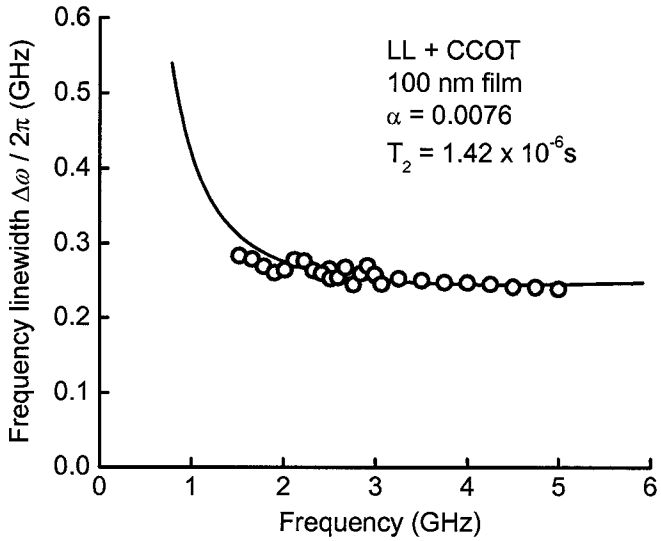

FIG 4.1.8. Frequency linewidth $\Delta\omega$ results vs. frequency obtained from the strip line, and PIMM techniques for sample $S100_g$. The open circles are the data and the solid curve is a calculation based on LL and constrained COT type of models with parameters as indicated.

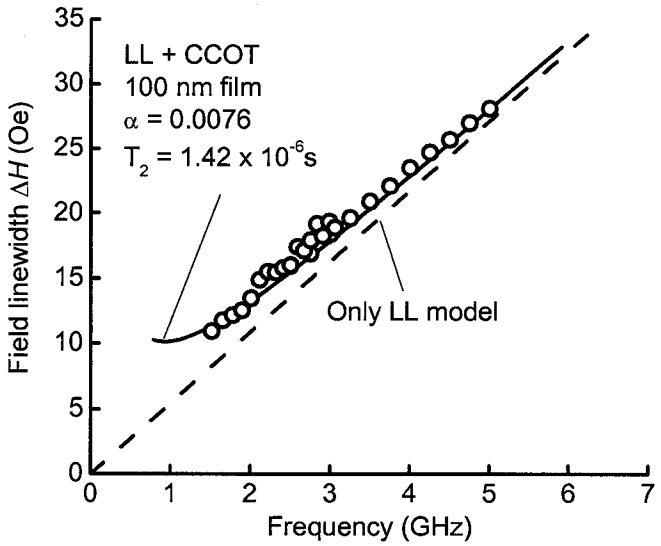

FIG 4.1.9. Field linewidth ΔH results vs. frequency obtained from the strip line, and PIMM techniques for sample $S100_g$ The open circles are the data and the solid curve is a calculation based on LL and constrained COT type of models with parameters as in Fig 4.1.8. The dashed line is the dependence due to the LL model alone.

The frequency linewidth contribution due to the CCOT model predominates the values at lower frequencies because of its dependence on the internal field. As follows from the Eq. (4.1.4) at low frequencies $\Delta\omega \propto 1/\omega^2$. The $\Delta\omega$ data do not show such a sharp upturn as indicated by the model, however the fit is still quite reasonable. As shown in Fig. 4.1.8, this leads to the low-frequency upturn in the field linewidth and yields an apparent non-zero linewidth intercept at zero frequency. The CCOT contribution to the linewidth diminishes rapidly as the frequencies increase and is negligible by 7 GHz or so.

The third interpretation is that of a combination of the LL model with a field dependent inhomogeneity line broadening due to magnetization ripple. This linebroadening mechanism was discussed in Section 2.4.4. Figures 4.1.10 and 4.1.11 show the linewidth vs. frequency in a field and frequency linewidth format respectively for the 100 nm film. The figures also show fits to a combined LL and ripple field broadening to the data. The open circles show the data and the solid lines are the fits. The dashed line in Fig. 4.1.11 shows the LL dependence alone. The equations given for the fit are discussed in Chapter 2. The relation between the $\Delta\omega$ and the ΔH values is given by equation similar to Eq. (4.1.4).

$$\Delta\omega = \left(|\gamma|\Delta H_{ripp} + 2\alpha_{LL}\omega\right)\sqrt{1+\left(\frac{|\gamma|4\pi M_s}{2\omega}\right)^2}, \qquad (4.1.5)$$

where ΔH_{ripp} is given by second term at the right-hand-side of Eq. (2.86). The $\alpha_{LL} = 0.0076$ value is the same as for previous fits. The ripple field $H_r = 1.9$ Oe

was found from the fit to the data. The anisotropy field parameter $H_k = 5.6$ Oe was obtained from the static magnetization data.

The frequency linewidth contribution due to the magnetization ripple also dominates at lower frequencies because of its dependence on the internal field. There is a large upturn in linewidth at lower frequencies. This model does fit the $\Delta\omega$ quite well. The field linewidth contribution due to the ripple effect shows a slow rise at lower fields due to the effect of the ellipticity factor.

One can compare the calculations in Figs 4.1.11 to the LL dependence alone, as shown by the dashed line. It can be seen that the slow rise in the ripple effect when combined with the LL model gives an impression of a linebroadening at lower frequencies, which increases rapidly at lower frequencies. Another interesting aspect to this calculation is the effect of the ripple field at higher frequencies. While it was usually assumed that the effect of the ripple broadening is negligible at higher frequencies, one can see that this effect is quite pronounced.

Hence one can see that the FMR linewidth data vs. frequency can be interpreted in at least three ways. Phenomenologically the linewidth shows a frequency dependence predicted by the LL and the CCOT models. Physically this can be interpreted as a combination of magnon electron scattering, and a linebroadening contribution due to inhomogeneities. If the contribution due to inhomogeneities is independent of the applied field then the total effect is a simple addition of a constant ΔH_0 to the magnon electron scattering contribution.

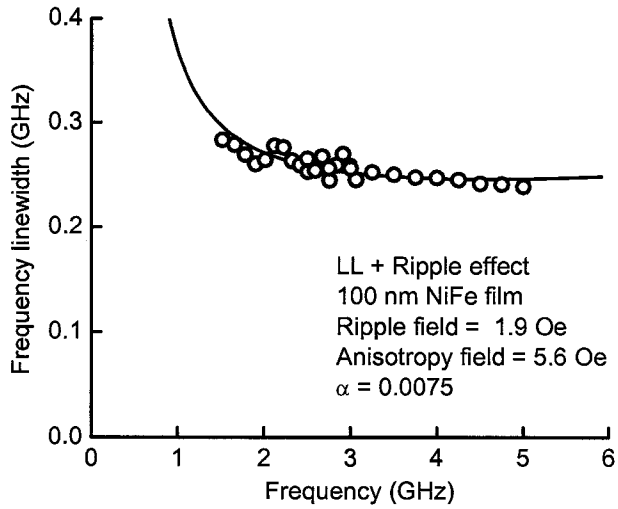

FIG 4.1.10. Frequency linewidth $\Delta\omega$ results vs. frequency obtained from the strip line, and PIMM techniques for sample $S100_g$. The open circles are the data and the solid curve is a calculation based on LL type of model and a ripple field broadening with parameters as indicated.

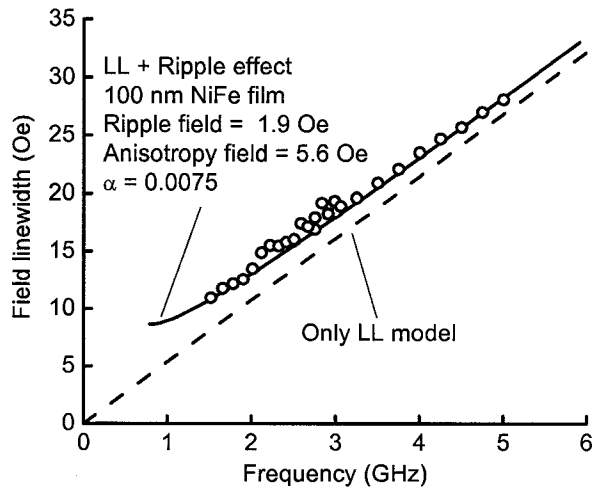

FIG 4.1.11. Field linewidth ΔH results vs. frequency obtained from the strip line, and PIMM techniques for sample $S100_g$. The open circles are the data and the solid curve is a calculation based on LL type of model and a ripple field broadening with parameters as in Fig 4.1.10. The dashed line is the dependence due to the LL model alone.

Field due to inhomogeneities can also be in the form of the magnetization ripple, and the contribution due to this ripple tends to increase at lower frequencies. All of these give frequency dependence consistent with the linewidth vs. frequency data obtained with both, the FMR set up (SL and shorted waveguide setups) and the PIMM setup, in the 1.5 – 5 GHz range.

4.1.5 FMR LINEWIDTH FOR OBLIQUELY MAGNETIZED THIN FILMS

The previous sections described the frequency, thickness dependences of in-plane magnetized FMR linewidth for Permalloy films deposited on glass and Si and used the linewidth obtained to compare three different measurement techniques. This section describes the FMR field swept linewidths ΔH as a function of the external magnetic field angle θ_H to the sample plane.

Figure 4.1.12 shows the sample geometry. The external field **H** is applied at an angle of θ_H with the film normal, or $Z-$axis in the sample frame. The magnetization static equilibrium position lies at an angle θ_M to the $Z-$axis. This angle has to be determined.

The rotation from the sample X,Y,Z frame to the precessional x,y,z frame may be described by a rotation matrix

$$\ddot{R} = \begin{pmatrix} \cos\theta_M & 0 & -\sin\theta_M \\ 0 & 1 & 0 \\ \sin\theta_M & 0 & \cos\theta_M \end{pmatrix}. \tag{4.1.6}$$

The relation between a general vector $\mathbf{v}$ and a tensor $\ddot{T}$ in both frames is then described by

$$\begin{aligned} \mathbf{v}_{xyz} &= \ddot{R} \cdot \mathbf{v}_{XYZ}, \\ \ddot{T}_{xyz} &= \ddot{R} \cdot \ddot{T}_{XYZ} \cdot \ddot{R}^{-1} \end{aligned} \tag{4.1.7}$$

The static equilibrium position may be evaluated from Eq. (2.13). First, the external field $\mathbf{H}$ in the x, y, z frame has components

$$\mathbf{H}_{xyz} = \ddot{R} \cdot \begin{pmatrix} H\sin\theta_H \\ 0 \\ H\cos\theta_H \end{pmatrix} = \begin{pmatrix} -H\sin(\theta_M - \theta_H) \\ 0 \\ H\cos(\theta_M - \theta_H) \end{pmatrix}. \tag{4.1.8}$$

Second, the demagnetizing tensor $\ddot{N}$ in x, y, z frame has components

$$\begin{aligned} \ddot{N}_{xyz} &= \ddot{R} \cdot \begin{pmatrix} 0 & 0 & 0 \\ 0 & 0 & 0 \\ 0 & 0 & 1 \end{pmatrix} \cdot \ddot{R}^{-1} \\ &= \begin{pmatrix} \sin^2\theta_M & 0 & -\sin\theta_M\cos\theta_M \\ 0 & 0 & 0 \\ -\sin\theta_M\cos\theta_M & 0 & \cos^2\theta_M \end{pmatrix}. \end{aligned} \tag{4.1.9}$$

The static equilibrium condition (2.13) is therefore transformed to

$$2H\sin(\theta_M - \theta_H) = 4\pi M_s \sin 2\theta_M \tag{4.1.10}$$

As expected, Eq. (4.1.10) is satisfied if $\theta_M \geq \theta_H$.

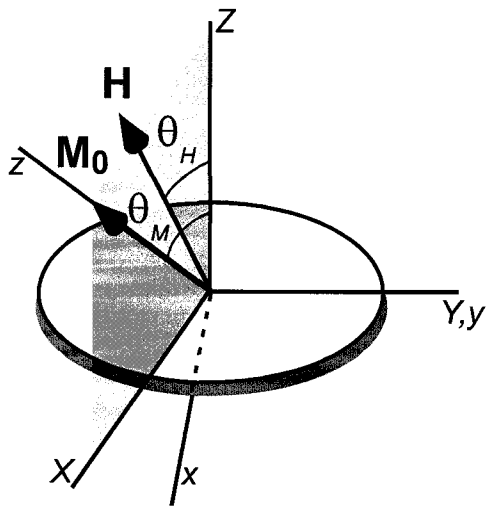

FIG. 4.1.12. Sample and field geometry for obliquely magnetized thin film FMR experiment.

The internal static field is

$$\begin{aligned} H_i &= H_z - 4\pi M_s N_{zz} \\ &= H\cos(\theta_M - \theta_H) - 4\pi M_s \cos^2\theta_M . \end{aligned} \tag{4.1.11}$$

Note that Eq. (4.1.10) and (4.1.11) may be written also in the form

$$\begin{aligned} &H_i \sin\theta_M = H\sin\theta_H , \\ &(H_i + 4\pi M_s)\cos\theta_M = H\cos\theta_H . \end{aligned} \tag{4.1.12}$$

Equation (4.1.12) represents the continuity condition for tangential component of the magnetic field and normal component of magnetic induction at the film surface.

The resonance condition is evaluated from Eq. (2.16) and (2.18)

$$\left(\frac{\omega_0}{|\gamma|}\right)^2 = H_i\left(H_i + 4\pi M_s \sin^2\theta_M\right). \tag{4.1.13}$$

Figure 4.1.13 shows the resonance field position as a function of angle θ_H to the sample normal. Graphs (a) and (b) show the data for the $S100_g$ and $S150_{Si}$ samples respectively at a frequency of 4 GHz. Solid circles show the experimental data and the solid line shows a theoretical fit of the data to the FMR resonance condition (4.1.13) as discussed above. The fit for the data yielded a value for $|\gamma|/2\pi$ of 2.8 GHz/kOe. The $4\pi M_s$ values were obtained as 10 and 10.54 kG for the $S100_g$ and $S150_{Si}$ samples respectively. These values are acceptable literature values for Permalloy films and the fits are quite reasonable for these data.

Figure 4.1.14 shows the variation of FMR linewidth ΔH as a function of angle θ_H to the sample plane. Graphs (a) and (b) show the data for the $S100_g$ and $S150_{Si}$ respectively at a frequency of 4 GHz denoted by the solid and open circles respectively. The solid line shows a fit to the data with the Landau-Lifshitz model. The fit comprises Eq. (2.46), (2.60), (2.61) and (4.1.13). The fit to the data looks reasonable. The linewidth $\Delta H_{\|}$ in the parallel configuration $(\theta = 90°)$ for the $S100_g$ sample is smaller than the linewidth $\Delta H_{\perp}$ in the perpendicular configuration $(\theta = 0°)$. On the other hand, the linewidth $\Delta H_{\|}$ in the parallel configuration for the $S150_{Si}$ sample is larger than the linewidth $\Delta H_{\perp}$ in the perpendicular configuration. The comparisons between linewidth in these two configurations will be considered in detail in the next section. It is important to note that for the LL damping model $\Delta H_{\|} = \Delta H_{\perp}$.

Other than for the in-plane and perpendicular configuration, the angular dependence of linewidth shows a reasonable agreement with LL damping model. This corroborates the linear frequency dependence of the field swept linewidth from the previous section. However, the total linewidth in the parallel and perpendicular configurations not being equal points to extrinsic contributions to the linewidth. This trend transcends deposition methods of Permalloy films. Therefore the magnetization relaxation seems to largely follow a Landau-Lifshitz type of relaxation model. The extrinsic contribution appears in the form of inhomogeneous linebroadening which results in an apparent linewidth intercept at zero frequency, and a possible two-magnon scattering contribution which gives a larger contribution in the parallel than the perpendicular configuration. This is also typical of most metal films.

The out of plane angular dependence of FMR linewidth shows that the predominant relaxation mechanism in metals is given by the Landau Lifshitz model. However since the parallel and perpendicular linewidths are not equal, one needs to take into consideration other mechanisms such as inhomogeneous linebroadening or two magnon scattering.

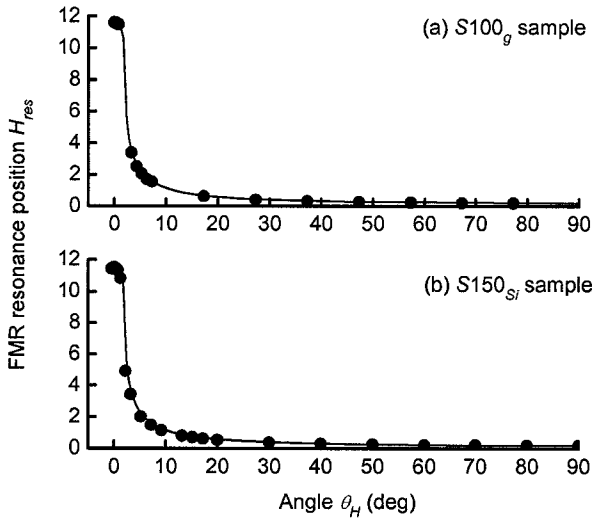

FIG. 4.1.13. Angle dependence of FMR position in field for $S100_g$ and $S150_{Si}$ samples at 4 GHz.

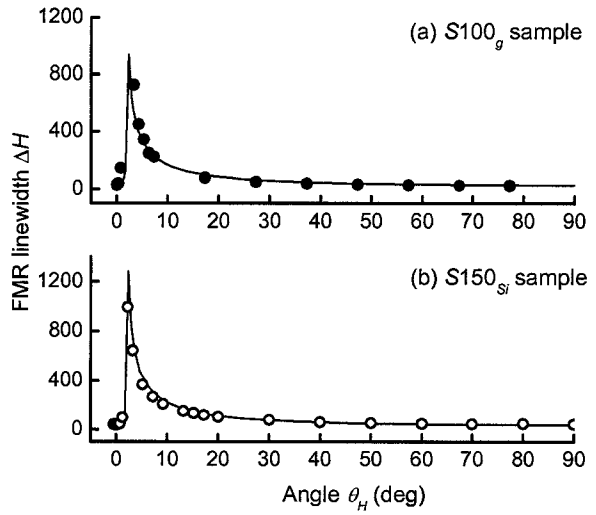

FIG. 4.1.14. Angle dependence of FMR linewidth for $S100_g$ and $S150_{Si}$ samples at 4 GHz.

4.1.6 FMR LINEWIDTH FOR PERPENDICULARLY MAGNETIZED FILMS

The frequency dependence of field linewidth in perpendicularly magnetized films was studied for the films on both glass and Si substrates. For glass substrates the film $S100_g$ was studied. For the Si substrates, the samples $S50_{Si}$, $S100_{Si}$ and $S150_{Si}$ were studied. For comparison, linewidth data for parallel configuration are also shown.

Fig 4.1.15 shows $\Delta H_{\perp}$ and $\Delta H_{\parallel}$ data for $S100_g$ film. The solid circles are the data for the perpendicular configuration. The solid triangles are the data for the parallel configuration. There are several interesting aspects to this set of data. Firstly, the data for perpendicular configuration show a rapid increase below 2 GHz. The linewidth increased from 21 Oe at 2 GHz, to about 32 Oe at 1.7 GHz. This kind of increase is indicative of linebroadening due to the unsaturated state of the sample. The second interesting aspect is that the parallel and perpendicular linewidth have linear frequency dependence. The slopes of both the sets of linewidth data as a function of frequency are nearly the same, indicating LL or Gilbert type of damping. The third aspect is that the perpendicular configuration data show larger values than the parallel configuration data.

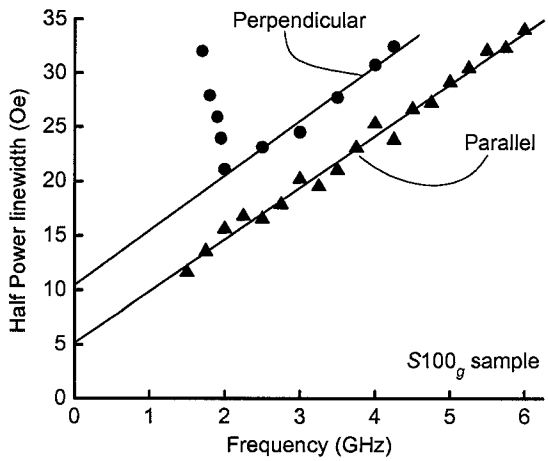

FIG. 4.1.15 Linewidth as a function of frequency in two orientations of the applied field, to the film plane for $S100_g$ sample. The solid circles show the perpendicular data and the solid triangles show the parallel data.

Fig 4.1.16 shows the $\Delta H_{\perp}$ and $\Delta H_{\parallel}$ data for $S50_{Si}$, $S100_{Si}$ and $S150_{Si}$ films. The solid circles are the data for the perpendicular configuration. The solid triangles are the data for the parallel configuration. These data also show linear dependence with frequency for all the samples, with the parallel and perpendicular linewidths having nearly the sample slopes. The data also show that for $S50_{Si}$, the $\Delta H_{\parallel}$ and $\Delta H_{\perp}$ values coincide. For the $S100_{Si}$ and $S150_{Si}$ samples, the $\Delta H_{\parallel}$ values are larger than the $\Delta H_{\perp}$ values, with the difference increasing as the thickness of the film increases.

Due to the demagnetization field, the magnetization in thin films prefers to be in the plane of the film. Therefore to magnetize the films perpendicular to plane, it is necessary to apply large fields. It was always believed that fields only slightly larger

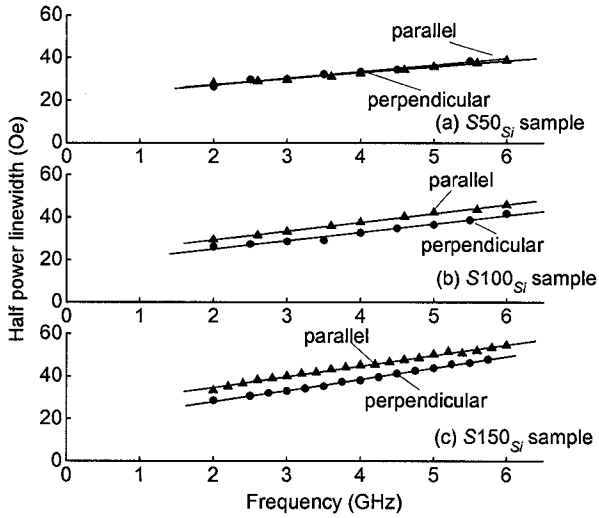

FIG. 4.1.16 Linewidth as a function of frequency in two orientations of the applied field, to the film plane for $S50_{Si}$, $S100_{Si}$, $S150_{Si}$ samples. The solid circles show the perpendicular data and the solid triangles show the parallel data.

than the $4\pi M_s$ values were enough to saturate a thin film perpendicular to the plane. However the data in Fig. 4.1.15 show that this is not the case. The onset of the large line broadening due to the unsaturated state occurs at frequencies only slightly less than 2 GHz, which correspond to fields about 700 Oe in excess of $4\pi M_s$.

In this figure, the fact that the linewidth in the perpendicular configuration $\Delta H_{\perp}$ was larger than the linewidth in the parallel configuration $\Delta H_{\parallel}$ cannot be explained by two magnon scattering. This may however be qualitatively understood in the scenario of inhomogeneous linebroadening due to a variation in the magnetic properties that sets the resonance fields far apart enough so that the FMR line is a superposition of all the spectra. If the resonance condition is dependent on materials and other parameters say x_i, then the linewidth due to inhomogeneities is given by the spread in resonance frequencies $\Delta\omega_0 = \sum |\partial\omega/\partial x_i| \Delta x$ (McMichael *et al.* 2003).

In conversion from the frequency linewidth to the field linewidth, this would imply an increase in the contribution for the perpendicular configuration. This is because of the absence of the strong elliptical polarization in the perpendicular configuration which is present in the parallel configuration (Heinrich, 2003). Similar behaviour of $\Delta H_{\perp} > \Delta H_{||}$ was also obtained by Patton (Patton 1968) (Patton *et al.* 1975) but the linewidth did not show the same frequency dependence as is seen here.

As the data in Fig. 4.1.16 show, at a given frequency, for the films on Si substrates, the linewidth in the perpendicular configuration remains constant. Bertaud and Pascard (Bertaud and Pascard 1965) measured $\Delta H_{\perp}$ and $\Delta H_{||}$ on thin Permalloy (83% Ni, 17% Fe) films as a function of thickness at 9.4 GHz. They also observed that the $\Delta H_{\perp}$ values were fairly constant whereas the $\Delta H_{||}$ increases with film thickness. The trends of $\Delta H_{||} \geq \Delta H_{\perp}$ are predictable by two magnon scattering mechanism. For a thickness of 50 nm, the linewidths in both the orientations is equal which shows that two-magnon scattering is negligible in this film. For $S100_{Si}$ and $S150_{Si}$, there might be a contribution due to two-magnon scattering.

An interesting aspect to the data on the Permalloy films presented here is that the in plane and perpendicular linewidth both have a linear frequency dependence. The frequency dependence of $\Delta H_{\perp}$ has shown different trends in this material itself. Patton's data in 1968, showed a constant in the $\Delta H_{\perp}$ values for thin Permalloy films over a frequency range of 1 to 4 GHz. (Patton 1968) It was concluded therefore that the intrinsic ferromagnetic relaxation process in thin metal films was better

characterized by a relaxation rate type like the Bloch Bloembergen, rather than a Landau-Lifshitz or Gilbert type of modelling. Later work by Patton, Frait and Wilts in 1975 on thin Permalloy films showed a different trend.(Patton *et al.* 1975) The $\Delta H_{\perp}$ data coincided with the $\Delta H_{\|}$ values at higher frequencies of 25 and 36 GHz. The $\Delta H_{\perp}$ values levelled off at lower frequencies below 10 GHz, and again, they were larger than the $\Delta H_{\|}$ values. Perpendicular linewidth reported more recently, on 10 nm Permalloy films show linear dependence on frequency, with the coincident values in the parallel configuration (Twisselmann and McMichael 2003). Linear dependence of linewidth on frequency in the case of the measured thin Permalloy films in this study hence indicate that LL type of damping mechanism is more suited for the modelling of linewidth in Permalloy films. At lower frequencies, linewidth in the perpendicular configuration is extremely sensitive to the angle of the applied field to the plane of the film. Hence the early data by Patton (Patton 1968), (Patton *et al.* 1975) where the $\Delta H_{\perp}$ values were more or less constant with frequency, may be attributed to a misalignment of the film normal to the applied field.

4.1.7 SUMMARY AND CONCLUSIONS

Section 4.1 described the experimental results obtained on thin Permalloy films. FMR linewidth were presented for in-plane magnetized sputtered films for two different types of substrates. Results for Permalloy films on glass substrates were used for comparison of FMR linewidth obtained from the different measurement

techniques described in Chapter 3. Out of plane angle dependence of FMR linewidth results were presented for these films. FMR linewidth results were also presented for perpendicularly magnetized films.

The field linewidth data for in-plane magnetized thin films were linear in frequency implying that the intrinsic relaxation could be characterised by a Landau-Lifshitz type of modelling or a magnon electron scattering mechanism. Additional linebroadening effects were also observed which could be modelled either by a field independent inhomogeneous line broadening ΔH_0 or a field dependent effect due to magnetization ripple effect. It can be seen that the effect due to ripple broadening could not be ignored even at high frequencies.

Both these effects gave values of LL damping parameter α_{LL}, which were reasonable for metallic ferromagnetic films. The out-of-plane angular dependence of linewidth showed that for the most part, the linewidth could be modelled with a constant value of damping parameter α_{LL}.

The perpendicular-to-plane linewidth measurements showed that a considerably large value of field is required to completely magnetize the Permalloy films to saturation. The $\Delta H_{\|} > \Delta H_{\perp}$ trend shows that two magnon scattering can account for the linewidth mechanism in some films. However in one of the films, this kind of microwave relaxation cannot account for the $\Delta H_{\|} < \Delta H_{\perp}$ trend.

In all cases, the in plane, the angle dependence, and the perpendicular to plane FMR linewidth data indicate that the relaxation mechanism can be successfully modelled by a LL or Gilbert type of phenomenology. This also points to the

relevance of magnon electron physical mechanism for damping, which is a viscous damping type mechanism, as suggested by the Gilbert phenomenology.

SPECIAL ACKNOWLEDGEMENTS

The author would like to acknowledge Dr. T. J. Silva for providing the films and Dr. M. J. Schneider, for help with the microwave measurements on PIMM and and Dr. P. Kabos for the VNA FMR data.

------- § -------

4.2 FERROMAGNETIC RESONANCE IN NITROGENATED IRON-TITANIUM FILMS

4.2.1 INTRODUCTION AND BACKGROUND

Recently, the need for higher density magnetic information storage has led to a high level of interest in perpendicular media. High magnetization nanostructured films with soft magnetic properties are the materials of interest for use in write heads and as a soft underlayer (SUL) in most perpendicular media designs. The desirable properties for this application and for use in the communication industry are high magnetization, low coercive force, and low magnetic damping. In addition, it is desirable to have a reasonably high specific resistivity in order to have low eddy current losses.

A new class of iron based alloys with superior soft magnetic behaviour, low losses and saturation magnetization much higher than Permalloy, was reported for first time by Yoshizawa *et al* (Yoshizawa *et al.* 1988). Recently, nanocrystalline Fe-N films with similar magnetic properties have attracted interest as good SUL candidates with similar attractive magnetic properties. In Fe-N systems, the interstitial N-atoms are instrumental in refining the grain structure of the film and expanding the lattice, leading to a structural change. Generally, a small amount of a third element for example, Al, Zr, Co, Ta, Ti, is required to improve the thermal stability of the materials. Fe–X–N alloys have demonstrated a low coercivity and high saturation magnetization. The element X replaces Fe and improves the soft magnetic properties. Nitrogen incorporation also depends on the nature of X (Viala 1996). Some of the systems under recent study have been Fe–Zr–N, (Craus *et al.* 2004), (Craus *et al.* 2002), (Chevan 2002) Fe–Co–N (Sun *et al.* 2002), Fe–Ta–N, (Viala *et al.* 1996) and Fe–Ti–N (Alexander *et al.* 2000) films.

High-frequency performance of Fe–X–N alloys has also become increasingly important and an improved understanding of the correlation between microstructure, micromagnetic structure, and high-frequency performance has become critical. There has been limited work on the ferromagnetic resonance response in these films (Rantschler 2003). A correlation was found between the mean grain diameter of the film and the linewidth broadening which was interpreted to be the result of a ripple field effect. Rantschler (Rantschler 2003) indicated that as the grain size approached the exchange length of the material, the contribution due to linebroadening is

reduced. This reflects that the contribution to FMR linewidth of the intra-granular variations in exchange coupling is large and in some films, possibly more important than large-scale inhomogeneities. Ferromagnetic resonance (FMR) measurements (Rantschler *et al.* 2003), (Rantschler 2003) correlate extrinsic damping to grain size, and show a leveling off of the FMR linewidth extrapolation to zero frequency for grain sizes below about 10 nm. This response might also be a direct effect of structural transition observed by Ding *et al.*(Ding *et al.* 2001)

However, the connection between the grain size, the structural changes with the atomic percentage of nitrogen and the linewidth was not established completely and whether the actual origin of the change in linewidth with the nitrogen content was a grain size effect or due to structure change remained to be resolved.

The goal of the present work was to study the microwave damping properties in soft, polycrystalline Fe-Ti-N thin films, as a function of nitrogen content in the alloy. The nitrogen content x_N was varied from 0 to 12.7 atomic weight percentage, which gave a magnetization variation from 20 kG – 13 kG, and a grain size variation from 28 nm – 4 nm.

Ferromagnetic resonance (FMR) linewidth was studied as a function of frequency in the 2-40 GHz range for these films. The frequency dependence of FMR linewidth showed that the damping and the line broadening strongly depended on the nitrogen content in the film. Section 4.2.2 gives the materials details, resistivity and static magnetic properties for these films and presents a discussion on the relation between

the static magnetic properties and the structure of the Fe-Ti-N systems. Section 4.2.3 gives the ferromagnetic resonance results and discussion.

4.2.2 MATERIAL DETAILS, RESISTIVITY AND STATIC MAGNETIZATION RESULTS

The Fe-Ti-N films used for this study were prepared by DC magnetron sputtering in an N/Ar atmosphere at the University of Alabama. The details of overall film properties and preparation procedures are given in (Ding *et al.* 2001) and (Rantschler and Alexander 2003). A DC magnetic field of about 300 Oe was applied in the plane of the substrates during sputtering to obtain in-plane uniaxial anisotropy. The Ar flow rate and pressure were held constant. The flow rate was changed to vary the nitrogen pressure from 0 to 1 mT. The nitrogenated thin films were deposited on 1×1 cm square glass substrates. The thickness for all these films was estimated to be 50 nm. The films were annealed in a field of 300 Oe at a temperature of 100°C. X-ray photoelectron spectroscopy was used to measure the atomic concentrations of different elements. All films had about 3 at. % Ti. The nitrogen content x_N was found to vary from 0 to 12.7 at. %. Transmission electron microscopy was used to determine the grain sizes of the nanoparticles. The average grain size varied from 28 nm for the Fe-Ti film without nitrogen to about 4 nm for the Fe-Ti-N film with 12.7 at. % of nitrogen.

Resistivity

Resistivity in these films was measured by the four point Van der Pauw method at room temperature. Details of this technique are given in Appendix I. The resistivity values were then used to calculate the conductivity. Figure 4.2.1 shows the conductivity values σ vs. N-content. The solid straight lines are guides to the eye. The dashed line indicates the x_N value at which the rate of decrease in conductivity changes. The addition of high resistivity metals like Ti ($\rho_{Ti} = 42\times10^{-6}\Omega$ cm) serves to increase the film resistivity. The resistivity ρ of these materials are in general larger than pure bulk materials, ($\rho = 10\times10^{-6}\Omega$ cm, for pure Fe). The conductivity data in the figure shows a decrease with the increase in x_N. The slope of the decrease in conductivity changes at an x_N value of about 7 %.

The relationship between the change in conductivity values and the nitrogen

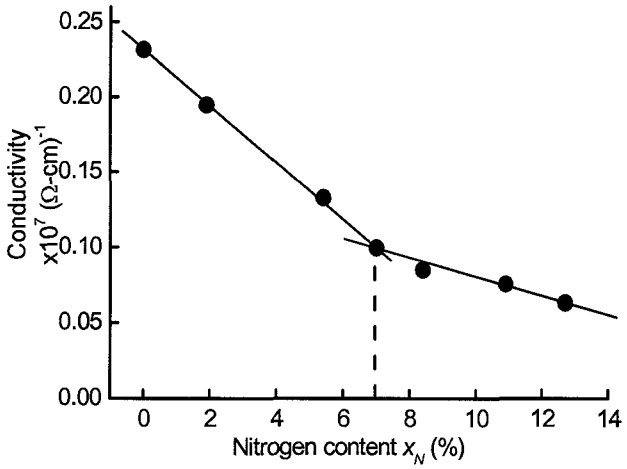

FIG. 4.2.1. Conductivity as a function of nitrogen content x_N. The inset shows the values of resistivity ρ as a function of x_N.

content is complex. When nitrogen is added to the Fe-Ti matrix, it occupies interstitial sites.(Ding *et al.* 2001) In contrast to metals, nitrogen has almost no electronic affinity for electrons, hence the increase of resistivity with x_N is not be related to mere nitrogen incorporation in the lattice. The observed increase may reflect two main indirect contributions to the scattering of the conduction electrons, (1) the grain boundary scattering due to the decrease of grain size and (2) the lattice distortion scattering due to interstitial incorporation of nitrogen in the matrix, as will be elaborated below.

Saturation magnetization

A change in the nitrogen content also leads to a change in the magnetization of the alloy and grain size in the film. A Quantum Design (MPMS *XL*) Superconducting

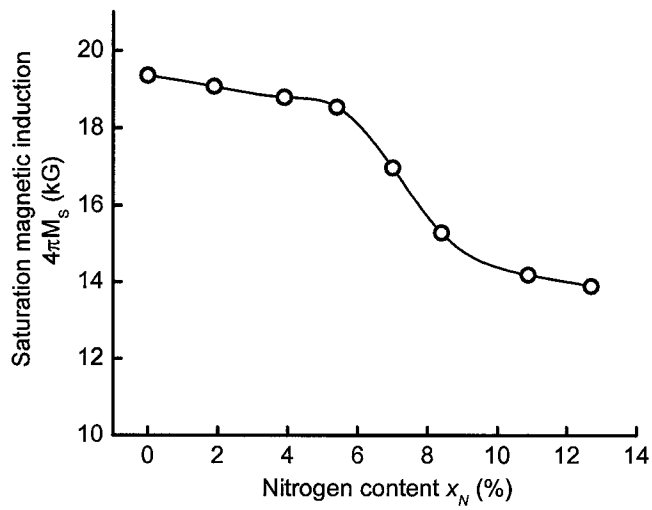

FIG. 4.2.2 Saturation magnetic induction as a function of nitrogen content x_N

Quantum Interference Device (SQUID) magnetometer was used for the magnetization measurements (Das *et al.* 2006). These measurements were made as a function of temperature and applied field. A field of 100 Oe was sufficient to saturate these films. The saturation induction was obtained at a fixed static field $H = 1$ kG in the temperature range 2 to 300 K. The magnetization M vs. field measurements were done at select temperatures in the $-100 \text{ Oe} \leq H \leq 100 \text{ Oe}$ range. Figure 4.2.2 gives the saturation magnetic induction $4\pi M_S$ values for the FeTiN films as a function of x_N. The $4\pi M_S$ values show a decrease with the N-content. The saturation magnetization in such films as FeTaN films was also reported to decrease with nitrogen incorporation. (Viala *et al.* 1996) This decrease can be related to the increase in lattice volume due to nitrogen incorporation at the interstitial sites. A sharp decrease in $4\pi M_s$ has been observed for the 6 – 8 at. % nitrogen range. These data give clear evidence for some sort of a structural transition in the x_N = 6 - 8 at. % range.

Hysteresis loops

Figure 4.2.3 show complete hysteresis loops for two samples, one for $x_N < 7$ at. % (3.9 at. %) and one for $x_N \geq 7$ at. % (10.9 at. %). The magnetization data are cast in terms of reduced saturation magnetization M / M_S for easy comparison. All the hysteresis loop measurements were performed in plane, with the static field applied along the uniaxial easy direction. For $x_N < 7$ at. % films, the hysteresis loops are more square than those for $x_N \geq 7$ at. %. This points to changes in the remanance

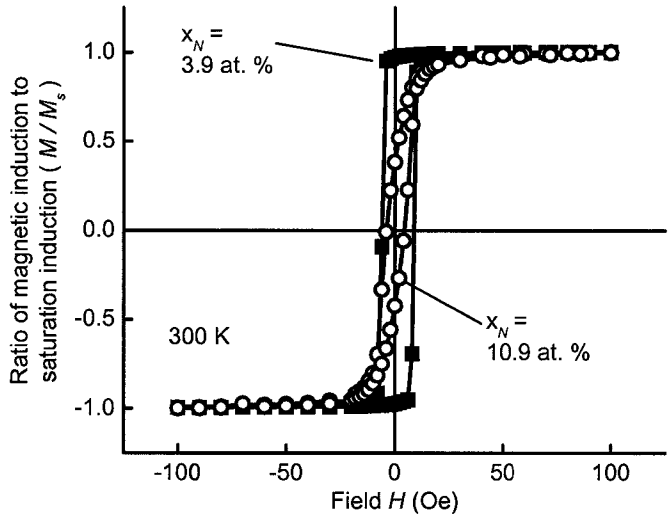

FIG. 4.2.3. Hysteresis loops for $x_N = 3.9$ at. % and 10.9 at. %

and the coercive force as nitrogen content is varied. These changes will be elaborated on below.

Remanance

Figure 4.2.4 shows the ratio of the remanence $M_r = M(H = 0)$ to the saturation induction (M_r / M_s) as a function of nitrogen concentration x_N. The solid lines show the theoretical M_r / M_s values predicted by the Stoner-Wohlfarth (SW) model for randomly oriented non-interacting single-domain particles with cubic and uniaxial anisotropy as indicated.(Stoner and Wohlfarth 1948) The SW model with a positive first-order cubic magnetocrystalline anisotropy constant i.e. $K_1 > 0$ gives $M_r = 0.83\, M_s$. This condition of $K_1 > 0$ is satisfied for Fe.(Chikazumi 1997)

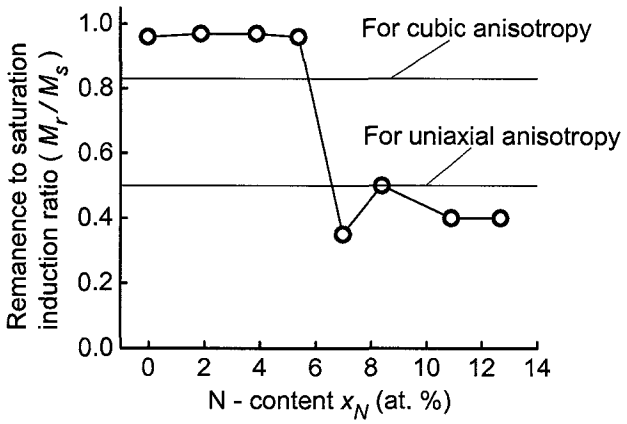

FIG. 4.2.4. Remanance to saturation magnetizaton ratio as a function of nitrogen content.

For uniaxial anisotropy, the SW model predicts $M_r = 0.5\,M_s$. The M_r / M_s values for the $x_N < 7$ at. % films are close to cubic anisotropy. This indicates that the cubic magnetocrystalline anisotropy dominates in this range. For $x_N \geq 7$, the M_r / M_s values drop to about 0.5, which suggests the dominance of the uniaxial anisotropy. Recent theoretical calculations predicted a similar trend in the M_r / M_s ratio in systems with competing cubic and uniaxial anisotropy of randomly oriented magnetic nanoparticles. (Geshev *et al.* 1998) Therefore, the variation in the M_r / M_s values with x_N indicates a competition between the magnetocrystalline and induced anisotropy in these Fe-Ti-N films (Das *et al.* 2006).

Coercive force

Figure 4.2.5 shows the variation of coercive force H_c as a function of nitrogen content x_N at room temperature. Coercive force is minimum for the 7 at. % nitrogen content film. For $x_N < 7$ at. %, H_c decreases with increasing nitrogen

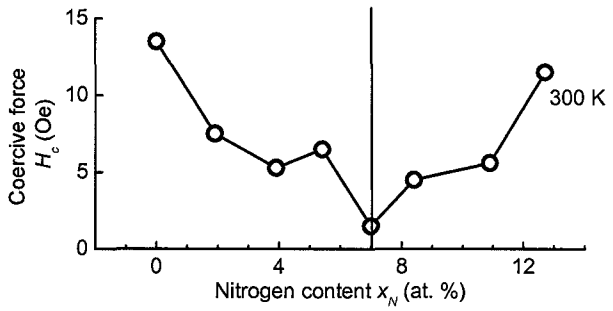

FIG. 4.2.5. Variation of the coercive force H_c with nitrogen content at room temperature.

content, while for $x_N \geq 7$ at. %, it increases. A similar trend in the coercive force in the Fe-X-N films was also observed by other workers. (Chezan 2002) (Ding and C. Alexander 2005) It was found that this trend is consistent for different temperatures (Das *et al.* 2006). There is a definite kink in the coercive force values at $x_N \approx 7$ at.%. This variation of coercive force with x_N can be understood by considering two factors. (1) The effect of grain size and (2) the effect of the competition between the cubic and uniaxial anisotropy in the Fe-Ti-N films.

The grain size in nanocrystalline materials has a significant effect on the coercive force. In these materials, when the grain size is smaller than exchange length, the variation in magnetocrystalline anisotropy axes is efficiently averaged out. This results in very low values of the coercive force. In the Fe-Ti-N films, for low nitrogen concentrations i.e. $x_N < 7$ at. %, where the grain size varies from 28 nm to about 10 nm, H_c increases almost linearly with the grain size. For $x_N \geq 7$, the grain size is in the 4 - 10 nm range and the coercive force decreases with increasing grain size.

The competition between cubic and uniaxial anisotropy also has an effect on the coercive force. The data on remanence show that the cubic anisotropy dominates for $x_N < 7$ at. % and for $x_N \geq 7$ at. %, the nitrogen-induced uniaxial anisotropy takes over the cubic anisotropy. Cubic anisotropy decreases with increasing nitrogen content for $x_N < 7$ at. % (Ding and C. Alexander 2002) and as can be seen from the FMR results, the nitrogen-induced uniaxial anisotropy increases linearly with nitrogen content. Therefore, for the low concentrations of nitrogen, the coercive force decreases following the decrease in the cubic anisotropy, while the linear increase in uniaxial anisotropy is responsible for the increase in H_c for the higher nitrogen content films (Das *et al.* 2006).

Calculation of the cubic and uniaxial anisotropy constants.

The effective anisotropy constants were calculated from the hysteresis loop and microwave data. Néel's prediction (Néel 1947) for the coercive force for randomly oriented cubic nanoparticles can be written as

$$H_c = 0.64 < K_1 > / M_s . \qquad (4.1.14)$$

Here $< K_1 >$ is the effective cubic anisotropy constant. For the Fe-Ti film, the value of $< K_1 >$ is about 3.3×10^4 erg/cm^3 at room temperature. This value is about one order of magnitude lower than the single-grain anisotropy constant K_1 – value of Fe (Chikazumi 1997). Herzer has suggested that for randomly oriented nanoparticles where the grains interact through an exchange coupling, the effective anisotropy

constant the average value of the anisotropy constant $< K_1 >$ is expected to be lower than the K_1 – value (Herzer 1990).

In order to obtain a quantitative understanding of the variation of H_c with nitrogen content, the effective cubic and uniaxial anisotropy constants i.e. $< K_1 >$ and $< K_u >$ respectively, were calculated using the hysteresis loop and microwave data for various nitrogen content films. The results are shown in Fig 4.2.6. The $< K_1 >$ values for $x_N < 7$ at. % were calculated using the Eq. (4.2.2). For $x_N \geq 7$ at. % films, uniaxial anisotropy is dominant. In such a case, the coercive force is related to the effective uniaxial anisotropy constant $< K_u >$ by the expression (Gangopadhyay *et al.* 1992)

$$H_c = 0.96 < K_u > / M_s . \qquad (4.1.15)$$

Again, it can be seen in Fig 4.2.6 that the cubic anisotropy parameter decreases with an increase in the nitrogen content while the uniaxial anisotropy parameter increases.

Summarizing the static magnetization results, the changes which appear at $x_N \approx$ of 7 at.% are related to the structure of the Fe-Ti-N system. Addition of Ti to the body centered cubic (bcc) α – Fe lattice results in Ti occupying the Fe sites and an increase in the lattice volume. However, the lattice structure still remains bcc. Recent experiments show that about 3 at. % Ti at the Fe site increases the lattice parameter from 2.866 Å to 2.878 Å.(Ding and C. Alexander 2006)

Therefore, in the Fe-Ti-N system, the effect of nitrogen atom on the lattice structure may differ from that observed in other Fe-N systems. The nitrogen can be infused in the bcc $\alpha-$Fe lattice up to about 0.4 at % without causing any distortion in the lattice structure (Mijiritskii and Boerma 2001). Above this concentration, however, the nitrogen atom starts distorting the lattice structure resulting an increase in the c/a ratio. This changes the phase to an α' phase, where the nitrogen randomly occupies the octahedral interstitial sites. Larger concentration of nitrogen leads to yet another phase change viz. α'' phase, which is body-centered-tetragonal (bct) in structure (Jack 1994) and the nitrogen atoms have an ordered arrangement in the lattice. The Fe-N phase diagram shows that addition of more nitrogen gives the γ phase, which has a face-centered-cubic (fcc) structure and the nitrogen atoms are perfectly ordered at the octahedral sites (Jack 1994). For $x_N \leq 10$ at. %, the c/a ratio and the lattice volume increase linearly with nitrogen concentration (Jack

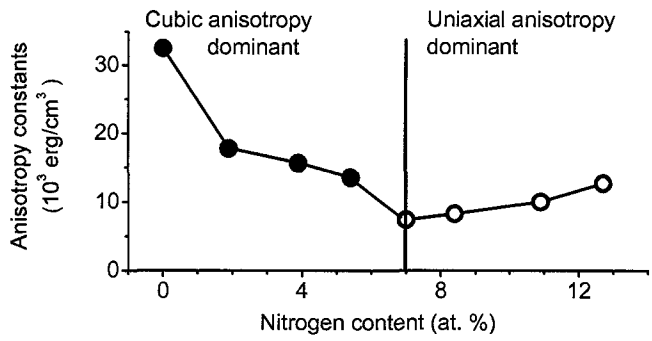

FIG. 4.2.6 Anisotropy constants as a function of nitrogen content. The solid circles indicate the values obtained from the coercive force data and the open circles indicate the values obtained from the anisotropy field parameter from the FMR measurements.

1951).

The remanance results show a change in the anisotropy from cubic to uniaxial at $x_N \approx$ 7 at. % where the M_r / M_s ratio goes from nearly 0.8 down to 0.5. The trend shown in coercive force reinforces the effect of decreasing grain size and the cubic-uniaxial anisotropy competition.

4.2.3 FERROMAGNETIC RESONANCE RESPONSE

Ferromagnetic resonance response was measured for all the films with the applied field in the plane of the film. To estimate the induced uniaxial anisotropy, FMR profiles were obtained for different orientations of the external field in steps of 5 degrees. Frequency dependence of linewidth was measured by the use of the strip transmission line method from 3-6 GHz and by the use of a shorted waveguide method in the 8-40 GHz range. Field modulation and lock-in detection methods were used to detect the FMR signal. The raw data consisted of the field derivative of the FMR absorption. These profiles were fairly symmetric indicating that the corresponding FMR absorption profiles were Lorentzian in shape. The FMR resonance positions were obtained from the zero crossing position in field of the derivative profiles. The FMR linewidths ΔH_d were obtained as the difference in field points of the extrema of the derivative profiles. These values may be converted to ΔH values using Eq. 2.63.

Induced uniaxial anisotropy

A distribution of nitrogen atoms at interstitial sites in the Fe-Ti structure gives rise to in plane uniaxial anisotropy in the field deposited Fe-Ti-N films. The direction of the anisotropy field depends on the direction of the static field applied during deposition. For the films investigated in this study, the applied field was directed in the plane of the films. Ferromagnetic resonance position measurements as a function of in plane angle θ of the applied field H to the easy axis yielded a measure of the anisotropy field parameter H_A. In the limit of high saturation induction $4\pi M_s$ for these films, the resonance frequency ω_0 is given by

$$\omega_0 = |\gamma| \sqrt{\left(H + H_A \cos 2\theta \right) 4\pi M_s}, \qquad (4.1.16)$$

Ferromagnetic resonance results for all the samples showed a clear in plane uniaxial anisotropy for $x_N > 3.9$ at. %. The samples with nitrogen content $x_N \leq 3.9$ at. %, however, did not show an obvious angle dependence of the FMR resonance position.

Figure 4.2.7 shows representative FMR field data as a function of angle for the film with $x_N = 8.4$ at. %. The open circles are the data and the solid curve is the theoretical fit to the data with an H_A value of 12.5 Oe. The $4\pi M_s$ value was taken from the static magnetization measurements as mentioned earlier in the previous section. From the graph it is clear that the magnetization has a preferential easy and hard direction. For all the films with $x_N \geq 3.9$ at. %, the angle dependence of the resonance field can be attributed to a uniaxial type behaviour.

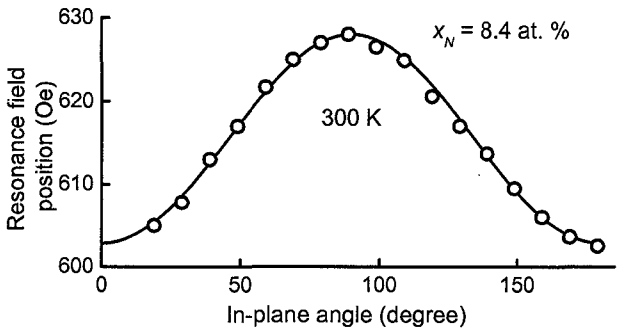

FIG. 4.2.7 Resonance field position as a function of the in plane angle with the easy axis at . The solid line is a fit to the data.

The anisotropy field parameter H_A for nitrogen concentrations $x_N \geq 3.9$ at. % was obtained from the uniaxial type response of the resonance field position vs. in-plane angle data. Figure 4.2.8 shows the H_A values obtained from the microwave measurements vs. nitrogen content. The uniaxial anisotropy is seen to increase with the nitrogen content with values going up to 19 Oe for $x_N = 12.7$ at. %. For comparison, the H_A values for Permalloy are on the order of 5 Oe.

The distortion in the bcc lattice in the $x_N < 7$ at. % range results in a decrease in the cubic anisotropy.(Ding and C. Alexander 2002) Further, the structural change from bcc to bct at about $x_N = 7$ at. % minimizes the cubic anisotropy. At the same time, the occupation of the nitrogen atoms at interstitial sites gives rise to a uniaxial anisotropy in the field deposited Fe-Ti-N films (Riet *et al.* 1997). Hence an increase in the nitrogen content in the films also reflects in an increase in the uniaxial anisotropy. The direction of the anisotropy field depends on the direction of the field during deposition, which was in the plane of the films in this study.

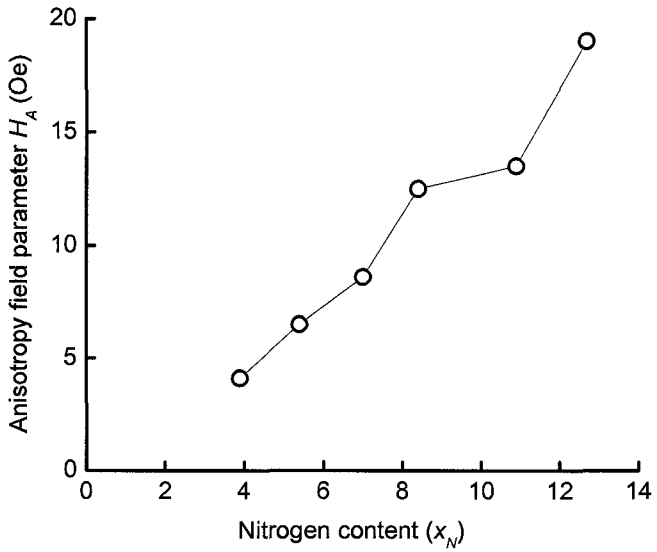

FIG. 4.2.8 Anisotropy field parameter as a function of nitrogen content.

FMR linewidth for various nitrogen content as a function of frequency and temperature

Figure 4.2.9 shows the peak to peak FMR linewidth vs. x_N for different frequencies and different temperatures. Graph (a) shows the linewidth vs. x_N for a fixed frequency of 9.5 GHz at temperatures of 294 and 95 K as indicated. Graph (b) shows the room temperature linewidth vs. x_N for frequencies of 3.5 and 5 GHz, as indicated. The linewidth decreases as a function of x_N, for values of x_N less than 7%. However, beyond 7% the linewidth stays more or less constant. This trend of a sharp decrease in linewidth as the x_N approaches 7 at.% and then the constancy of linewidth was observed at 9.5 GHz for various temperatures. As graph (a) clearly shows, this trend is independent of temperature.

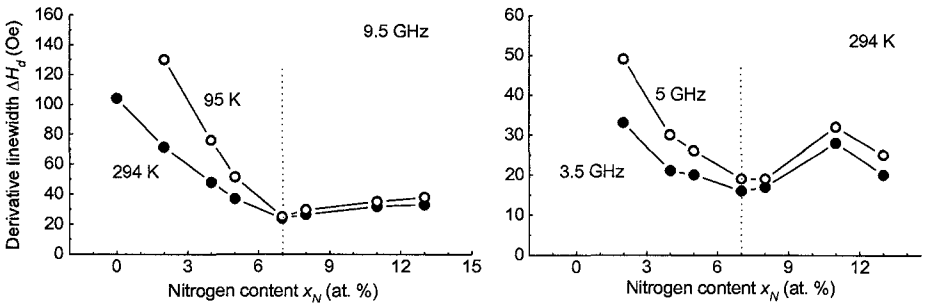

Fig. 4.2.9. FMR linewidth vs. nitrogen content at different temperatures and frequencies.

All of the FMR responses show clear minima at $x_N \approx 7$ at.%, which is the point at which the bcc to bct structural change occurs. As the nitrogen content in the films is increased the conductivity decreases. This decrease in conductivity is accompanied by a decrease in the linewidth. This is to be expected if the damping mechanism is magnon-conduction electron scattering. Also, as the nitrogen content is increased the grain size decreases. The arrest in further decrease in linewidth and its levelling off for $x_N \geq 7$ is probably due to additional large contribution due to grain boundary scattering.

Figure 4.2.10 shows the wide frequency range dependence of linewidth, for two samples, one with x_N value less than 7 at.% and the other larger than 7 at.%. The (a) graph shows the FMR data for sample with $x_N = 3.9$ at.%. The (b) graph shows the FMR data for the sample with $x_N = 8.4$ at. %. For samples with x_N values less than 7 at.%, the linearity of the ΔH_d values vs. frequency disappeared in the wider

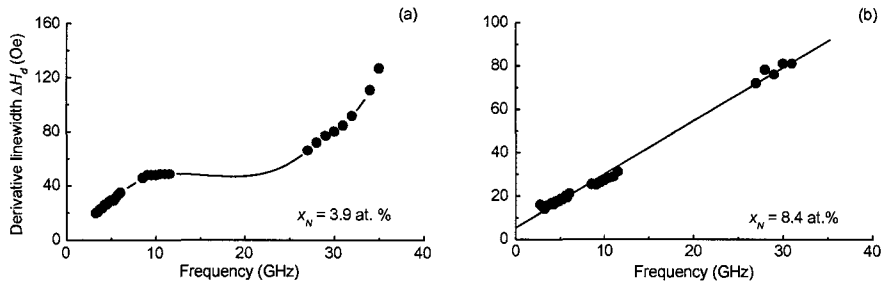

Fig. 4.2.10. FMR linewidth vs. frequency for x_N = 3.8 at.% and 8.4 at. %

bandwidth. For samples with x_N values larger than 7 at.%, the linewidth remained fairly linear with frequency.

It is clear from these graphs that the samples do not show the behaviour expected from metallic films. The $x_N = 3.9$ at.% sample shows a highly non-linear trend in frequency, with the linewidth increasing drastically above 25 GHz. These data were verified by independent linewidth measurements at the University of Alabama (Alexander 2005). In contrast, graph (b), for $x_N = 8.4$ at.%, shows a nearly linear $\Delta H(f)$ response.

Discussion of FMR results

The nonlinearity in the FMR linewidth vs. frequency response was evaluated with a combination of intrinsic damping, (ΔH_{LL}) a two magnon scattering contribution (ΔH_{TMS}) and a linebroadening due to ripple field (ΔH_{ripp}).

$$\Delta H = \Delta H_{LL} + \Delta H_{TMS} + \Delta H_{ripp} \qquad (4.1.17)$$

Intrinsic damping models like the Landau-Lifshitz or Gilbert models essentially give a linear dependence of linewidth on frequency. The slope of the line is related to the damping parameter α_{LL}. Two-magnon scattering can contribute to the linewidth due to inhomogeneities when the exchange and dipolar interactions are very strong. These inhomogeneities introduce weak interactions between the spin wave modes and provide a channel for the energy transfer from the uniform precession mode. McMichael and Krivosik have treated this phenomenon in a classical model (McMichael and Krivosik 2004) including grain size and anisotropy effects. It was shown that there is a large effect of grain size and anisotropy on the frequency dependence of FMR linewidth. The ripple field H_r contributes to the linebroadening when the exchange and dipolar interactions are stronger than the inhomogeneities. The methods of calculating the intrinsic linewidth, the two-magnon contribution to the linewidth and the effect of ripple on the linebroadening have been summarized in Chapter 2.

The two-magnon scattering calculation was based on Eqn. (2.79). If the two magnon scattering is due to variation of the anisotropy, the strength of the scattering $\langle \delta h^2(\mathbf{r}) \rangle$ would be given by: (McMichael and Krivosik 2004)

$$\langle \delta h^2(\mathbf{r}) \rangle \propto \left(\frac{2K}{M_s} \right)^2 \tag{4.1.18}$$

The ripple field contribution was based on Eqn. (2.86).

Figure 4.2.11 shows the FMR linewidth vs. frequency for six samples in the frequency range of 2-14 GHz. The open circles show the data while the solid curves

are the calculations. These calculations include LL type of damping and two types of inhomogeneity scattering namely, two-magnon and line broadening due to ripple fields.

There is a fairly good agreement between the data and the calculations. The value of α_{LL} was 0.005 for all the samples. This value compares well with that obtained for low linewidth Permalloy films. The two magnon correlation parameter $\langle \delta h^2 \rangle$ and the ripple field strength H_{ripp} were the fit parameters and these varied with the nitrogen content.

Figure 4.2.12 shows the values of the anisotropy field parameter used for the two magnon scattering fits $\sqrt{<\delta h^2>}$ and compares it to the anisotropy field parameter $2<K>/M_S$ values obtained from the static magnetization measurements. The right axis and the solid circles show the $\sqrt{<\delta h^2>}$ values, while the left axis and the solid triangles show the $2<K>/M_S$ data.

The general trend for the anisotropy field parameter $\sqrt{<\delta h^2>}$ obtained from the fits follow the same trend as the measured $2<K>/M_S$ values. This implies that at in these films, two-magnon scattering due to the random anisotropy orientation in the grains is a dominant loss mechanism. For $x_N \geq 7$ at. %, the $\sqrt{<\delta h^2>}$ value is close to zero. The actual $2<K>/M_S$ values are a factor of 10 lower than the two magnon scattering field values. This is a reflection of the fact that the $<K>$ values,

especially for the Fe-Ti sample, are much (actually an order of magnitude) smaller than the literature values, as mentioned previously.

Figure 4.2.13 shows the ripple field strength H_r obtained from the calculations. The data in the figure shows that the ripple field broadening is considerable for $x_N < 7$ at. %. However the values decrease with the increase in x_N. For $x_N > 7$ at. %, the values of H_r are of the magnitude as the uniaxial anisotropy field.

It is important to note that the data for $x_N = 3.4$ at. % at higher frequencies could not be modelled by these theories. The connection between the grain size, the structural transition, and the FMR linewidth frequency dependence is extremely

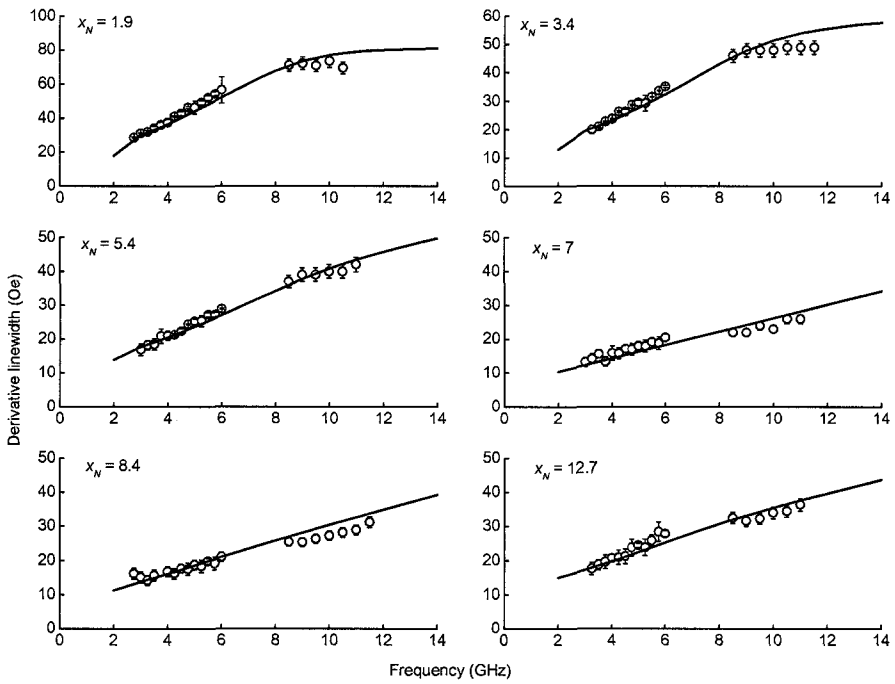

Fig. 4.2.11. FMR linewidth vs. frequency with the fits to the data with LL type of damping, two magnon scattering, and ripple field line broadening.

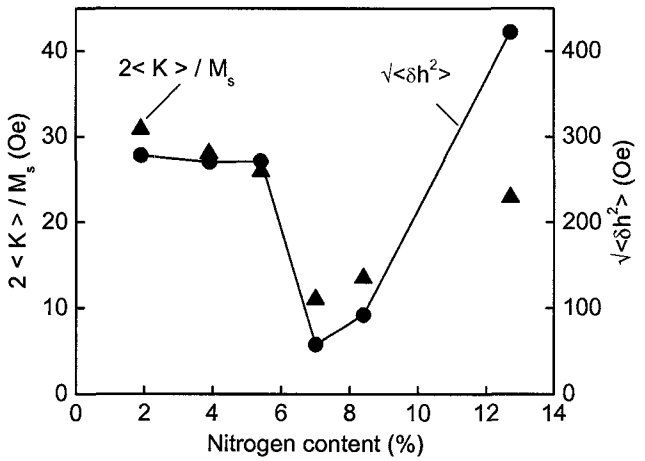

FIG. 4.2.12 The strength of two magnon scattering (solid circles) from the fits and the measured $2 < K > / M_S$ (solid triangles) as a function of nitrogen content x_N.

complex. This unusual behaviour in the static and dynamic regime indicates that perhaps the structural transition has a more significant effect on the microwave loss than is expected.

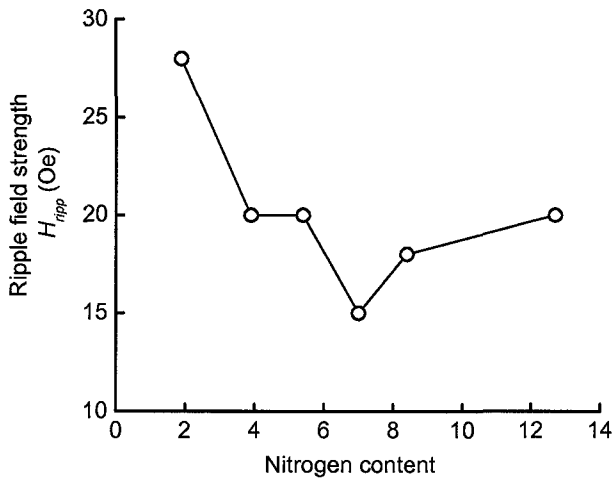

FIG. 4.2.13 Ripple field strength as a function of nitrogen content x_N.

4.2.4 SUMMARY AND CONCLUSIONS

The effect of nitrogenation of Fe-Ti alloy thin films and its effect on static and microwave magnetic properties has been studied. A distinct dependence of coercive force, FMR linewidth, and the intrinsic damping parameter on the nitrogen content has been observed. All these parameters appear to follow a trend in the structural transition from bcc to bct. The saturation induction was found to decrease with increasing nitrogen content. The nitrogen atom goes to the interstitial sites of the metallic lattice. This can be correlated to a fast expansion in the lattice volume due to inclusion of the nitrogen atom in the $x_N < 7$ at. % range. However, above this range of nitrogen content, data indicate a probable structural transition from the body-centered-cubic to the body-centered-tetragonal structure. The variation in the coercive force with nitrogen concentration also indicates a structural change at about 7 at. % nitrogen content.

The nitrogen atoms induce uniaxial anisotropy in the system. The ratio of the remanence to the saturation induction clearly shows that there is a competition between the cubic and uniaxial anisotropy in these Fe-Ti-N films. For lower nitrogen content films, the magnetocrystalline cubic anisotropy dominates and the decrease in the coercive force follows from the decrease in the cubic anisotropy with increasing nitrogen content. For $x_N \geq 7$ at. %, the coercivity increases with the induced anisotropy and the nitrogen-induced uniaxial anisotropy is dominant.

Ferromagnetic resonance results point to a relation between the structural transition and the microwave loss. The intrinsic damping parameters for all these films are on the order of 0.005. This is typical of low loss metallic films like Permalloy.

The extrinsic contribution to linewidth can be inferred as arising from two magnon scattering due to random anisotropy in the grains. There is a definite minimum in the two magnon contribution to the FMR linewidth at $x_N = 7$ at.%. There is also a levelling off of the contribution to linewidth due to inhomogeneous fields at this point. This is also the value of nitrogen content at which the bcc to bct structural transition takes place and a transition of the type of anisotropy dominance from cubic to uniaxial. The frequency dependence of FMR linewidth hence shows a dependence on the anisotropy, grains and hence, on the bcc to bct structural transition.

SPECIAL ACKNOWLEDGEMENTS

The author would like to acknowledge Professor C. Alexander for providing the films, and the measurements of nitrogen content, and grain size. The author would also like to acknowledge Dr. J. Das, for the static magnetic measurement data Dr. K. S. Kim for the 9.5 GHz data and Dr. P. Krivosik for help with the analysis.

4.3 REFERENCES

(Alexander *et al.* 2000) C. Alexander, J. Rantschler, T. Silva and P. Kabos J. Appl. Phys **87**(9): 6633-6635 (2000).

(Alexander, 2005) Private communication (2005).

(Anderson, *et al.* 1971) J. Anderson, S. Bhagat, and F. Chen, Phys. Stat. Sol. **45**, 312.(1971)

(Bertaud and Pascard, 1965) A. J. Bertaud, and H., J. Pascard, Appl Phys **36,** 970.(1965)

(Bonin *et al.* 2005) R. Bonin, M. L., Schneider, T. J. Silva, and J. P. Nibarger, J. Appl Phys **98**, 123904.(2005)

(Celinski and Heinrich, 1991) Z. Celinski, and B. Heinrich, J. Appl. Phys. **70**, 5935.(1991)

(Chezan, A. R. 2002) *Nanostructure and soft magnetic properties of iron-nitrogen alloys*, University of Groningen, The Netherlands. Ph. D. (2002).

(Chikazumi 1997) S. Chikazumi, *Physics of ferromagnetism*. NY, (Oxford University Press, 1997)

(Cochran, *et al.* 1982) J. F. Cochran, K. Myrtle, and B. Heinrich, J. Appl Phys **53**, 1982.(1982)

(Craus, *et al.* 2002) C. Craus, A. Chezan, M. Siekman, J. Lodder, D. Boerma and L. Niesen J. Mag. Mag. Mater **240**(1-3): 423-426 (2002).

(Craus, *et al.* 2004) C. Craus, A. Chezan, D. Boerma and L. Niesen J. Phys. - Cond Mat **16**(50): 9227-9241 (2004).

(Das *et al.* 2006) J. Das, S. S. Kalarickal, K. S. Kim, and C. E. Patton Phys. Rev B (to be submitted).

(Ding and Alexander 2002) Y. Ding and J. C. Alexander J. Appl. Phys. **91**: 7833 (2002).

(Ding and Alexander 2005) Private communication (2005).

(Ding and Alexander 2006) Y. Ding and J. C. Alexander IEEE Trans. Magn. **42**, 5 (2006).

(Ding *et al.* 2001) Y. Ding, S. C. Byeon and J. C. Alexander IEEE Trans. Magn. **37**, 1776 (2001).

(Frait and Fraitova, 1980) Z. Frait, and D. J. Fraitova, J. Mag. Mag. Mater **15-18**, 1081.(1980)

(Gangopadhyay *et al.* 1992) S. Gangopadhyay, G. C. Hadjipanayis, B. Dale, C. M. Sorensen, K. J. Klabunde, V. Papaefthymiou, and A. Kostikas, Phys. Rev. B **45**, 9778 (1992).

(Geshev *et al.* 1998) J. Geshev, A. D. C. Viegas and J. E. Schmidt J. Appl Phys **84,** 1488 (1998).

(Heinrich *et al.* 1985) B. Heinrich, J. F. Cochran, and Hasegawa, J. Appl Phys **57**, 3690.(1985)

(Heinrich, 2003) B. Heinrich, *Spin Relaxation in Magnetic Metallic Layers and Multilayers*. Springer Verlag (2003).

(Herzer, 1990) G. Herzer IEEE Trans. Magn. **26**, 1397 (1990).

(Hillebrands and Ounadjela, 2001) B. Hillebrands, and K. E. Ounadjela, *Spin Dynamics in Confined Magnetic Structures*, Springer, Berlin.(2001)

(Jack, 1951) K. H. Jack Proc. Roy. Soc. A **208**, 200 (1951).

(Jack, 1994) K. H. Jack J. Appl. Phys. **76**, 6620 (1994).

(Kalarickal *et al.* 2006) S. S. Kalarickal, P. Krivosik, M. Wu, C. E. Patton, M. L. Schneider, P. Kabos, T. J. Silva, and J. P. Nibarger, J. Appl Phys **99**(9), 093909 (2006).

(Kraus *et al.* 1981) L. Kraus, Z. Frait, and J. Schneider, Phys. Stat. Sol. **64**.(1981)

(Liu *et al.* 2003) X. Liu, J. Rantschler, C. Alexander, and G. Zangari, IEEE Trans. Magn. **39**(5), 2362-2364.(2003)

(McMichael and Krivosik 2000) R. McMichael and P. Krivosik IEEE Trans. Magn. **40** 2 (2004).

(McMichael et al. 2003) R. McMichael, D. Twisselmann and A. Kunz, Phys Rev Lett. 90, 2760 (2003).

(Mijiritskii and Boerma, 2001) A. V. Mijiritskii and D. O. Boerma Phys. Rev. B 64 035410 (2001).

(Néel, 1947) L. Néel C. R. Acad. Sci. (Paris) 224 1488 (1947).

(Patton et al. 1966) Patton, C. E., McGill, T. C. and Wilts, C. H., J. Appl Phys 37(9), 3594.(1966)

(Patton *et al.* 1975) Patton, C. E., Frait, Z. and Wilts, C. H., J. Appl. Phys **46**(11), 5002-5003.(1975)

(Patton, 1968) Patton, C. E., J. Appl. Phys **39**, 3060.(1968)

(Patton, 1973) C. E. Patton, *Angle and thickness dependence of the FMR linewidth in high quality Ni-Fe films*. AIP conference proceedings,**10**, 135 Denver (1972) (1973).

(Plummer and Weller, 2001) V. E. Plummer, and Weller, *The Physics of Ultra-High-Density Magnetic Recording*, Springer, Berlin.(2001)

(Quach, *et al.* 1976) H. Quach, A. Friedman, C. Wu, and A. Yelon, Phys. Rev. B **17**, 312.(1976)

(Rantschler and Alexander, 2003) J. Rantschler and C. Alexander J. Appl. Phys **93**(10): 6665-6667 (2003).

(Rantschler, 2003) J. Rantschler, *Ferromagnetic Resonance and Microsrtucture of Soft Magnetic Thin Films* University of Alabama Ph.D. Thesis.(2003)

(Riet *et al.* 1997) E. V. de. Riet, W. Klaassens and F. Roozeboom J. Appl. Phys. **81,** 806 (1997).

(Rossing, 1963) T. D. Rossing , J. Appl Phys **34**, 995.(1963)

(Schneider *et al.* 2005) M. L., Schneider, T. Gerrits, A. B. Kos, and T. J. Silva, Appl. Phys. Lett. **87**, 072509.(2005)

(Spano and Bhagat, 1981) M. L. Spano, and S. M. Bhagat, J. Mag. Mag. Mater **24**, 143.(1981)

(Stoner and Wohlfarth, 1948) E. C. Stoner and E. P. Wohlfarth Philos. Trans. R. Soc. London, Ser A **240,** 599 (1948).

(Sun *et al.* 2002) N. Sun, S. Wang, T. Silva and A. Kos IEEE Trans. Magn. **38**(1), 146-150 (2002).

(Twisselmann and McMichael, 2003) D. Twisselmann, and R. McMichael, J. Appl. Phys **93**(10), 6903-6905.(2003)

(Viala *et al.* 1996) B. Viala, M. K. Minor and J. A. Barnard IEEE Trans. Magnetics **32**(5), 3506 (1996).

(Viala *et al.* 1996) B. Viala, M. K. Minor and J. A. Barnard J. Appl. Phys **7**, 3941 (1996).

(Yoshizawa, *et al.* 1988) Y. Yoshizawa, S. Oguma and K. Yamaguchi J. Appl Phys **64**, 6044 (1988).

EXPERIMENTAL RESULTS II – FERROMAGNETIC RESONANCE LINEWIDTH IN CERAMICS

Outline:

5.1: Frequency dependence of linewidth in hot isostatic pressed yttrium iron garnet

5.1.1: Material details

5.1.2: Frequency dependence of FMR linewidth

5.1.3: Summary

5.2: Microwave magnetic properties of ferrite ferroelectric composite materials

5.2.1: Materials details and crystallographic analysis

5.2.2: Static magnetic properties

5.2.3: Ferromagnetic resonance response

5.2.4: High field effective linewidth results

5.2.5: Summary and conclusions

5.3: References

Ferromagnetic resonance in non-metallic materials is a well studied area. However there still remain topics for study related to the characterization of new materials and/or materials prepared by new fabrication procedures. This chapter concentrates on the ferromagnetic resonance studies in highly dense polycrystalline yttrium iron garnet (YIG) prepared by hot isostatic pressing (hipping), and new ferrite-ferroelectric composite materials intended for multifunctional applications.

Section 5.1 and its subsections describe the FMR results obtained for highly dense bulk pure and substituted YIG. Section 5.2 and its subsections present an initial study of ferrite-ferroelectric composite materials.

5.1 FREQUENCY DEPENDENCE OF LINEWIDTH IN HOT ISOSTATIC PRESSED YTTRIUM IRON GARNET

"*One may say that YIG is .. to ferromagnetic resonance research what the fruit fly is to genetics research*" (Sparks *et al.* 1961)

Ferromagnetic resonance (FMR) losses in polycrystalline ferrites depend on various factors. The dominant loss mechanism for typical coarse-grain ferrites with a low magnetocrystalline anisotropy and a small porosity is two-magnon scattering. Two main sources of this scattering are (1) a variation of the anisotropy due to randomly oriented crystalline grains and (2) dipole field due to pores. The anisotropy loss mechanisms were first treated theoretically by Schloemann in his

theory developed for two-magnon anisotropy dominated scattering (TMAS). (Schlomann 1956), (Schlomann 1958) However, experimental results show that it is extremely difficult to isolate the anisotropy effects from the residual porosity effects. (Kaskatkina *et al.* 1983) (Patton 1969), (Patton 1975), (Roschmann 1975), (Seiden and Grunberg 1963) This is because completely eliminating porosity is a difficult fabrication problem. Two established processes to make dense ferrites are hot pressing (Patton 1970) and hot isostatic pressing (hipping) (Atkinson and Davies 2000), (Van Hook and Willingham 1984) Hot isostatic pressing have yielded YIG materials with the lowest porosity till date. (Nazarov *et al.* 2003) This provided an excellent test bed for Schloemann's TMAS theory which has not been experimentally verified by direct frequency dependence of FMR linewidth measurements until now.

This work concentrates on the low frequency FMR measurements on highly dense YIG samples made by hipping. The linewidth results as a function of frequency closely match the predictions made by Schloemann's TMAS theory. Section 5.1.1 describes briefly, the hipping process and the sample preparation. Section 5.1.2 presents the experimental results on hipped YIG and hipped substituted YIG samples and also shows results on some porous YIG samples. Section 5.1.3 gives a summary of the work presented in Section 5.1.

5.1.1 MATERIAL DETAILS

The YIG samples used in this work were made by hipping. Nazarov et *al.* have elaborated the fabrication of, and the X-band microwave FMR and high power losses

in these materials. (Nazarov *et al.* 2003) The sample preparation described by Nazarov *et al.* is summarized below.

The starting material was a conventionally sintered polycrystalline YIG material obtained from Pacific Ceramics, Inc., which was prepared from yttrium iron oxide powders with a rare earth impurity content below 0.01%. The residual porosity was less than 1% and the half power FMR linewidth was 27 Oe at 10 GHz. Small blocks of these materials were then subjected to a hipping process in an argon atmosphere. The starting argon pressure in the chamber was 470 bar. The temperature and pressure were gradually increased to 1400 °C and 1000 bar respectively over 10 hours and then held at this soak point for 3 hours. The system was then cooled and vented back to room temperature and pressure over 20 hours. The measured density of the hipped YIG material was 5.172 g/cm^3, which is the theoretical density for YIG. The average grain size was 8 μm. Spheres were fabricated from the interior regions of the hipped blocks, to avoid possible problems with oxygen deficient surface regions. The same procedure was also applied to Ca-V-substituted YIG. The specific results in this chapter, shown for 2 mm diameter spheres, confirm the nearly complete elimination of porosity for the hipped materials.

5.1.2 FREQUENCY DEPENDENCE OF FMR LINEWIDTH

The frequency dependence of linewidth between 1.95 and 6 GHz was measured using the stripline FMR (SL-FMR) spectrometer. The details of the experimental setup are given in Chapter 3. The sample under consideration was a polished 2mm hipped YIG sphere. Careful polishing was extremely important to eliminate two-

magnon scattering due to surface pits. The absorbed power was seen to be a small perturbation, which meant that the small sample size and the wide center conductor ensured that the microwave magnetic field in the sample was homogenous. This is essential since it ensures that only the uniform mode is excited.

Figure 5.1.1 shows the derivative of the absorbed power profiles as a function of static field for the hipped YIG sphere, at the indicated frequencies in GHz. The profiles are fairly symmetric and correspond to Lorentzian absorption profiles. The resonance field position was taken from the zero crossing of the derivation of

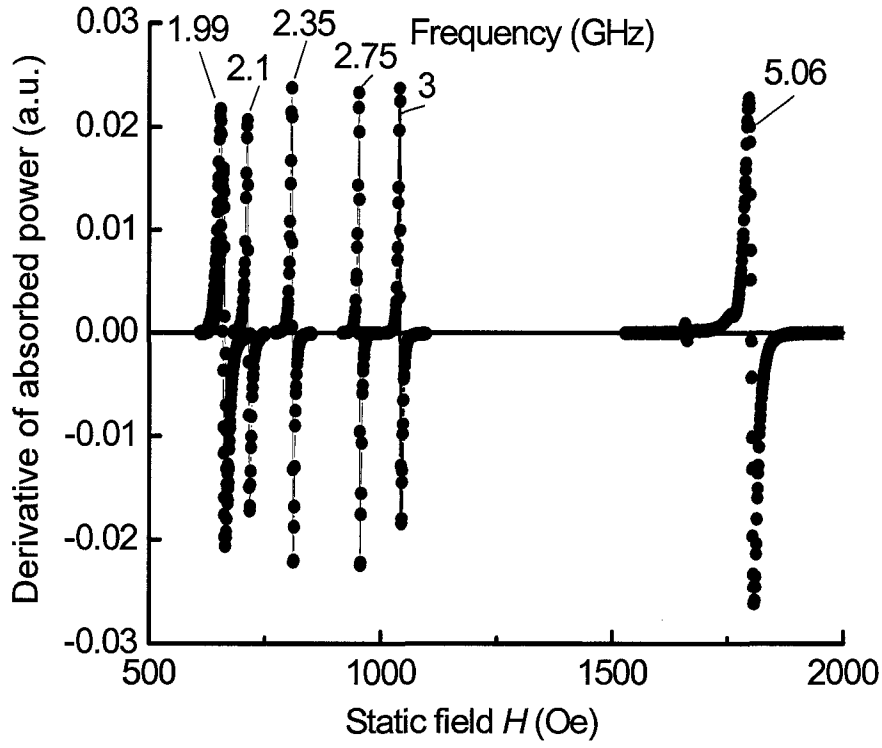

FIG. 5.1.1 Derivative of absorbed power profiles as a function of static field for Hipped YIG samples at indicated frequencies.

absorption curve. This field increases linearly with frequency as expected for a spherical sample. The half power field linewidth ΔH was calculated from the difference in field values at the extrema of the derivative profile with the use of Eq. (2.63). Figures 5.1.2 and 5.1.3. show the frequency dependence of the field swept linewidth ΔH for hipped pure YIG and doped YIG sample respectively. The strongly nonlinear $\Delta H(\omega)$ dependence is an indication of the dominant two-magnon scattering relaxation mechanism. This behavior is expected from the Schloemann two-magnon anisotropy scattering (TMAS) theory (Schlömann 1958) as elucidated in Chapter 2.

Figure 5.1.2 shows the half power FMR linewidth results on pure hipped YIG as a function of frequency. The solid circles are the data obtained with the SL-FMR technique. The open circles are Nazarov *et al.* data taken at 9.53, 14, 16 and 18 GHz, using a shorted waveguide technique. (Nazarov *et al.* 2003) The solid curve shows the field linewidth computed from Eq. (2.72) based on the Schloemann TMAS theory. The parameters used for the calculation were $4\pi M_S = 2045\,\mathrm{G}$, $H_A = 44\,\mathrm{Oe}$ and $|\gamma| = 2.81\,\mathrm{MHz/Oe}$.

One can see that the data match the theory extremely well. Three different regions in the frequency regime can be considered. These relate to Fig. 2.6, and the discussion thereafter, in Chapter 2. Note that graphs in Fig 2.6. were calculated for slightly different material parameters and therefore the frequency values do not match those discussed below.

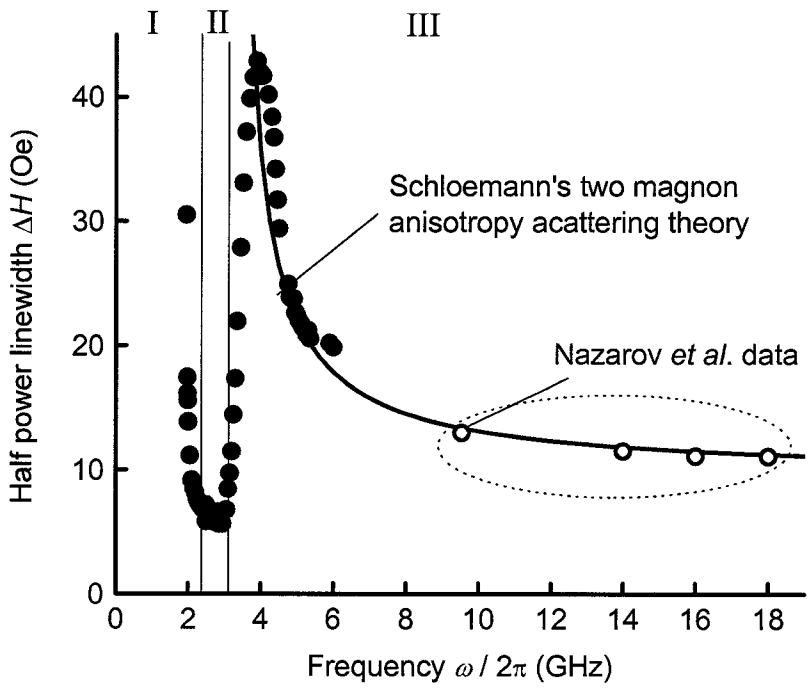

FIG. 5.1.2 Half power ferromagnetic resonance linewidth as a function of frequency for the 2 mm diameter hipped YIG sphere. The solid circles show the data obtained by the stripline spectrometer. The open circles show Nazarov *et al.* data, (Nazarov *et al.* 2003). The solid line shows the calculated linewidth from Eq. (2.72) for two magnon scattering process with parameters $4\pi M_s = 2045$ G, $H_A = 44$ Oe, $|\gamma| = 2.81$ MHz/Oe.

Region I corresponds to frequency $\omega < \omega_M / 3$ (~ 2.3 GHz) and to the situation shown in Fig 2.6(a). In this regime, the sample is not saturated and the FMR line is extensively broadened by the domain structure. In region II, $\omega_M / 3 < \omega < 2\omega_M / 3$ (2.3 GHz ~ 4.6 GHz), the uniform precession is above the manifold and the scattering takes place only to high k states. This region corresponds to graph (b) in Fig. (2.6). The coupling of the uniform mode to high k is weak in garnets and therefore the linewidth is small and almost a constant. In region III, as the frequency

is raised above the critical frequency, the uniform magnetization mode becomes quickly degenerate with the low and medium k states. The interaction is very strong in garnets and the linewidth increases abruptly. At $\omega = 2\omega_M / 3$ (~ 4.6 GHz), the uniform mode is excited at the upper limit of the spin wave manifold as shown in Fig 2.6.(c) and there is a maximum number of spin waves degenerate with the uniform mode. The maximum in the $\Delta H(\omega)$ dependence at this frequency reflects the maximum density of states of degenerate modes. As the frequency is raised further, the uniform mode moves into the manifold and the density of states for available degenerate modes decrease. This regime is shown in Fig. 2.6(d)-(f)

Figure 5.1.3 shows the half power FMR linewidth as a function of frequency for a hipped Ca-V-substituted YIG sphere for a frequency range of 1-6.5 GHz. The solid circles are the data obtained using the SL-FMR spectrometer. The solid curve is the calculated linewidth from Eq. (2.72) for the two magnon anisotropy scattering process with a $4\pi M_s$ value of 995 G, an H_A parameter of 27 Oe, $|\gamma|$ value of 2.68 GHz/kOe, and no porosity contribution.

Ca-V substitution in YIG results in a reduction in the anisotropy and hence a reduction in the linewidth. (Van Hook *et al.* 1968), (Patton and Van Hook 1972). The substitution also comes with a cost to the saturation magnetization, which is reduced to about 1000 G for these materials. The frequency dependence of the linewidth in hipped samples of YIG with Ca-V substitution follows closely the TMAS calculation. The only variable parameter used for the fit was the anisotropy

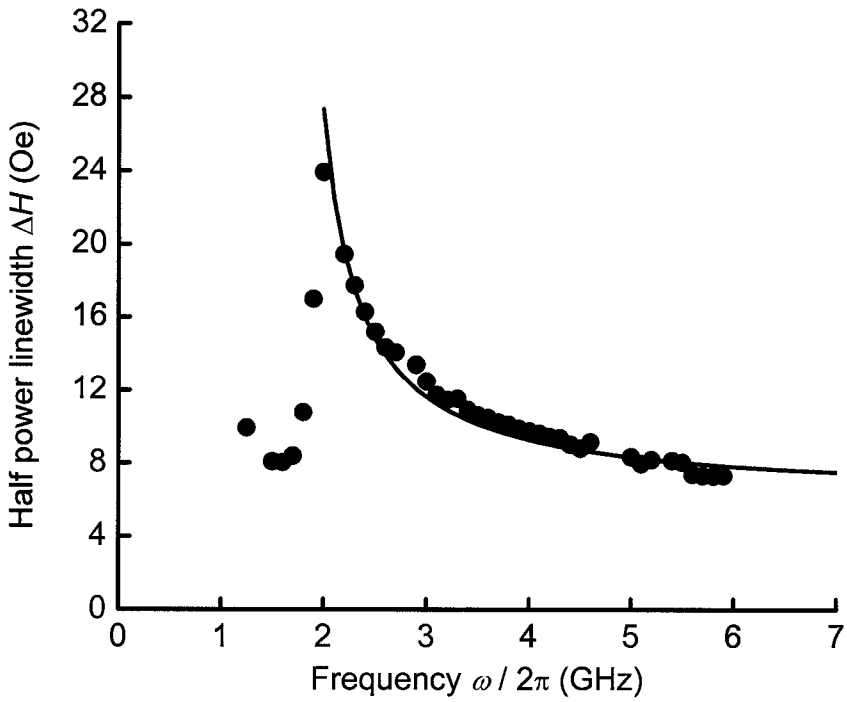

FIG. 5.1.3 Half power ferromagnetic resonance linewidth as a function of frequency for a hipped CaV-YIG 2 mm diameter sphere. The solid circles show the data The solid curve shows the calculated linewidth from Eq. (2.72) for two magnon scattering process with parameters $4\pi M_S = 995\,\mathrm{G}$, $H_A = 27\,\mathrm{Oe}$, $|\gamma| = 2.68\,\mathrm{MHz/Oe}$.

parameter H_A. The value of H_A used is close to the value of about 37 Oe obtained in previous works on single crystal Ca-V substituted YIG. (Patton 1969), (Patton and Van Hook 1972)

5.1.3 SUMMARY AND CONCLUSIONS

Ferromagnetic resonance linewidth results in the low microwave frequency regime for the first time experimentally confirm the two-magnon anisotropy scattering mechanism in polycrystalline ferrites. This evidence in hipped YIG comes from a peak in the linewidth at about 4 GHz. This peak corresponds to the frequency at

which the FMR frequency moves through the top of the spin wave band, and for which the density of states goes through a maximum. As the frequency is increased above 4 GHz, the linewidth decreases as the density of states decreases. The theory elucidated by Schloemann gives excellent quantitative agreement with the measured linewidth versus frequency results in the 1.95 – 18 GHz range.

--------- § ---------

5.2 MICROWAVE MAGNETIC PROPERTIES OF FERRITE FERROELECTRIC COMPOSITE MATERIALS

Ferrites and ferroelectric materials are used in a large family of microwave and millimeter wave devices. Ferrite devices typically have high figures of merit, good bandwidths, low insertion loss, and frequency agility.(Valenzuela 1994) Current ferrite components, however, present two critical problems for advanced system applications: large size and high cost. Ferroelectric components, on the other hand, provide new solutions both in size and cost.(Sengupta and Sengupta 1997),(Abeles 1976) Size reduction arises from the large relative dielectric constants. These components are also tunable with the application of a modest voltage. The voltage tunability and the low cost are advantageous for many applications. On the other hand, the tunability of ferroelectric components is not as high as for ferrites. Recently there has been a demand for the integration of high performance, multifunction, smaller size, higher efficiency and lower cost, with microwave and

millimeter wave device applications. The premise is that when a ferromagnetic and a ferroelectric phase coexist in one material, novel properties can be expected due to coupling between spontaneous magnetization and electric polarization. For example, electric polarization could be induced by an external magnetic field, and magnetization could be adjusted by an external electric field. Such phenomena are referred to as arising from the magneto-electric effect. Such materials, which exhibit two or all of ferroelectricity, ferromagnetism and ferroelasticity properties, have been called mutiferroics. Multiferroics which exhibit simultaneous ferroelectric and magnetic ordering are very rare. (Hill and Filippetti 2002) However, it is difficult to synthesize a single material that satisfies all the requirements for multifunctional components. Hence there is a push to fabricate composite materials.

It is likely that ferrite-ferroelectric composites could be used to produce small size, low cost, and highly tunable elements for microwave applications. Because of the wide variety of possible applications, there has been considerable interest in composite materials. (Abeles *et al.* 1975) (Bergman 1978) (Bergman 1979) (Bergman 1981) (Grannan *et al.* 1981) (Aspnes 1982) (Grimes and Grimes 1991) (Bergman and Stroud 1992) (Kanai *et al.* 2001) (Qi *et al.* 2004) Previous work on multifunctional ferrite ferroelectric composite materials have emphasized static magnetization properties (Kanai *et al.* 2001) (Qi *et al.* 2004) and the complex permeability and permittivity. (Mantese *et al.* 1996)

The objective of this work was to prepare a series of ferrite-ferroelectric composite materials with a systematic variation in the ferrite loading, and examine the static

and high frequency magnetic properties of these materials. The magnetic component was a standard commercial nickel zinc spinel ferrite from Trans Tech, TT2-111. The ferroelectric component was specially prepared barium strontium titanate.

Section 5.2.1 describes the materials preparation and the X-ray diffraction (XRD) results. Section 5.2.2 presents room temperature magnetization vs. field data for all of the composites and considers these data in terms of a simple model of non-interacting magnetic particles in a nonmagnetic host. Section 5.2.3 presents ferromagnetic resonance (FMR) results. Section 5.2.4 extends the high frequency analysis to include the microwave response at magnetic fields well above the FMR resonance field. This response is used to determine the high field effective linewidth for the different loadings. Section 5.2.5 presents a summary and conclusions.

5.2.1 MATERIALS DETAILS AND CRYSTALLOGRAPHIC ANALYSIS

The composite materials consisted of thick disks of Parascan^{TM} tunable dielectric materials, nominally ferroelectric barium strontium titanate (BSTO), with different loadings of the NiZn ferrite (NZF). Different weight percentages of the TT2-111 NiZn ferrite powder (0.3 wt. %, 1 wt. %, 5 wt. %, 10 wt. %, 25 wt. %, and 50 wt. %) were mixed with powders of BSTO materials. In addition, pure TT2-111 ($L = 100$ wt.%) powder was independently processed and sintered. The mixtures were alumina ball-milled for 24 hours in ethanol. The slurry was then dried and sieved. For each loading, a set of samples was pressed into 1 inch diameter disks and sintered at various temperatures in the range of 1200-1450 C. Disk densities were

then measured. A sintering temperature of 760°C was determined to yield the highest overall density for the $L = 0$ wt. % pure BSTO material. Optimum density samples were used for all of the measurements reported below. Sample densities, as measured on the starting cubes for the sphere samples used for the magnetic measurements (see below), ranged from 4.20 g/cm^3 to 5.25 g/ cm^3. There was no apparent correlation between loading and density. The samples were made at Paratek Microwave Inc., Columbia, MD.

A full XRD analysis was done in order to check the phases in the fired materials. These measurements were made with a standard XRD system with an angular step size of 0.02 degrees. Figure 5.2.1 shows a collage of XRD intensity vs. angle 2θ scans for all the samples. The individual scans are identified by the nominal NZF loading values in wt. % for the different samples. In each scan, solid circles and solid squares serve as markers for the main BSTO and NZF diffraction peaks, respectively. The solid triangles mark the peaks that identify the additional Ti-O phase. For the 1 and 0.3 w. % samples, there are no resolved NZF peaks.

These XRD data show that the BSTO phase is maintained intact for all the loadings. The ferrite phase is also largely intact for ferrite loadings at 5 wt.% and above. The intact peaks for the ferrite phase imply that the sintering temperatures and preparation methods did not degrade the individual phases in the composite material. The third phase, which has been identified to be that of Ti-O, is non-magnetic and is an artifact of the preparation procedure. The effective loading of the ferrite L was deduced from the relative areas under the maximum peaks for the three

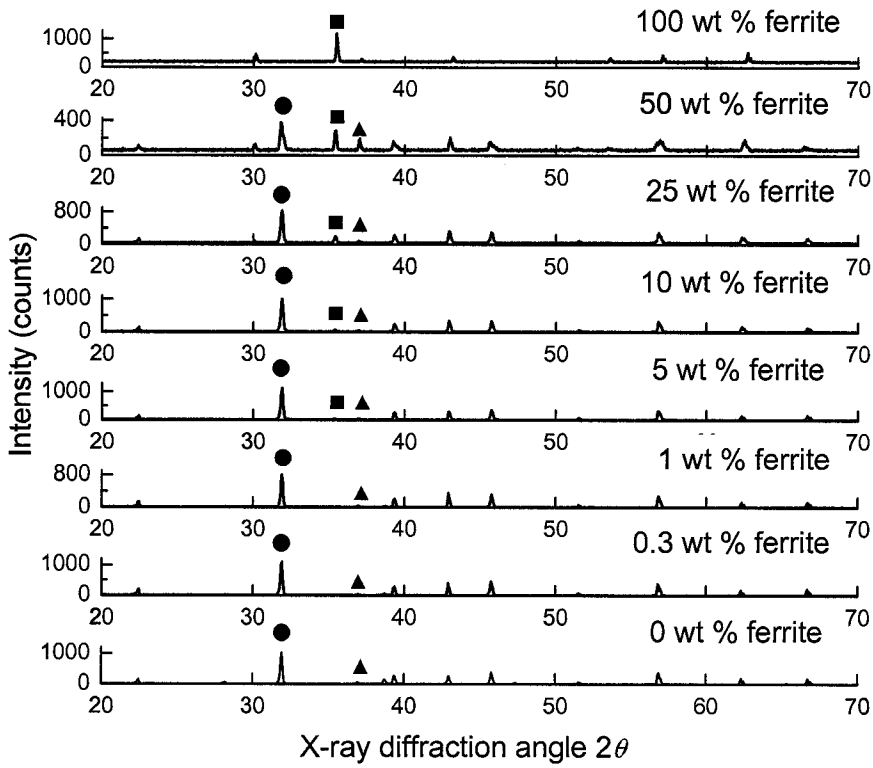

FIG.5.2.1. X-ray diffraction results for all the samples as indicated. The solid circles, squares and triangles indicate the main peaks for the BSTO, the ferrite phase, and the Ti-O phase.

phases present in the composite material. The loadings of 50, 25, 10 and 5 wt. % ferrite were found to actually be L = 27, 16, 6 and 4 % ferrite respectively.

Magnetic and microwave measurements were made on spherical samples with nominal diameters of 2 mm. For these measurements, spheres were fabricated from 3 mm cubes cut from the optimum density fired disks. The densities of the individual cubes and spheres were different from the densities measured on the starting disks, with about the same spread as indicated above. These variations in density may be taken as an indication of inhomogeneous starting disks. Two types of pure ferrite samples were also measured. First, the TT2-111 powders were used

to fire disks and then fabricate spheres at 100% ferrite loading based on the same procedures as given above. Second, fired TT2-111 blocks from Trans-Tech were used to fabricate sphere samples for baseline magnetic and microwave measurements.

5.2.2 STATIC MAGNETIZATION PROPERTIES

Static magnetic induction vs. field data were obtained by vibrating sample magnetometry at room temperature for applied fields up to 5 kOe. The data below are given in terms of the magnetic induction $4\pi M$. Volumes were calculated from the densities of the fired disks and the masses of the individual samples. Cubes and spheres gave similar results for all the loadings. The specific data below for the materials with partial ferrite loadings were obtained on spheres.

The various data on the average magnetic induction $\langle 4\pi M \rangle$ vs. applied magnetic field H, the average saturation magnetic induction $\langle 4\pi M \rangle_{\mathrm{SAT}}$, as measured at $H = 5\,\mathrm{kOe}$, vs. loading, and the saturation field H_{SAT}, initial susceptibility, and coercive force H_{C} vs. loading are shown in Figs. 5.2.2 – 5.2.4. Considered as a whole, these data show that the static magnetic response can be inferred from a model of an effective medium with unmodified ferrite inclusions in a non magnetic matrix.

Figure 5.2.2 shows full hysteresis loop data for the 4, 6, 15, 27 and 100 % loading samples. The main graph and the inset show average magnetic induction $\langle 4\pi M \rangle$ as a function of the applied magnetic field H. All samples show a clear saturation for fields above 1-2 kOe.

These hysteresis loop data show several effects. First, one can see that the measured $\langle 4\pi M \rangle_{\mathrm{SAT}}$ values at the 5 kOe field limit decrease as the loading L is

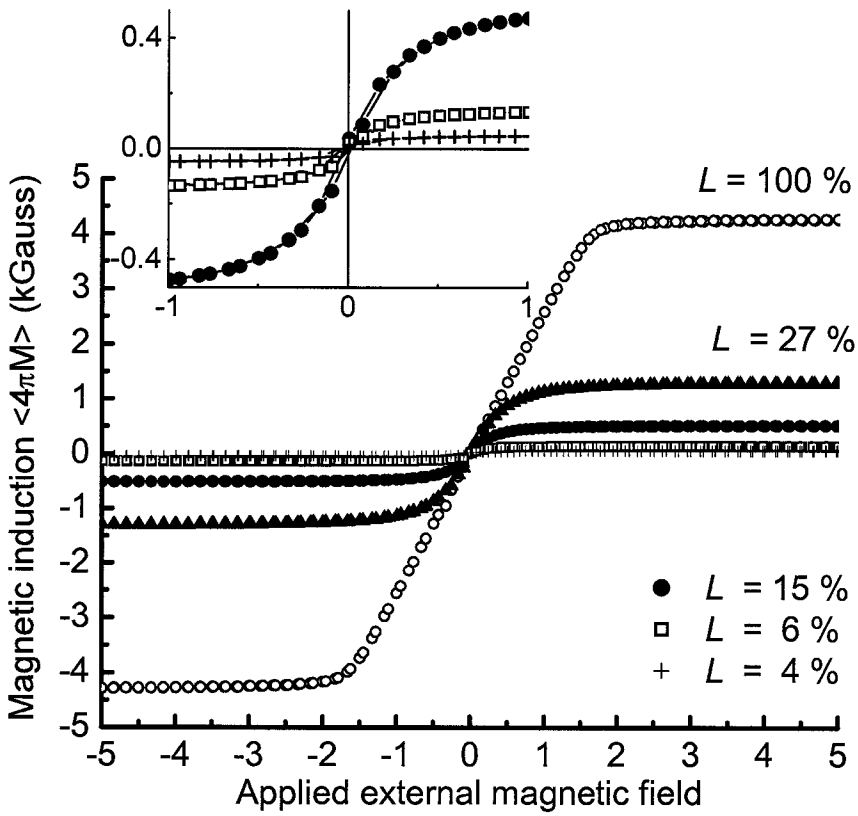

FIG 5.2.2. Average magnetic induction $\langle 4\pi M \rangle$ as a function of the applied magnetic field H for the different ferrite loadings, as indicated. The inset shows an enlarged view for samples with loadings of L =4, 6 and 15 %.

decreased. The $\langle 4\pi M \rangle_{SAT}$ value of 4.3 kG at $L = 100$ % is close to the $\langle 4\pi M \rangle_{SAT}$ value for the standard TT2-111 material. These $\langle 4\pi M \rangle_{SAT}$ data will be discussed in more detail shortly, in connection with Fig. 5.2.3

Second, from the outward shift in the knee of the full magnetization curves, one can see that the saturation field increases with loading. The 4 and 6 % samples have saturation fields well below 500 Oe. For the 100 % sample, one has a saturation field $H_{SAT} \approx$ 1.2-1.4 kOe. This H_{SAT} value for the pure ferrite is very close to one third of the measured $\langle 4\pi M \rangle_{SAT}$. This means that the 100 % sample behaves as expected from simple demagnetizing field considerations. The lower H_{SAT} values for the lower loadings imply lower values of $\langle 4\pi M \rangle_{SAT}$ for these samples. The $\langle 4\pi M \rangle_{SAT}$ vs. loading response will be discussed in more detail below.

Third, consider the $\langle 4\pi M \rangle$ vs. H response in the $H \to 0$ limit. The slope of this low field response corresponds to $4\pi\chi$, where χ is the initial susceptibility. From the saturation field $H_{SAT} \approx \langle 4\pi M \rangle_{SAT}/3$ at 100 % loading as noted above, one has $4\pi\chi|_{L=100\,wt\%} \approx 3$. The data in Fig. 1 show that as the loading is reduced, the $4\pi\chi$ values also decrease. A magnetically soft spherical particle with any value of $\langle 4\pi M \rangle_{SAT}$ would have a saturation field of $\langle 4\pi M \rangle_{SAT}/3$. This means that for independent spherical ferrite particles of any kind, the $4\pi\chi$ should depend only on

the loading and vary as $3L/100$. The $4\pi\chi$ should not depend on the $\langle 4\pi M \rangle_{\mathrm{SAT}}$ for the sample. Further discussion will follow below.

Figure 5.2.3 shows the $\langle 4\pi M \rangle_{\mathrm{SAT}}$ data vs. the ferrite loading L. The solid circles show the $H = 5$ kOe data points from Fig. 5.2.2. The solid square shows the reference saturation induction measured for the commercial TT2-111 sphere at $H = 5$ kOe as well. The solid line shows the linear response one would expect for an unmodified ferrite phase with a saturation induction value the same as that

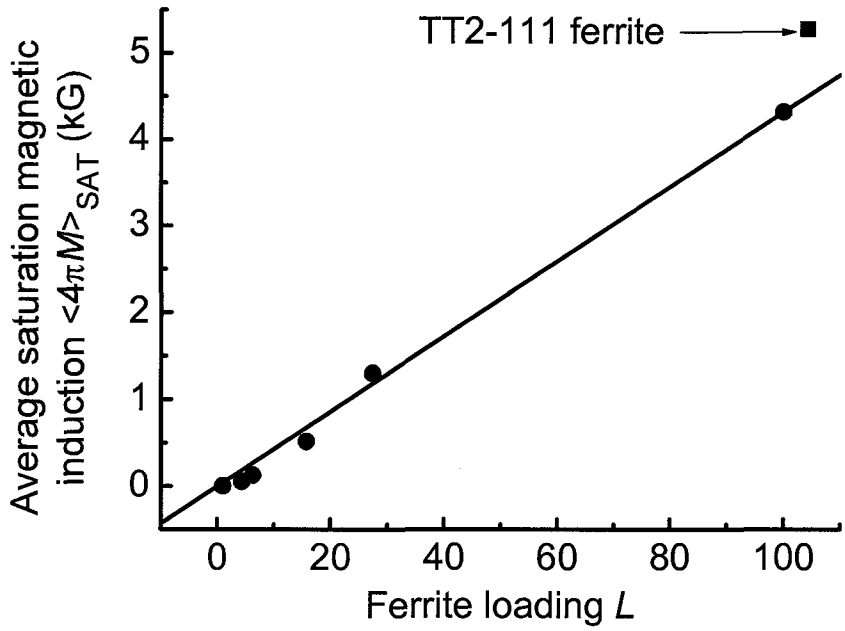

FIG. 5.2.3. Average saturation magnetic induction $< 4\pi M >_{\mathrm{SAT}}$ as a function of ferrite loading L. The data were obtained for an applied magnetic field of 5 kOe. The solid circles show the data for the composites. The solid square shows the value for the commercial TT2-111 ferrite. The solid line shows the linear response expected for an unmodified ferrite phase.

obtained for $L = 100$ %. The Fig. 2 data quantify the $\langle 4\pi M \rangle_{SAT}$ vs. L response evident in Fig. 5.2.2. The data show that the magnetic induction scales with the sample loading, in a linear fashion as is expected from a simple model with an unmodified ferrite phase.

Figure 5.2.4 shows additional data on H_{SAT} and $4\pi\chi$ as a function of loading, as well as new data on the coercive force H_C vs. L. Graph (a) shows H_{SAT} values obtained from the extrapolated low field responses shown in Fig. 1 to the

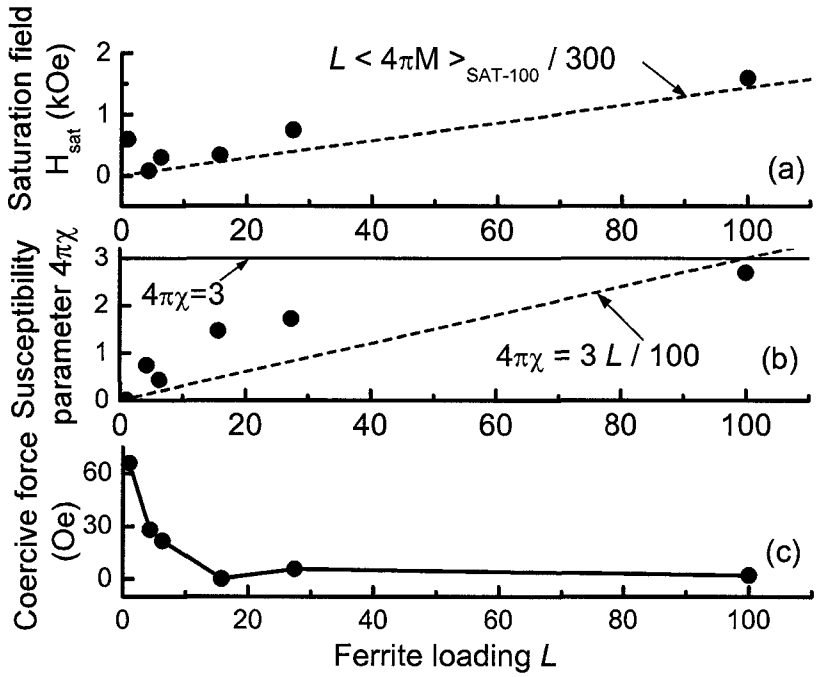

FIG. 5.2.4. Saturation field H_{SAT}, the initial susceptibility $4\pi\chi$, and the coercive force H_C as functions of ferrite loading L. The solid circles in (a) show the saturation field data. The dashed line corresponds to $H_{SAT} = L\langle 4\pi M \rangle_{SAT\text{-}100}/300$ where $\langle 4\pi M \rangle_{SAT\text{-}100}$ is the $\langle 4\pi M \rangle_{SAT}$ value for the 100 wt. % sample. The solid circles in (b) show the susceptibility parameter data. The solid line corresponds to $4\pi\chi = 3$ and the dashed line corresponds to $4\pi\chi = 3L/100$. The solid circles in (c) show the coercive force data.

$\langle 4\pi M\rangle_{\text{SAT}}$ points for each data set. These data are shown by the solid circles. The dashed line corresponds to a linear change in H_{SAT} according to $H_{\text{SAT}} = L\langle 4\pi M\rangle_{\text{SAT-100}}/300$, where $\langle 4\pi M\rangle_{\text{SAT-100}}$ is the $\langle 4\pi M\rangle_{\text{SAT}}$ value for the 100 % sample. Graph (b) shows the $4\pi\chi$ results. The data are shown by the solid circles. The dotted line corresponds to the value of $4\pi\chi = 3$ expected for a spherical ferrite phase. The dashed line shows the linear $4\pi\chi = 3L/100$ response expected for independent ferrite spherical grains. Graph (c) shows the coercive force data. The solid line simply connects the data points.

Apart from the sample with the lowest ferrite loading, the H_{SAT} data in Fig. 5.2.4 (a) show a linear increase with L and an end point value at $L = 100$ % that is close to $\langle 4\pi M\rangle_{\text{SAT}}$. The linear response shown by the dashed line is what one would expect from a mean field model, that is, a sample with strongly coupled magnetic particles that acts like a uniformly magnetized material with a $\langle 4\pi M\rangle_{\text{SAT}}$ equal to $L\langle 4\pi M\rangle_{\text{SAT-100}}/100$ and $H_{\text{SAT}} = \langle 4\pi M\rangle_{\text{SAT}}/3$. The fact that the data lie slightly above the dashed line is an indication that the coupling is not perfect and a mean field model is not strictly applicable. Fully noninteracting particles would give an $L-$independent H_{SAT} equal to $\langle 4\pi M\rangle_{\text{SAT-100}}/3$ for all samples.

The $4\pi\chi$ data in Fig. 5.2.4(b) show a general increase with loading, but the points generally fall well above the linear response line. Interactions between the spherical particles would give an $L-$independent susceptibility value of 3. Completely

independent ferrite inclusions on the other hand would give a linear dependence of susceptibility on L. The somewhat larger than linear $4\pi\chi$ values for intermediate $L-$values indicate, therefore, that there may be some level of interaction between the ferrite particles.

The H_C data in Fig. 4(c) show a small coercive force at large loadings and a rapid increase when one drops below $L = 16$ vol. %. The small values at the large loadings are consistent with the properties of the original TT2-111 material and support the existence of essentially unmodified ferrite grains in the composites down to $L = 16$ vol. % or so. However, it is not clear why there is such a drastic increase in the coercive force as the loading is reduced below 16 vol. %.

5.2.3 FERROMAGNETIC RESONANCE RESPONSE

Ferromagnetic resonance (FMR) and high field effective linewidth techniques were used to characterize the microwave losses. This section presents the FMR results. Section V gives the high field effective linewidth results. The FMR profiles were measured by a shorted waveguide reflection technique at an operating frequency of 9.5 GHz. Measurements were made on nominal 1 mm diameter spheres for the TT2-111 and the 100 % materials and nominal 3 mm diameter spheres for the materials with lower loadings. The samples were mounted in the middle of the wave guide cross section on a Rexolite® rod and positioned a half wavelength from an adjustable short. The additional loading introduced by the

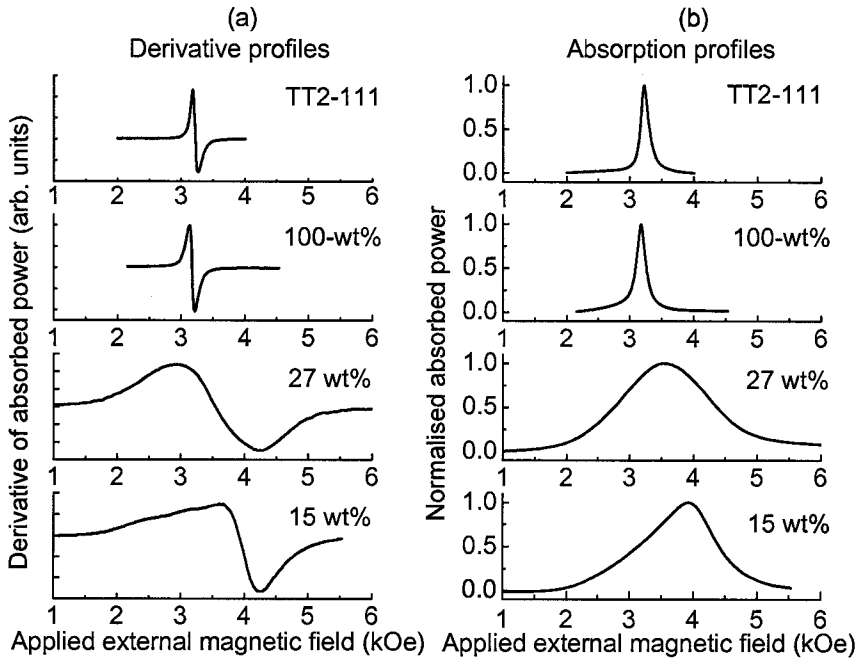

FIG. 5.2.5. Ferromagnetic resonance profiles at 9.5 GHz. The (a) graphs show the measured derivative of the absorbed power vs. applied magnetic field for the TT2-111 sample and the 100, 27, and 15 wt. % samples, as indicated. The (b) graphs show integrated FMR absorption profiles based on the derivative data in the corresponding (a) graphs.

samples at the FMR loss point in field was so small that field modulation and lock-in detection methods were needed to observe the response. The raw data consisted of profiles of the uncalibrated field derivative of the FMR absorption vs. field. Absorption profiles of loss vs. field were obtained from direct integration of the raw data. These integrated data were then used to determine the resonance field peak position H_{FMR} and the half power linewidth ΔH_{FMR}.

The FMR derivative profiles for the TT2-111 and 100 samples were well resolved and close to the general response expected from dense nickel zinc ferrite materials. The data for the 27 and 15 % samples, however, showed that any appreciable drop in the ferrite loading below 100 % causes a large degradation in the FMR response.

This conclusion carries over to the extreme for the samples with the smaller loadings. These samples showed no recognizable FMR response.

Figure 5.2.5 shows the actual FMR data in two formats. The (a) graphs show the measured derivative of the absorbed power vs. applied magnetic field profiles for the TT2-111, and L = 100, 27, and 15 % samples, as indicated. The (b) graphs show the integrated profiles for the derivative profiles in (a). The absorption profiles in (b) have all been scaled to give a peak absorption value of unity. Both the raw data and the integrated profiles show that the FMR lines are narrow and symmetric for the TT2-111 and 100 % samples. These lineshapes are near Lorentzian. On the other hand, for the 27 and the 15 % samples, the absorption profiles are broad and distorted, and nowhere near Lorentzian in shape. One can also see that the peaks for the 27 and the 15 % samples are also shifted up in field relative to the FMR positions for the two dense samples.

Table 5.1 summarizes the basic FMR parameters including the FMR field H_{FMR}, the effective gyromagnetic ratio, the FMR half power linewidth ΔH_{FMR}, and the high field effective linewidth ΔH_{eff}. The FMR field is taken at the peak loss point in the (b) graphs. The gyromagnetic ratio, defined for spherical samples as $\gamma_{\mathrm{eff}} = -2\pi f / H_{\mathrm{FMR}}$ (Sparks 1964), is shown in practical units as $|\gamma_{\mathrm{eff}}|/2\pi$. For electron based atomic moment systems, γ_{eff} is negative. For spin only moments with a Landé g-factor of 2, $|\gamma_{\mathrm{eff}}|/2\pi$ is equal to 2.8 GHz/kOe. The linewidth ΔH_{FMR} is taken as the full width at half maximum of the profiles in (b).

Table 5.1 summarizes the FMR data and the effective linewidth results to be considered in the next section. The FMR fields for the TT2-111 and the 100 % are close to 3.2 kOe and the corresponding $|\gamma_{eff}|/2\pi$ values of about 3 GHz/kOe are slightly higher than the free electron value. These samples also show relatively narrow linewidths in the 150-170 Oe range. These represent typical FMR parameters for dense ferrite materials. This situation is not maintained for the samples with lower ferrite loadings. Here one finds higher FMR fields and much lower $|\gamma_{eff}|/2\pi$ values than one would expect for any reasonable ferrite. At the same time, one sees large departures from a Lorentzian line shape and very large increases in the linewidths by a factor of ten or so.

It is evident that a simple change in the ferrite loading has a drastic effect on the FMR response for these composite materials. The data show that any reduction in the ferrite loading below 100 vol. % level serves to degrade the FMR response severely. It is worthwhile to consider two possibilities, among many, for this degradation. First, it is likely that the imbedding process yields ferrite particles with irregular shapes, large strains, and impurities. All of these factors are known to produce large linewidths. Second, in the extreme view, one can consider the composite as a polycrystalline ferrite with a very large porosity. It is well known that even a small amount of porosity in a ferrite material can produce a large inhomogeneously broadened line. Typical porosity broadened half power linewidths for spinel ferrites at 10 GHz are in the 30 - 40 Oe per percent.

Table 5.1. Summary of 9.5 GHz ferromagnetic resonance and effective linewidth results

Vol. % ferrite loading L	FMR Field H_{FMR} (Oe)	Effective gyromagnetic ratio $\lvert\gamma_{eff}\rvert/2\pi$	FMR linewidth ΔH_{FMR} (Oe)	High field effective linewidth ΔH_{eff} (Oe)
100	3223	2.95	157	6
100	3175	2.99	168	8
27	3549	2.68	1596	97
16	3924	2.42	1260	480
6	--	--	--	367

It may also be noteworthy that for the $L = 16$ vol. % sample, the FMR absorption profile is also highly distorted. The indication here is that for dilute loadings, the factors enumerated above result in more than a simple linebroadening. The detail origins of these distortions are not yet clear

5.2.4 HIGH FIELD EFFECTIVE LINEWIDTH RESULTS

The FMR results presented in the previous section show that any amount of ferroelectric loading causes a severe degradation of the linewidth. This section considers the microwave loss as measured at high field rather than at ferromagnetic resonance. In conventional ferrites, one can use high field measurements of the so-called effective linewidth to determine near intrinsic losses even when the FMR linewidth is broadened by microstructure effects or inhomogeneities of various types (Patton 1975), (Mo *et al*, 2005). This section presents the results of similar measurements on the present ferrite-ferroelectric composite materials.

The high field microwave response was evaluated for the composites for a field range of 5-11 kOe at 10 GHz, and high field effective linewidth determinations were made from these data. Reasonable results were obtained for the samples with 10, 25, 50, and 100 wt. % loadings. For the samples with lower L values, the high field losses were too large to obtain meaningful determinations of the effective linewidth. The working equations for the high field microwave response and the effective linewidth analysis are given in Appendix 3.

Figure 5.2.6 shows measurement results for the cavity frequency shift as a function

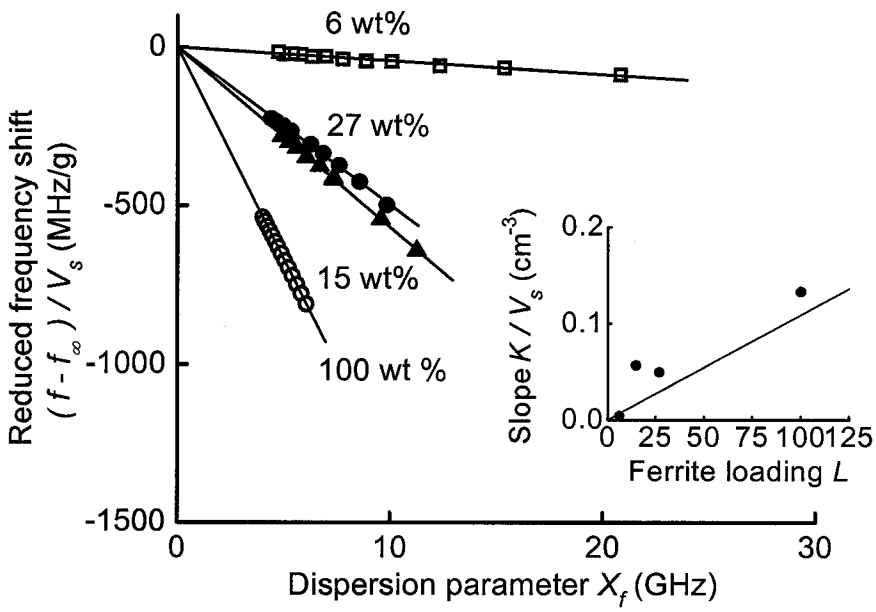

FIG. 5.2.6. Reduced cavity frequency shift $(f - f_\infty)/m$ as a function of the dispersion parameter X_F for the different ferrite loadings, as indicated. The solid lines show linear fits to the different data sets. The inset shows the response slope parameter K/m as a function of the ferrite loading L. The solid circles in the inset show the slopes of the line fits in the main graph and the line shows the calculated theoretical response based on microwave perturbation theory.

of field. The data in the main graph are shown in an $(f-f_\infty)/V_S$ vs. X_F format for the 6, 15, 27, and 100 % samples, as indicated. The solid lines show linear fits to the different data sets. The solid points in the inset shows the slopes of line fits as a function of the loading L for the different samples, and the straight line shows the expected slope response from Eq. (A3.1).

The X_F values were obtained from the raw f vs. H data and Eq. (A3.4). The $4\pi M_S$ was taken as the static magnetic induction value $\langle 4\pi M \rangle_{\mathrm{SAT}}$ for the ferrite sample. The $(f-f_\infty)/V_S$ format for the vertical axis display was used so that all the data for the samples with different loadings could be compared in a consistent manner. While the extrapolated f_∞ values vary from sample to sample, depending on the overall cavity loading, a display based on $(f-f_\infty)/V_S$ will extrapolate to a vertical axis value of zero in the $X_F = 0$ limit. From Eq. (A3.3), one sees that the K parameter scales with the sample volume V_S. The slope of a given $(f-f_\infty)/V_S$ vs. X_F plot, therefore, should scale with the loading L.

All of the data plots in Fig. 5.2.6 confirm the expectation from Eq. (A3.1) that $(f-f_\infty)/V_S$ is a linear function of X_F with a negative slope. The general trend of the slopes from these plots to scale with the loading L, with the notable exception for $L =$ 15 %, is also consistent with the expectation from Eqs. (A3.1) and (A3.3). The slope results in the inset make this trend quantitative and show that the response is reasonably close (except for the $L =$ 15 % point) to the solid line result from perturbation theory. The fact that the fitted slope values from the data fall about

10% above the solid line is consistent with sample loading effects measured by Truedson *et al* (Truedson *et al.* 1994).

It is not clear why the $(f-f_\infty)/V_s$ vs. X_F response for the 15 % sample should be so anomalous. There is no inconsistency in the corresponding static magnetization vs. field date that would point to such a large anomaly in the off resonance microwave response.

Figure 5.2.7 shows corresponding results on the inverse cavity Q factor as a function of field. The data in the main graph are shown in a $(1/Q-1/Q_\infty)/K$ vs. X_Q format for the same samples as used for the data in Fig. 5.2.6. The format is the

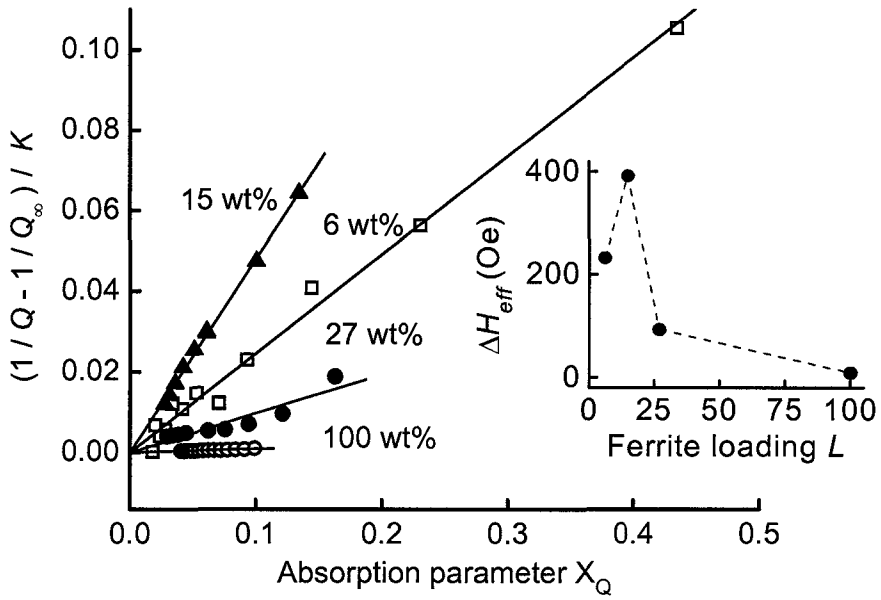

FIG. 5.2.7. Reduced sample loss parameter $(1/Q-1/Q_\infty)/K$ as a function of the absorption parameter X_Q for different ferrite loading values, as indicated. The inset shows the extracted high field effective linewidth ΔH_{eff} as a function of ferrite loading L.

same as for Fig. 5.2.6. The solid lines show linear fits to the different data sets. The solid points in the inset shows the slopes of line fits as a function of the loading L for the different samples.

The X_Q values were obtained from the raw f vs. H data and Eq. (A3.5). The $(1/Q-1/Q_\infty)/K$ format for the vertical axis display was used so that the data for the samples with different loadings could be compared in a consistent manner. For a linear $(1/Q-1/Q_\infty)/K$ vs. X_Q response, moreover, one can see from Eq. (2) that the slope for a given data set corresponds directly to the high field effective linewidth ΔH_{eff}.

All of the data plots in Fig. 5.2.7 confirm the expectation from Eq. (A3.2) that $(1/Q-1/Q_\infty)/K$ is a linear function of X_Q with a positive slope. This means, as noted above, that one has a well defined high field effective linewidth that corresponds to the slope of the response for each data set. As the inset to Fig. 5.2.7 shows, with the exception of the data for $L =$ 15 %, there is a general trend in these slopes, and hence ΔH_{eff}, to decrease as the loading is increased. The actual fits give relatively small effective linewidth values of 8 Oe at $L = 100$ %, 93 Oe at $L = 27$ %, and 392 Oe at $L =$ 15 % and 232 Oe at $L =$ 6 %. As a point of reference, the TT2-111 material had $\Delta H_{\text{eff}} = 6$ Oe. It is important to note that the anomalously large slope and corresponding ΔH_{eff} value of 392 Oe for the $L =$ 15 % sample is not a carry over from the anomaly in the noted in the $(f-f_\infty)/V_s$ vs. X_F response discussed above. This anomaly is normalized out by the K divisor in the vertical

axis display used for Fig. 5.2.7. Rather, this anomalously large ΔH_{eff} provides evidence in its own right that there is something problematic about this sample. These ΔH_{eff} values are the same as listed in Table 5.1.

There are several effects that are passed over in the $(1/Q-1/Q_{\infty})/K$ vs. X_Q display format used for Fig. 5.2.7. This relates to the actual values of the high field $Q-$values that lead to the $1/Q_{\infty}$ offset in the first place. It was found that a decrease in loading to the 15 or 6 % levels caused a significant drop in the Q_{∞} values for the cavity. Typical Q_{∞} values for the cavity with the TT2-111 sample, the 100 % composite, were in the 20,000 to 22,000 range. It is interesting to note that even a drop in loading to 27 % caused only a drop in Q_{∞} - value to about 20,000. These values amount to a very small degradation from the nominal empty cavity Q of 22,500 or so. For the 15 and 6 % loading samples, however, the Q_{∞} degraded to about 7,000 and 5,000, respectively.

The fact that the K/V_s value for the $L=6$ % sample, as shown in the Fig. 5.2.6 inset, is consistent with the corresponding values for the 27 and 100 % samples, indicates that the drop in Q did not affect the cavity calibration. It is possible, however, that the factor of four ΔH_{eff} increase in going from $L=27$ % to $L=6$ % could be due to the same process that causes the factor of four drop in Q_{∞}. It is possible that the large ferroelectric component introduces ohmic losses that affect both Q_{∞} and ΔH_{eff}. Truedson *et al.*(Truedson *et al.* 1994) have shown that ohmic

losses in a ferrite disk can give the appearance of a contribution to the high field ΔH_{eff}.

5.2.5 SUMMARY AND CONCLUSIONS

The above sections have described preparation methods and measurement results on the magnetic properties of a ferrite – ferroelectric composite fabricated from a Paratek barium strontium titanate material and a Trans Tech nickel zinc ferrite TT2-111 material. The ferrite loading levels were varied from the pure BSTO material ($L = 0$) to pure TT2-111 ($L = 100$ vol. %). Initial susceptibility, saturation field, and coercive force data show trends consistent with the saturation magnetization results.

The magnetic response at high frequency show similar effects. Any amount of BSTO added to the ferrite phase causes a severe degradation in the FMR profile and linewidth as well as the high field off resonance effective linewidth. The XRD data and a comparison of magnetic properties for the $L = 100$ vol. % material and a commercial TT2-111 baseline sample indicate that the processing recipe used for the composite materials did not cause any degradation in the NZF or the BSTO phase. The actual composites, on the other hand, all show a clear degradation in the magnetic properties.

The static magnetic results point to a model of unmodified spherical NZF inclusions in a non magnetic matrix. The FMR and high field effective linewidth results show that the presence of interactions between the two phases, the shape of

the NZF inclusions and extreme dilution due to the large amount of ferroelectric material can affect the magnetic losses. Further work is needed to develop fabrication processes that can preserve the desirable ferroelectric and ferrite properties of the composite, while at the same time, produce a multifunctional material with enhancements in both classes of properties.

SPECIAL ACKNOWLEDGEMENTS

The author would like to acknowledge Paratek Microwave Inc. for providing the samples. The author is also indebted to Mr. Elwood Hoakenson and Trans-Tech, Inc., Adamstown, Maryland, for a sample of TT2-111 ferrite for static and microwave magnetic characterization. Dr. Sandeep Kohli of the Chemistry dept, Colorado State University, is acknowledged for assistance with the X-ray diffraction measurements.

5.3 REFERENCES

(Abeles 1976).B. Abeles Solid State Scie. **6**, 1 (1976).

(Abeles et al.1975).B. Abeles, H. L. Pinch and J. I. Gittleman Phys. Lett. **35,** 247 (1975).

(Aspnes 1982).D. E. Aspnes Phys. Rev. Lett. **48,** 1629 (1982).

(Atkinson and Davies 2000).H. V. Atkinson and S. Davies Metall. Mater. Trans. A **31A**, 2981 (2000).

(Bergman and Stroud, 1992).D. J. Bergman and D. Stroud Solid State Phys. **46**, 147 (1992).

(Bergman et al., 1994).D. J. Bergman, O. Levy and D. Stroud Phys. Rev. B **49**, 129 (1994).

(Bergman, 1978).D. J. Bergman Phys. Rep. **43**, 377 (1978).

(Bergman, 1979).D. J. Bergman Phys. Rev. B **19**: 2359 (1979).

(Bergman, 1981).D. J. Bergman Phys. Rev. B **23**, 3058 (1981).

(Geyer et al. 1996). R. G. Geyer, J. Krupka, L. Sengupta and S. Sengupta. Proceedings of the Tenth IEEE International Symposium on Applications of Ferroelectrics IEEE Catalog Number 96CH35948 (1996).

(Grannan, 1981).D. M. Grannan, J. C. Garland and D. B. Tanner Phys. Rev. Lett. **46**, 375 (1981).

(Grimes and Grimes, 1991).C. A. Grimes and D. M. Grimes J. Appl Phys **69**, 6168 (1991).

(Kanai et al. 2001).T. Kanai, S. Ohkoshi, A. Nakajima, T. Watanabe and K. Hashimoto Adv. Mater **13,**: 487 (2001).

(Kaskatkina et al.1983).T. S. Kaskatkina, Y. M. Yakovlev, S. L. Matskevich and I. K. Berestovaya Sov. Phys. Solid State **25**, 999 (1983).

(Mantese et al., 1996).J. V. Mantese, A. L. Micheli, D. F. Dungan, R. G. Geyer, J. Baker-Jarvis and J. Grosvenor J. Appl Phys **79**, 1655 (1996).

(Mo *et al*, 2005). N. Mo, Y. Y. Song, C. E. Patton, J. Appl. Phys, **97**, 093901 (2005).

(Nazarov et al. 2003).A. V. Nazarov, D. Menard, J. J. Green, C. E. Patton, G. M. Argentina and H. J. Van Hook J. Appl. Phys. **94**(11), 7227-7234 (2003).

(Patton 1969).C. E. Patton Phys. Rev. **179**, 352 (1969).

(Patton 1970).C. E. Patton J. Appl. Phys **41**, 1637 (1970).

(Patton 1975). *Microwave resonance and relaxation.* Magnetic Oxides. D. J. Craik, John Wiley, London: 575-645 (1975).

(Patton and Van Hook 1972 \).C. E. Patton and H. J. Van Hook J. Appl. Phys **43**, 2872 (1972).

(Qi et al., 2004).X. Qi, J. Zhou, Z. Yue, Z. Gui and L. Li J. Mag. Mag. Mater **269**: 352 (2004).

(Roschmann 1975).P. Roschmann IEEE Trans. Magn. **14**, 1247 (1975).

(Schlomann 1956). AIEE Special Publication No. T-91 (unpublished): 600 (1956).

(Schlomann 1958).E. Schlomann J. Phys. Chem. Solids **6**, 242 (1958).

(Seiden and Grunberg 1963).P. E. Seiden and J. G. Grunberg J. Appl. Phys. **34**, 1696 (1963).

(Sengupta and Sengupta 1997).L. C. Sengupta and S. Sengupta IEEE Trans. Ultrasonics, Ferroelectrics and Frequency Control **44**(4), 793 (1997).

(Sparks 1964). M. Sparks, *Ferromagnetic Relaxation Theory*, (McGraw-Hill, New York, 1964)

(Sparks et al. 1961).M. Sparks, R. Loudon and C. Kittel Phys. Rev. **122**, 791 (1961).

(Truedson et al. 1994).J. R. Truedson, P. Kabos, K. D. McKinstry and C. E. Patton J. Appl. Phys. **76**(1), 432 (1994).

(Valenzuela 1994). Valenzuela, *Magnetic Ceramics*, (Cambridge University Press, 1994)

(Van Hook and Willingham 1984).H. J. Van Hook and C. B. Willingham Adv. Ceram. **15**, 1637 (1984).

(Van Hook et al. 1968).H. J. Van Hook, J. J. Green, F. Euler and E. R. Czerlinsky J. Appl Phys **39,** 730 (1968).

SUMMARY AND CONCLUSIONS

Outline:

6.1: Summary of the work in the dissertation

6.2: Conclusions and future directions

6.1 SUMMARY OF THE WORK IN THE DISSERTATION

The work in this dissertation focussed on the measurement and analysis of ferromagnetic resonance (FMR) linewidth in different materials useful for device applications to study the prevalent microwave loss mechanisms. The materials for this study included (1) metal films, which find use in high-density magnetic recording, (2) ferrites, which have wide applications in isolators, circulators etc., and (3) ferrite-ferroelectric composite materials, which belong to the newly emerging field of multifunctional materials.

Frequency dependence of the FMR linewidth in metal films and bulk ferrites have helped unravel some of the damping mechanisms prevalent in these materials. Experimental results of linewidth measurements in two types of metallic films have

been presented. One is the widely used Permalloy, which the material of choice for most applications, where the soft magnetic properties and low losses are required. For example, it is used for shielding, in magnetic read/write heads. The FMR linewidth measurements on sputtered Permalloy films have been compared for two different substrates. Comparative measurements were first done by three different experimental techniques in order to compare the reliability of these techniques. Data shown in the dissertation have been taken by the traditional FMR spectroscopy, where the field FMR linewidth was measured as a function of frequency, both in-plane and perpendicular-to-plane configurations of external static field. Out-of-plane angular dependence of FMR linewidth was also studied. The data indicate magnon-electron scattering as a dominant intrinsic relaxation mechanism. The extrinsic contribution result in a broadening in the FMR line, due to inhomogeneities. Phenomenologically the data could be modelled by a combination of the Landau-Lifshitz or Gilbert type of damping model and a constrained Codrington-Olds-Torey model. Contribution of eddy current losses were dominant for thicker films. Comparison of in-plane and out-of-plane measurements indicate that the inhomogeneity contribution to the FMR linewidth is not negligible.

The second metallic film system under study was nitrogenated iron-titanium alloy (Fe-Ti-N). This material has been recently suggested for use in the next generation of magnetic recording heads due to its soft magnetic properties and high saturation magnetic induction. A systematic study of static magnetic properties and microwave properties has been done in Fe-Ti-N films for different nitrogen content, and in a

wide frequency range. The FMR linewidth results point to a relation between the structural transition and the microwave loss. The intrinsic damping parameter α values for all these films have been found to be on the order of 0.005. This value corresponds to that in low loss Permalloy films. The extrinsic contribution to linewidth can be inferred as arising from two magnon scattering due to random anisotropy in the grains, and an inhomogeneity based linebroadening which is dependent on the nitrogen content. The addition of nitrogen to the Fe-Ti matrix and the accompanying changes in the anisotropy, grain size and the structure, therefore results in a contribution to the extrinsic damping of the films.

The results of linewidth measurements in two types of ceramic materials, which find its use in several microwave devices, have been presented. With the porosity almost eliminated by the recently developed procedure of hot isostatic pressing (hipping), it was possible to measure frequency dependence of the two-magnon anisotropy scattering contribution to linewidth directly in yttrium iron garnet spheres. The results have been fit to Schloemann's two magnon anisotropy scattering theory. The second material investigated for device application was the composite system of ferrite and ferroelectric materials. Results on static and microwave magnetic measurements have been presented. The static magnetic results point to a model of unmodified spherical NiZn ferrite (NZF) inclusions in a non magnetic matrix. The FMR and high field effective linewidth results show that the presence of interactions between the two phases, the shape of the NZF inclusions and extreme dilution due to the large amount of ferroelectric material affect the magnetic losses.

6.2 CONCLUSIONS AND FUTURE DIRECTIONS

Ferromagnetic resonance linewidth is a sensitive tool to the detection of the effect of microstructure on the microwave relaxation processes in ferromagnetic materials. Frequency dependence of linewidth helps in unravelling some of the many processes that affect the FMR linewidth. In plane, out of plane angle dependences and perpendicular to the plane measurements of FMR linewidth have helped establish the Landau-Lifshitz or Gilbert type of phenomenology as the most appropriate for modelling of the intrinsic damping mechanism in metallic films. The physical mechanism suggested is the magnon electron scattering. The FMR line also shows the presence of a linebroadening effect in addition to the effect of the damping mechanism to the linewidth. The ripple field affects the linewidth even at high frequencies can be used to model the frequency dependence of the linewidth. It causes a spurious increase in both, frequency and field swept linewidth at lower frequencies. This increase in frequency swept linewidth has been observed using the PIMM set up at NIST, Boulder. However the data analysis is extremely involved and possible effects of the narrow waveguide width on the calculated damping are still being investigated. A suggested direction would be the use of VNA-FMR set up with a wider waveguide coupled with a lock-in detector, to measure the linewidth at frequencies lower than 2 GHz.

The role of two-magnon scattering processes in Permalloy films can be corroborated with the utilization of the broad frequency range for FMR measurements. Also, the question of the origin of uniaxial anisotropy in Permalloy films is unresolved. A careful deposition of thin films with varying deposition conditions like thickness down to the percolation thickness, and the magnitude and direction of the applied field during deposition need to be made. Careful static magnetic and FMR measurements will then go a long way in the resolution of this question.

In the nitrogenated Fe-Ti system, a distinct dependence of saturation magnetization, coercive force, remanance, and anisotropy on the nitrogen content has been observed. All these parameters appear to follow a trend in the structural transition from bcc to bct. Ferromagnetic resonance results also point to a relation between the structural transition and the microwave loss. Frequency dependence of the FMR linewidth throws new light on the dynamic properties of these materials. The presence of two magnon scattering due to anisotropy has been established. At the structural transition point of about 7 at. % nitrogen, the contribution of the two magnon scattering is minimal.

Temperature dependence of the FMR linewidth down to low temperatures might shed some more light on the microwave relaxation processes in the metal films. High power microwave measurements could also be of interest, since the connection between the grain size and microwave loss at high power can be investigated.

Composite materials show some promise in multifunctional applications. They need to be better processed and one needs to make a careful choice of ferrites to be incorporated into the ferroelectric matrix. A study of bulk materials on the other side of the spectrum studied in this dissertation i.e. for ferrite loadings between 50 and 100 wt. % will be extremely helpful. Another step towards materials for device applications will be deposition of these materials as a film. Layered structured of ferrite and ferroelectric materials are already being studied by some research groups; however films with composite materials is another avenue of promising research.

APPENDIX - 1

TABLE OF MATERIALS USED IN THIS DISSERTATION

MATERIAL	METHOD	SOURCE	SAMPLE DETAILS
Ni-Fe on glass	Sputtering	Dr. Michael Schneider, NIST, Boulder, CO	$S10_g$, $S25_g$, $S50_g$, $S100_g$, $S150_g$ (numbers indicate thickness in nm)
Ni-Fe on Si	Sputtering	Dr. John Nibarger, Sun Microsystems, Golden CO	$S10_{Si}$, $S25_{Si}$, $S50_{Si}$, $S100_{Si}$, $S150_{Si}$, $S200_{Si}$, $S250_{Si}$ (numbers indicate thickness in nm)
Fe-Ti-N	Sputtering	Dr. Yunfei Ding, MINT, University of Alabama, AL	Fe-Ti-N with nitrogen content x_N = 0, 1.9, 3.9, 5.4, 7, 8.4, 10.9, and 12.7 at. %

MATERIAL	METHOD	SOURCE	SAMPLE DETAILS
YIG, substituted YIG	Conventional sintering, then hipping	Gil Argentina, Pacific Ceramics, Sunnyvale, CA	2 mm spheres for hipped and substituted YIG.
Composite materials	Conventional ball milling and sintering	Dr. L. Sengupta, Paratek Microwave Inc., Columbia, MD	2 mm spheres of material with ferrite loading L = 0, 0.3, 1, 5, 10, 25, 50 and 100 wt %
TT2-111 Ni- Zn ferrite	Conventional ball milling and sintering	Trans-Tech Microwave Inc.	TT2-111, 2 mm sphere.

APPENDIX - 2

VAN DER PAUW METHOD FOR RESISTIVITY MEASUREMENT

The **Van der Pauw** method, developed by L.J. van der Pauw in 1958(Van der Pauw, 1958), is a simple technique for the determination of resistivity for a randomly shaped sample. The advantages of this method include low cost and simplicity.

The Van der Pauw technique can be used on any thin sample of material and the four contacts can be placed anywhere on the perimeter/boundary, provided certain conditions are met: (1) The contacts are on the boundary of the sample (or as close to the boundary as possible), (2) The contacts are infinitesimally small (or as close as possible), (3) The sample is thin relative to the other dimensions, (4) There

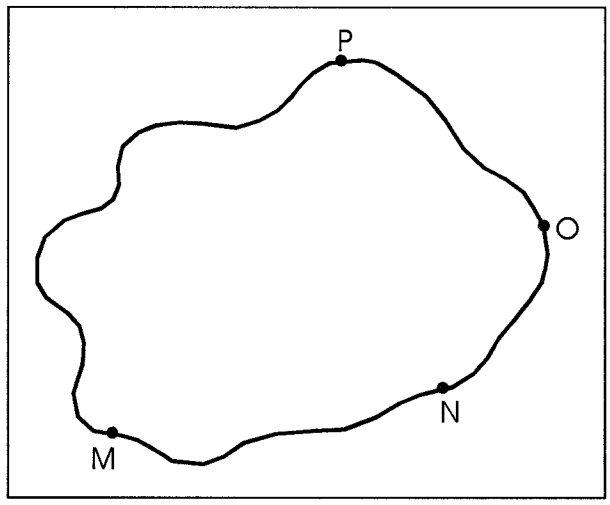

FIG A1.1 Point contacts on a sample to be measured.

are no isolated holes within the sample

Four small contacts M, N, O, P are made on the periphery of the film to be measured. The current i_{MN} is applied, and the potential difference $V_P - V_O$ is measured. Define

$$R_{MN,OP} = \frac{V_P - V_O}{i_{MN}}, \tag{A 2.1}$$

Analogously,

$$R_{NO,PM} = \frac{V_M - V_P}{i_{NO}}, \tag{A 2.2}$$

Between $R_{MN,OP}$ and $R_{NO,PM}$, there is a simple relation:

$$\exp\left(-\frac{\pi d}{\rho} R_{MN,OP}\right) + \exp\left(-\frac{\pi d}{\rho} R_{NO,PM}\right) = 1, \tag{A 2.3}$$

Here d is the film thickness and ρ is the resistivity of the material. In the general case, it is not possible to write ρ in an explicit form. However the solution can be written in the form

$$\rho = \frac{\pi d}{\ln 2} \frac{R_{MN,OP} + R_{NO,PM}}{2} f, \tag{A 2.4}$$

where f is a function only of the ratio $R_{MN,OP} / R_{NO,PM}$ given in general by

$$e^{-(\ln 2/f)}\cosh\left[\left(\frac{(x_1/x_2)-1}{(x_1/x_2)+1}\right)\left(\frac{\ln 2}{f}\right)\right]=\frac{1}{2}, \qquad \text{(A 2.5)}$$

(Van der Pauw 1958) L. Van der Pauw, A method of measuring the resistivity and Hall coefficient on lamellae of arbitrary shape, Philips Technical Review **20** (8), 220. (1958)

APPENDIX - 3

HIGH FIELD EFFECTIVE LINEWIDTH MEASUREMENT FOR COMPOSITE MATERIALS WITH MAGNETIC INCLUSIONS

The effective linewidth technique is based on measurements of the change in the frequency f and quality factor Q with field for a high Q cylindrical microwave cavity with the magnetic sample in place. Typically, the measurement is made with applied fields well above the FMR field. For such high fields, the spin wave band is shifted well above the nominal cavity and signal frequency. This eliminates, in principle, any contribution to the magnetic losses due to any inhomogeneities that may be present in the sample.

Such measurements allow one to access the high field tail of the FMR response and determine the relaxation rate η for the driven mode that is applicable in the high field regime. Expressed in linewidth units, one can write an effective linewidth parameter $\Delta H_{\text{eff}} = 2\eta / |\gamma|$. This ΔH_{eff} simply expresses the relaxation rate in field units for convenient comparison with actual linewidth data. For simplicity, the conversion from a relaxation rate to ΔH_{eff} uses the free electron gyromagnetic ratio γ rather than the γ_{eff} introduced in Section IV. The difference is small. In the high field regime of loss, the intrinsic γ is also more applicable.

For a typical polycrystalline ferrite, one may have a 10 GHz FMR linewidth in the 100 - 200 Oe range, while the high field effective linewidth will be in 10 - 20 Oe range. (Patton, 1975) In the case of very dense ferrites, one finds that ΔH_{eff} approaches intrinsic single crystal linewidth values in the limit of very high fields. (Mo *et al.*, 2005) As the results below will show, the effective linewidth situation for ferrite-ferroelectric composite materials is more complicated.

Truedson *et al.* provide a full description of the high field effective linewidth analysis procedure for materials in which one finds a constant ΔH_{eff} in the high field regime.(Truedson *et al.*, 1993) This is the applicable situation here. The sample is placed in the center of a TE_{011} cavity with a high Q, typically in the 20,000 range. The cavity frequency f and quality factor Q are then measured as a function of the field H in the high field regime, and the data are analyzed to obtain a high field ΔH_{eff} parameter. The analysis procedure is summarized below. Details of the measurement procedure as it applies to the present composite samples are given at the end of the section.

The working cavity response equations may be written as

$$f = f_{\infty} - K\, X_F(H, f) \qquad \text{(A 3.1)}$$

and

$$\frac{1}{Q} = \frac{1}{Q_\infty} + K\,\Delta H_{\text{eff}} X_Q(H,f)\ . \qquad \text{(A 3.2)}$$

In the above, f_∞ and Q_∞ denote the cavity frequency and quality factor in the limit of very high fields. In this limit, the magnetic response is essentially frozen out. The K parameter takes the form

$$K = C\,\frac{V_{\text{m}}}{V_{\text{cav}}}, \qquad \text{(A 3.3)}$$

where V_{m} denotes the active magnetic volume of the sample, C is a fixed parameter that depends on the cavity dimensions and cavity mode , and V_{cav} is the cavity volume. For the cavity used for this work, C/V_{cav} is equal to 0.109 cm^{-3}.

The $X_F(H,f)$ and $X_Q(H,f)$ denote field and frequency dependent dispersion and absorption parameters, respectively. In the case of an isotropic spherical magnetic sample, these parameters may be written as

$$X_F(H,f) = \frac{4\pi M_S\, H\, f}{H^2 - (f/|\gamma|)^2} \qquad \text{(A 3.4)}$$

and

$$X_Q(H,f) = \frac{4\pi M_S \left[H^2 + (f/|\gamma|)^2\right]}{\left[H^2 - (f/|\gamma|)^2\right]^2}\ , \qquad \text{(A 3.5)}$$

where $4\pi M_S$ is the saturation magnetic induction value for the magnetic sample. Note that in the high field limit in which $H^2 >> (f/|\gamma|)^2$ is satisfied, typically for fields above 5-6 kOe or so, the $X_F(H,f)$ scales essentially as $1/H$ and $X_Q(H,f)$ scales as $1/H^2$. The plots to be considered shortly for f vs. $X_F(H,f)$ and $1/Q$ vs. $X_Q(H,f)$ should be considered in this light.

From Eq. (1), one can see that the slope of the line obtained from a plot of the measured cavity frequency as a function of $X_F(H,f)$ will correspond to $-K$. From Eq. (2), one can also see that the slope of the plot of $1/Q$ as a function of $X_Q(H,f)$ will correspond to $K\Delta H_{\text{eff}}$. The ratio of the two slopes will then yield the high field effective linewidth ΔH_{eff}.

The data to be presented in the next section confirm that such linear f vs. $X_F(H,f)$ and $1/Q$ vs. $X_Q(H,f)$ responses are obtained for the series of composite samples of interest here. For ferrite-ferroelectric composites, however, it is also important to consider the way in which the K parameter scales with the sample mass and ferrite loading L. For the current samples, one may write the active magnetic volume as $V_{\text{m}} = V_s L/100$ where V_{s} is the density of the ferrite component. Based on this relation, one obtains a K parameter to sample volume ratio as

$$\frac{K}{V_s} = 0.00109L. \qquad \text{(A 3.6)}$$

This simple connection provides a simple test of the effect of loading on the cavity frequency response.

REFERENCES

(Patton, 1975) *Microwave resonance and relaxation*. Magnetic Oxides. D. J. Craik, John Wiley, London 575-645 (1975).

(Mo *et al*, 2005) N. Mo, Y. Y. Song, C. E. Patton, J. Appl. Phys, **97**, 093901 (2005).

(Truedson,*et al.*, 1993) Truedson, J. R., McKinstry, K. D., Kabos, P. and Patton, C. E., J. Appl. Phys 74(4), 2705-2718 (1993).

REFERENCES

(Abeles 1976) B. Abeles Solid State Scie. **6** 1 (1976).

(Abeles *et al.* 1975) B. Abeles, H. L. Pinch and J. I. Gittleman Phys. Lett. **35** 247 (1975).

(Alexander *et al.* 2000) C. Alexander, J. Rantschler, T. Silva and P. Kabos J. Appl. Phys **87**(9) 6633-6635 (2000).

(Alexander, 2005) Private communication (2005).

(Anderson, *et al.* 1971) Anderson, J., Bhagat, S. and Chen, F., Phys. Stat. Sol. **45**, 312.(1971)

(Aspnes 1982) D. E. Aspnes Phys. Rev. Lett. **48** 1629 (1982).

(Atkinson and Davies 2000) H. V. Atkinson and S. Davies Metall. Mater. Trans. A **31A** 2981 (2000).

(Bady 1967) I. Bady IEEE Trans. Magn. **3** 521 (1967).

(Barry 1986) W. Barry IEEE trans. Microwave theory and techniques **MTT-34** 80 (1986).

(Bergman and Stroud, 1992) D. J. Bergman and D. Stroud Solid State Phys. **46** 147 (1992).

(Bergman *et al.* 1994) D. J. Bergman, O. Levy and D. Stroud Phys. Rev. B **49** 129 (1994).

(Bergman, 1978) D. J. Bergman Phys. Rev. **43** 377 (1978).

(Bergman, 1979) D. J. Bergman Phys. Rev. B **19** 2359 (1979).

(Bergman, 1981) D. J. Bergman Phys. Rev. B **23** 3058 (1981).

(Bertaud and Pascard, 1965) Bertaud, A. J. and Pascard, H., J. Appl Phys **36**, 970.(1965)

(Bonin *et al.* 2005) Bonin, R., Schneider, M. L., Silva, T. J. and Nibarger, J. P., J. Appl Phys **98**, 123904.(2005)

(Cadieu *et al.* 1997) F. J. Cadieu, R. Rani, W. Mendoza, B. Peng, S. A. Shaheen, M. J. Hurben and C. E. Patton J. Appl. Phys **81** 4801 (1997).

(Celinski and Heinrich, 1991) Celinski, Z. and Heinrich, B., J. Appl. Phys. **70**, 5935 (1991).

(Chezan, 2002) Nanostructure and soft magnetic properties of iron-nitrogen alloys, University of Groningen, The Netherlands. Ph. D. (2002).

(Chikazumi 1997) S. Chikazumi, Physics of ferromagnetism. NY, (Oxford University Press, 1997)

(Cochran, *et al.* 1982) Cochran, J. F., Myrtle, K. and Heinrich, B., J. Appl Phys **53**, 1982.(1982)

(Craus, *et al.* 2002) C. Craus, A. Chezan, M. Siekman, J. Lodder, D. Boerma and L. Niesen J. Mag. Mag. Mater **240**(1-3) 423-426 (2002).

(Craus, *et al.* 2004) C. Craus, A. Chezan, D. Boerma and L. Niesen J. Phys. - Cond Mat **16**(50) 9227-9241 (2004).

(Das *et al.* 2006) J. Das, S. S. Kalarickal, K. S. Kim, and C. E. Patton Phys. Rev B (to be submitted)

(Ding and Alexander 2002) Y. Ding and J. C. Alexander J. Appl. Phys. **91** 7833 (2002).

(Ding and Alexander 2005) Private communication (2005).

(Ding and Alexander 2006) Y. Ding and J. C. Alexander IEEE Trans. Magn. **42** 5 (2006).

(Ding *et al.* 2001) Y. Ding, S. C. Byeon and J. C. Alexander IEEE Trans. Magn. **37** 1776 (2001).

(Frait and Fraitova, 1980) Frait, Z. and Fraitova, D., J. Mag. Mag. Mater **15-18**, 1081.(1980)

(Geshev *et al.* 1998) J. Geshev, A. D. C. Viegas and J. E. Schmidt J. Appl Phys **84** 1488 (1998).

(Geyer *et al.* 1996) R. G. Geyer, J. Krupka, L. Sengupta and S. Sengupta. Proceedings of the Tenth IEEE International Symposium on Applications of Ferroelectrics IEEE Catalog Number 96CH35948 (1996).

(Grannan, 1981) D. M. Grannan, J. C. Garland and D. B. Tanner Phys. Rev. Lett. **46** 375 (1981).

(Green and Kohane 1964) J. J. Green and T. Kohane SCP Solid State Technol. **7** 46 (1964).

(Griffiths 1946) J. H. E. Griffiths Nature **158** 670 (1946)

(Grimes and Grimes, 1991) C. A. Grimes and D. M. Grimes J. Appl Phys **69** 6168 (1991).

(Heinrich *et al.* 1985) Heinrich, B., Cochran, J. F. and Hasegawa, J. Appl Phys **57**, 3690.(1985)

(Heinrich, 2003) *Spin Relaxation in Magnetic Metallic Layers and Multilayers.* Springer Verlag (2003).

(Herring Kittel 1951) C. Herring and C. Kittel Phys. Rev. **81** 869 (1951).

(Herzer, 1990) G. Herzer IEEE Trans. Magn. **26** 1397 (1990).

(Hillebrands and Ounadjela, 2001) Hillebrands, B. and Ounadjela, K. E., *Spin Dynamics in Confined Magnetic Structures*, Springer, Berlin.(2001)

(Hoffman 1968) H. Hoffman IEEE Trans. Magn. Mag-**4** 32 (1968).

(Hurben 1996) Colorado State University. Ph. D. (1996).

(Hurben and Patton 1998) M. Hurben and C. Patton J. Appl. Phys **83**(8) 4344-4365 (1998).

(Husserl) E. Husserl. http //www.husserlpage.com/

(Jack, 1951) K. H. Jack Proc. Roy. Soc. **A 208** 200 (1951).

(Jack, 1994) K. H. Jack J. Appl. Phys. **76** 6620 (1994).

(Kalarickal *et al.* 2006) S. S. Kalarickal, P. Krivosik, M. Wu, C. E. Patton, M. L. Schneider, P. Kabos, T. J. Silva, and J. P. Nibarger, J. Appl Phys **99**(9), In Press.(2006)

(Kambersky 1976) V. Kambersky Czech. J. Phys. **B26** 1366 (1976).

(Kambersky and Patton 1975) V. Kambersky and C. E. Patton Phys. Rev. B **11** 2668 (1975).

(Kanai *et al.* 2001) T. Kanai, S. Ohkoshi, A. Nakajima, T. Watanabe and K. Hashimoto Adv. Mater **13** 487 (2001).

(Kaskatkina *et al.* 1983) T. S. Kaskatkina, Y. M. Yakovlev, S. L. Matskevich and I. K. Berestovaya Sov. Phys. Solid State **25** 999 (1983).

(Kos *et al.* 2002) A. B. Kos, T. J. Silva and P. Kabos Rev. Sci. Instr **73** 3563 (2002).

(Kraus *et al.* 1981) Kraus, L., Frait, Z. and Schneider, J., Phys. Stat. Sol. **64**.(1981)

(Krivosik and Patton 2006) P. Krivosik and C. E. Patton J. Appl Phys (to be submitted) (2006).

(Krivosik *et al.* 2004) P. Krivosik, S. S. Kalarickal, N. Mo and C. E. Patton. "*Two-magnon scattering processes in magnetic thin films - a simple and mathematically tractable model.*" The 49th MMM Conference, Nov. 7-11, Book of Abstracts, Jacksonville, Florida (2004).

(Kuanr *et al.* . 2005) B. Kuanr, R. Camley and Z. Celinski Appl. Phys. Lett. **87** 012502 (2005).

(Landau and Lifshitz 1935) L. D. Landau and E. M. Lifshitz Physik. Z. Sowjetunion **8** 153 (1935).

(Lax and Button 1962) Lax and Button *Microwave ferrites and ferrimagnetics.* New York, (McGraw Hill Book Company, 1962)

(LeCraw, *et al.* 1958) R. C. LeCraw, E. G. Spencer and C. S. Porter Phys. Rev. **110** 1131 (1958).

(Liu *et al.* 2003) Liu, X., Rantschler, J., Alexander, C. and Zangari, G., IEEE Trans. Magn. **39**(5), 2362-2364 (2003).

(Mantese *et al.* 1996) J. V. Mantese, A. L. Micheli, D. F. Dungan, R. G. Geyer, J. Baker-Jarvis and J. Grosvenor J. Appl Phys **79** 1655 (1996).

(McMichael and Krivosik 2004) R. McMichael and P. Krivosik IEEE Trans. Magn. **40** 2 (2004).

(McMichael et al.1998) R. McMichael, M. Stiles, P. Chen and W. Egelhoff J. Appl. Phys **83**(11) 7037-7039 (1998).

(McMichael *et al.* 2003) R. McMichael, D. Twisselmann and A. Kunz, Phys Rev Lett. **90**, 2760 (2003).

(Mijiritskii and Boerma, 2001) A. V. Mijiritskii and D. O. Boerma Phys. Rev. B **64** 035410 (2001).

(Mo *et al*, 2005) N. Mo, Y. Y. Song, C. E. Patton, J. Appl. Phys, **97**, 093901 (2005).

(Nazarov *et al.* 2003) A. V. Nazarov, D. Menard, J. J. Green, C. E. Patton, G. M. Argentina and H. J. Van Hook J. Appl. Phys. **94**(11) 7227-7234 (2003).

(Néel, 1947) L. Néel C. R. Acad. Sci. (Paris) **224** 1488 (1947).

(Nibarger *et al.* .2003) J. Nibarger, R. Lopusnik and T. Silva Appl. Phys. Lett. **82**(13) 2112-2114 (2003).

(Patton 1968) C. E. Patton, J. Appl. Phys **39** 3060 (1968).

(Patton 1969) C. E. Patton Phys. Rev. **179** 352 (1969).

(Patton 1970) C. E. Patton J. Appl. Phys **41** 1637 (1970).

(Patton 1975) *Microwave resonance and relaxation.* Magnetic Oxides. D. J. Craik, John Wiley, London 575-645 (1975).

(Patton and Van Hook 1972) C. E. Patton and H. J. Van Hook J. Appl. Phys **43** 2872 (1972).

(Patton *et al.* 1966) Patton, C. E., McGill, T. C. and Wilts, C. H., J. Appl Phys **37**(9), 3594 (1966).

(Patton *et al.* 1975) Patton, C. E., Frait, Z. and Wilts, C. H., J. Appl. Phys **46**(11), 5002-5003 (1975).

(Patton *et al.* 1975) Patton, C. E., Frait, Z. and Wilts, C. H., J. Appl. Phys **46**(11), 5002-5003 (1975).

(Patton, 1973) *Angle and thickness dependence of the FMR linewidth in high quality Ni-Fe films*. AIP conference proceedings,10, 135 Denver (1972) (1973).

(Plummer and Weller, 2001) Plummer, V. E. and Weller, *The Physics of Ultra-High-Density Magnetic Recording*, Springer, Berlin (2001).

(Pozar 1990) D. M. Pozar, *Microwave engineering*, (Addison-Wesley, 1990)

(Qi *et al.* 2004) X. Qi, J. Zhou, Z. Yue, Z. Gui and L. Li J. Mag. Mag. Mater **269** 352 (2004).

(Quach, *et al.* 1976) Quach, H., Friedman, A., Wu, C. and Yelon, A., Phys. Rev. **B** 17, 312 (1976).

(Rantschler and Alexander 2003) J. Rantschler and C. Alexander J. Appl. Phys **93**(10) 6665-6667 (2003).

(Rantschler *et al.* 2003) J . Rantschler, Y. Ding, S. Byeon and C. Alexander J. Appl. Phys **93**(10) 6671-6673 (2003).

(Rantschler, 2003) J. Rantschler, *Ferromagnetic Resonance and Microsrtucture of Soft Magnetic Thin Films* University of Alabama Ph.D. Thesis (2003)

(Riet *et al.* 1997) E. V. d. Riet, W. Klaassens and F. Roozeboom J. Appl. Phys. **81** 806 (1997).

(Roschmann 1975) P. Roschmann IEEE Trans. Magn. **14** 1247 (1975).

(Rossing, 1963) Rossing, T. D., J. Appl Phys **34**, 995 (1963).

(Safonov and Bertram 2003) V. Safonov and H. N. Bertram J. Appl. Phys **94** 529 (2003).

(Schloemann 1958) E. Schloemann J. Phys. Chem. Solids **6** 242 (1958).

(Schlomann 1956) AIEE Special Publication No. T-91 (unpublished) 600 (1956).

(Schneider *et al.* 2005) M. L. Schneider, T. Gerrits, A. B. Kos and T. J. Silva Appl. Phys. Lett. **87** 072509 (2005).

(Seiden and Grunberg 1963) P. E. Seiden and J. G. Grunberg J. Appl. Phys. **34** 1696 (1963).

(Seiden and Sparks 1965) P. E. Seiden and M. Sparks Phys. Rev. **137** A1278 (1965).

(Sengupta and Sengupta 1997) L. C. Sengupta and S. Sengupta IEEE Trans. Ultrasonics, Ferroelectrics and Frequency Control **44**(4) 793 (1997).

(Silva *et al.* 1999) T. J. Silva, C. S. Lee, T. M. Crawford and C. T. Rogers J. Appl Phys **85** 7849 (1999).

(Spano and Bhagat, 1981) Spano, M. L. and Bhagat, S. M., J. Mag. Mag. Mater **24**, 143 (1981).

(Sparks 1964) M. Sparks, *Ferromagnetic Relaxation Theory*, (McGraw-Hill, New York (1964).

(Sparks 1970) M. Sparks Phys. Rev. B **60** 7395 (1970).

(Sparks *et al.* 1961) M. Sparks, R. Loudon and C. Kittel Phys. Rev. **122** 791 (1961).

(Stoner and Wohlfarth, 1948) E. C. Stoner and E. P. Wohlfarth Philos. Trans. R. Soc. London, Ser A **240** 599 (1948).

(Sun *et al.* 2002) N. Sun, S. Wang, T. Silva and A. Kos IEEE Trans. Magn. **38**(1) 146-150 (2002).

(Truedson *et al.* . 1994) J. R. Truedson, P. Kabos, K. D. McKinstry and C. E. Patton J. Appl. Phys. **76**(1) 432 (1994).

(Truedson, *et al.* 1993) Truedson, J. R., McKinstry, K. D., Kabos, P. and Patton, C. E., J. Appl. Phys **74**(4), 2705-2718 (1993).

(Twisselmann and McMichael, 2003) Twisselmann, D. and McMichael, R., J. Appl. Phys **93**(10), 6903-6905 (2003).

(Valenzuela 1994) Valenzuela, *Magnetic Ceramics*, (Cambridge University Press, 1994).

(Van der Pauw 1958) L. Van der Pauw, A method of measuring the resistivity and Hall coefficient on lamellae of arbitrary shape, Philips Technical Review **20**(8), 220 (1958).

(Van Hook and Willingham 1984) H. J. Van Hook and C. B. Willingham Adv. Ceram. **15** 1637 (1984).

(Van Hook *et al.* 1968) H. J. Van Hook, J. J. Green, F. Euler and E. R. Czerlinsky J. Appl Phys **39** 730 (1968).

(Viala *et al.* 1996) B. Viala, M. K. Minor and J. A. Barnard IEEE Trans. Magnetics **32**(5) 3506 (1996).

(Viala *et al.* 1996) Viala, Minor and Barnard J. Appl. Phys **7** 3941 (1996).

(Vonsovskii 1961) Vonsovskii Chap V. *Ferromagnetic resonance.* E. A. Turov. Moscow, GIMFL (1961).

(Wangsness 1955) R. K. Wangsness Phys. Rev. **98** 927 (1955).

(Wolf 1961) P. Wolf J. Appl Phys **32** 95S (1961).

(Yoshizawa, *et al.* 1988) Y. Yoshizawa, S. Oguma and K. Yamaguchi J. Appl Phys **64** 6044 (1988).

(Van Hook *et al.* 1968) H. J. Van Hook, J. J. Green, F. Euler and E. R. Czerlinsky J. Appl Phys **39** 730 (1968).

(Viala *et al.* 1996) B. Viala, M. K. Minor and J. A. Barnard IEEE Trans. Magnetics **32**(5) 3506 (1996).

(Viala *et al.* 1996) Viala, Minor and Barnard J. Appl. Phys **7** 3941 (1996).

(Vonsovskii 1961) Vonsovskii Chap V. *Ferromagnetic resonance.* E. A. Turov. Moscow, GIMFL (1961).

(Wangsness 1955) R. K. Wangsness Phys. Rev. **98** 927 (1955).

(Wolf 1961) P. Wolf J. Appl Phys **32** 95S (1961).

(Yoshizawa, *et al.* 1988) Y. Yoshizawa, S. Oguma and K. Yamaguchi J. Appl Phys **64** 6044 (1988).